博士論文

Photocatalytic and Photoelectrochemical Water Splitting on Particulate $SrTiO_3$

（チタン酸ストロンチウム微粒子上での光触媒的及び光電気化学的水分解反応）

Yeilin HAM (咸　藝麟)

The Department of Chemical System Engineering, School of Engineering,

The University of Tokyo

2015 Doctoral Thesis

Contents

Chapter 1: General Introduction

1.1. Clean and Sustainable Energy for the Next Generation

Demand for alternative energy sources which could replace fossil fuels has grown rapidly since the 1973 oil crisis. Also, environmental problems such as smog and global warming started to draw attention of the people, and led to greater interest in clean and renewable energy sources such as hydro powder, wind, geothermal, and solar. The biggest advantage of solar energy over others is its vast amount along with its sustainability. The solar energy reaching the earth is estimated to be about 120,000 TW [1], which far exceeds the current energy consumption worldwide (~ 20 TW). The total energy consumption has been rapidly grown as in Figure 1-1 [2], and is expected to grow more. Since other renewable energy sources such as hydro power and wind are quite limited in their supply, utilization of solar energy is necessary for complete transformation to the green energy society.

There are several ways to utilize solar energy such as photovoltaics, solar heating, and solar hydrogen

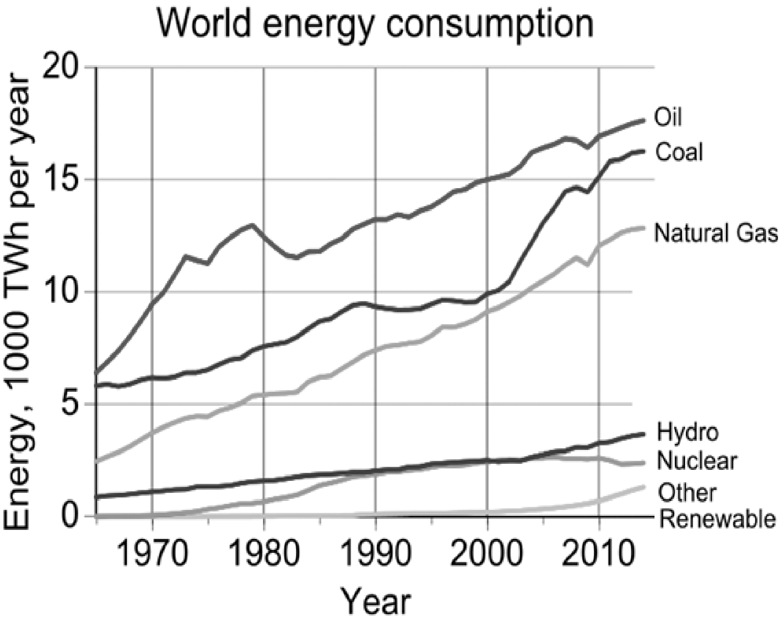

Figure 1-1. World energy consumption from “BP Statistical Review of World Energy June 2015”.

production. Among these methods, the solar hydrogen production through photocatalytic and photoelectrochemical water splitting is considered as a “Holy grail” for clean and sustainable energy production. The concept of utilizing solar energy through water splitting was first presented in the paper by Honda and collaborators published in 1975 [3]. Referring to their words, “the photo-cell produces hydrogen, which can be a source of “clean energy”, through the decomposition of water by means of solar energy.” Hydrogen produced can be stored as a fuel and delivered to the place it is used (Figure 1-2). Therefore, as one of the promising techniques for clean and sustainable energy generation, photocatalytic and photoelectrochemical water splitting have been studied to produce hydrogen with high efficiency and low cost [4,5].

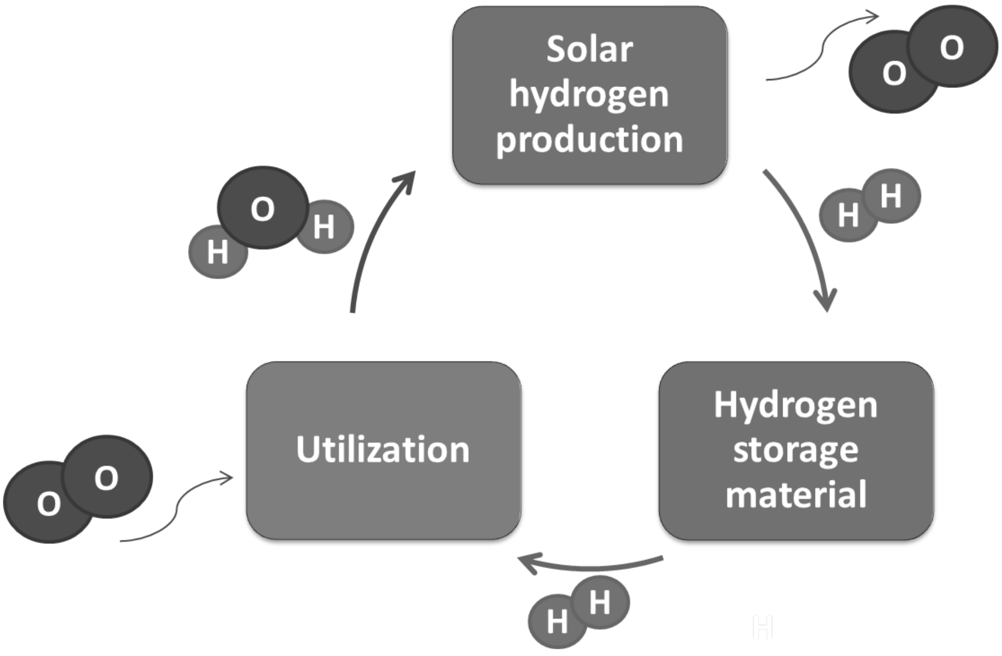

Figure 1-2. Clean and sustainable energy cycle based on the water splitting reaction.

1.2. Required Properties for Photocatalytic Water Splitting

Water splitting into hydrogen and oxygen is an uphill reaction which requires the standard Gibbs free energy change (ΔG°) of 237.141 kJ mol^{-1} or 1.23 eV, as shown in equation 1.1. In photocatalytic water splitting, this energy is provided as photons from sunlight or other light sources. A photon absorbed into a semiconductor can excite an electron in the valence band into the conduction band leaving an excited hole in the valence band. For this excited electron–hole pair to be used for water splitting reaction, the bottom level of the conduction band should be more negative than the reduction potential of H^+/H_2, and the top level of the valence band should be more positive than the oxidation potential of O_2/H_2O as it is illustrated in Figure 1-3. Therefore, photocatalysts must be a semiconductor with band gap energy larger than 1.23 eV, and its conduction band and valence band must sandwich the reduction potential of H^+/H_2 and oxidation potential of O_2/H_2O, to be used for water splitting.

$$H_2O \rightarrow \tfrac{1}{2}O_2 + H_2;\ \Delta G^{\circ} = +237.141\ kJmol^{-1} \quad (1.1)$$

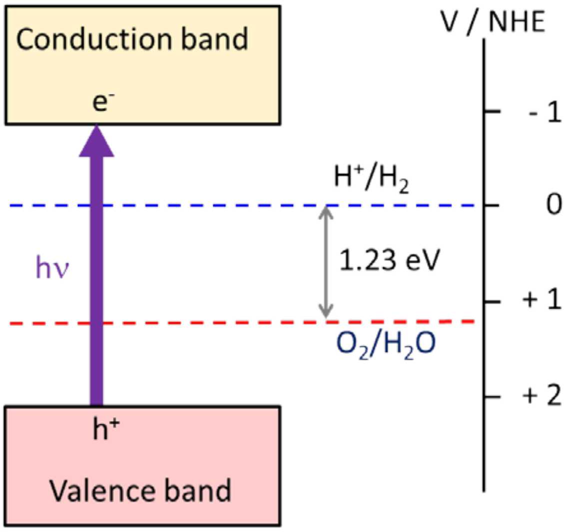

Figure 1-3. Fundamental principle of semiconductor-based photocatalytic water splitting.

The processes in the photocatalytic water splitting include (ⅰ) absorption of photons into photocatalyst, (ⅱ) generation of excited charges (electron and hole pairs), (ⅲ) charge separation, migration, and recombination, (ⅳ) hydrogen evolution and oxygen evolution on the surface of photocatalyst or on the surface of cocatalysts. For the absorption of photons, materials with high absorption coefficient are desirable. The absorption coefficient determines how far a photon with a particular wavelength can penetrate into a material before it is absorbed. A material with a low absorption coefficient will only poorly absorb light, and if the material is too thin, the light will penetrate the material before it is absorbed. Therefore, a photocatalyst should have high absorption coefficient and its particle size must be large enough so that incident light absorbed into the particle before it penetrates it. As it was mentioned, the band gap is important for the generation of excited charges. For the charge separation and migration, the crystal structure, the crystallinity, and the particle size of a photocatalyst are important. It is well known that the defects work as a recombination centers between photo-generated charges. The higher crystallinity means a smaller amount of defects. The generated charges must move to the photocatalyst surface to be used in the hydrogen evolution reaction (HER) or in the oxygen evolution reaction (OER). If a pathway from the point of charge generation to the surface is longer, the possibility of charge recombination increases. Therefore, photocatalysts with high crystallinity and small particle sizes are preferred to decrease recombination. The HER and OER proceed only if the surface of a photocatalyst can work as an active site for each reaction. Since this is not always the case, catalysts for HER and/or OER are deposited on the surface of photocatalysts as active sites, and these are called cocatalysts.

The activity of photocatalytic water splitting can be evaluated by apparent quantum efficiency (AQE). For photocatalyst particles suspended in water, the actual number of absorbed photons cannot be measured because of the scattering of light [6]. Therefore quantum efficiency (QE), defined as equation 1.2 cannot be obtained, and AQE, defined as equation 1.3 is used instead.

$$QE\ (\%) = \frac{Number\ of\ reacted\ electrons}{Number\ of\ absorbed\ photons} \times 100 \quad (1.2)$$

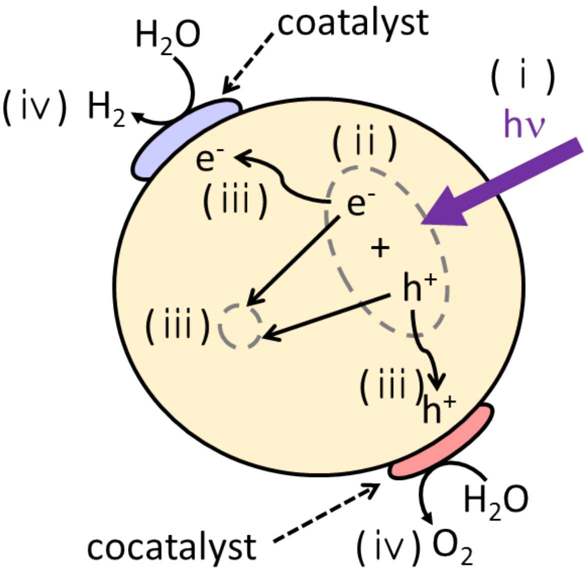

Figure 1-4. Main processes in photocatalytic water splitting.

$$AQE\ (\%) = \frac{Number\ of\ reacted\ electrons}{Number\ of\ incident\ photons} \times 100 = \frac{2\times(Number\ of\ evolved\ H_2)}{(Photon\ flux)\times(area)} \quad (1.3)$$

Some of the highest AQE reported for overall water splitting is summarized in Figure 1-5. The highest AQE reported so far is 71% at 254 nm by utilizing Zn doped Ga_2O_3 [7-11]. The absorption edge of the reported Zn doped Ga_2O_3 was about 274 nm, which corresponds to energy gap of about 4.5 eV [7], while a band bap of pure β-Ga_2O_3 was reported to be 4.9 eV [12,13]. As-purchased Ga_2O_3 worked well as water splitting photocatalyst under UV light [7]. However, its water splitting activity dramatically improved due to (1) addition of divalent cation, especially Zn^{2+}[8], (2) smaller particle size (~ 1 μm) obtained by the ammonia precipitation method compared to as-purchased sample (~ 8 μm) [9], (3) addition of a very small amount of Ca^{2+} (0.89 mol% to Ga), by using dilute $CaCl_2$ solution for the synthesis [11]. La doped $NaTaO_3$ also showed high AQE of 56% at 270 nm [14-17]. $NaTaO_3$ is another well-known water splitting photocatalyst with a band gap of about 4.0 eV [14] and its water splitting activity enhanced due to La doping [15]. Also, a high water splitting activity, which was equivalent to AQE of 50%, was reported on Ba doped $La_2Ti_2O_7$ [18,19], though the specific wavelength of the light used for the measurement was not

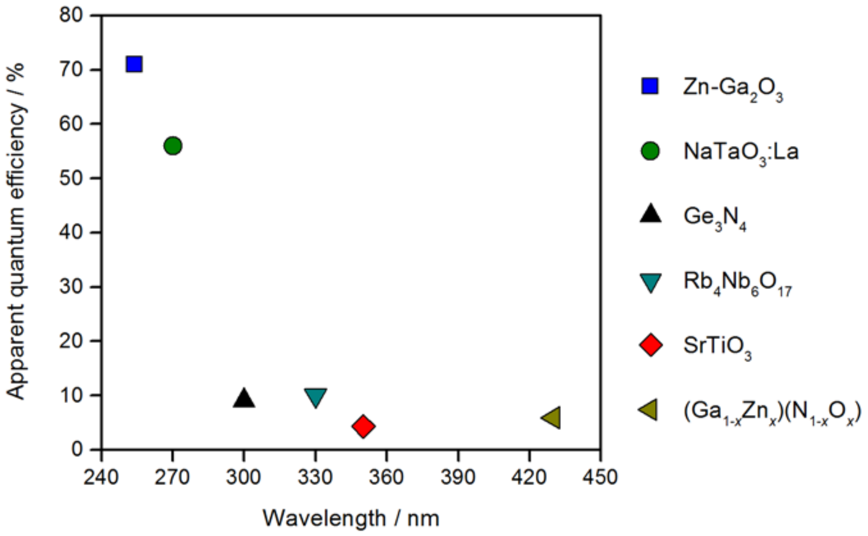

Figure 1-5. Some of the highest apparent quantum efficiency reported for overall water splitting.

reported. Some materials with layered perovskite structure such as $K_4Nb_6O_{17}$ [20-22], and $Rb_4Nb_6O_{17}$ [23], showed relatively high efficiency (5.3% and 10%, respectively) at 330 nm. $SrTiO_3$ is one of the oldest photocatalyst reported to split water into H_2 and O_2 [24-26]. The AQE of 4.3% at 350 nm was reported on KCl-treated $SrTiO_3$ [26], and the enhance activity compared to non-flux-treated $SrTiO_3$ was dedicated to its enhanced physical structure of obtained particles. There are several (oxy)nitrides reported to split water such as Ge_3N_4 [27], $(Ga_{1-x}Zn_x)(N_{1-x}O_x)$ [28-31], $(Zn_{1+x}Ge_x)(N_2O_x)$ [32], TaON [33], $CaTaO_2N$ [34], and $LaMg_xTa_{1-x}O_{1+3x}N_{2-3x}$ [35,36], and much more materials are reported to be active for both HER and OER in the presence of sacrificial agents [37,38]. A β-Ge_3N_4 showed quite high water splitting activity, which was equivalent to AQE of 9%, at around 300 nm [27]. In the visible light region, $(Ga_{1-x}Zn_x)(N_{1-x}O_x)$ shows the highest water splitting activity so far, recording 5.9% at 420−440 nm on $(Ga_{1-x}Zn_x)(N_{1-x}O_x)$ with x =0.18.

1.3. Required Properties for Photoelectrochemical Water Splitting

The photoelectrochemical (PEC) water splitting share some of the principles with the photocatalytic water splitting such as (ⅰ) absorption of photons into a photocatalyst, (ⅱ) generation of excited charges (electron and hole pairs), (ⅲ) charge separation, migration, and recombination, (ⅳ) hydrogen or oxygen evolution on the surface of photoelectrodes or on the surface of cocatalyst. There are two significant points those are different from photocatalytic water splitting. One is that in photoelectrochemical water splitting, HER and OER proceed on two different electrodes which are connected to each other so that current can move from one electrode to another. The n-type semiconductors can be used as photoanodes and the p-type semiconductors can be used as photocathodes. The PEC system can be a photoanode or photocathode connected to a counter electrode (CE) such as Pt or a photoanode series-connected to a photocathode as in Figure 1-6. Since only either of the HER or OER proceeds on one electrode, it is not necessary for the band gap to be larger than 1.23 eV. As long as the valence band maximum (VBM) of a photoanode is more positive than the oxidation potential of O_2/H_2O and the conduction band minimum (CBM) of a photocathode is more negative than the reduction potential of H^+/H_2, excited charges can be used for the water splitting reaction (Figure 1-5). The second point is that in PEC systems charge separation can be engineered by controlling the semiconductor-liquid junction (SCLJ) and (if exists) the metal-semiconductor junction (MSCJ).

There are several ways to evaluate the efficiency of photoelectrochemical water splitting. One definition is the incident photon to current conversion efficiency (IPCE), which is defined as equation 1.4. This value describes how many of the incoming photons at specific wavelength are converted to electrons.

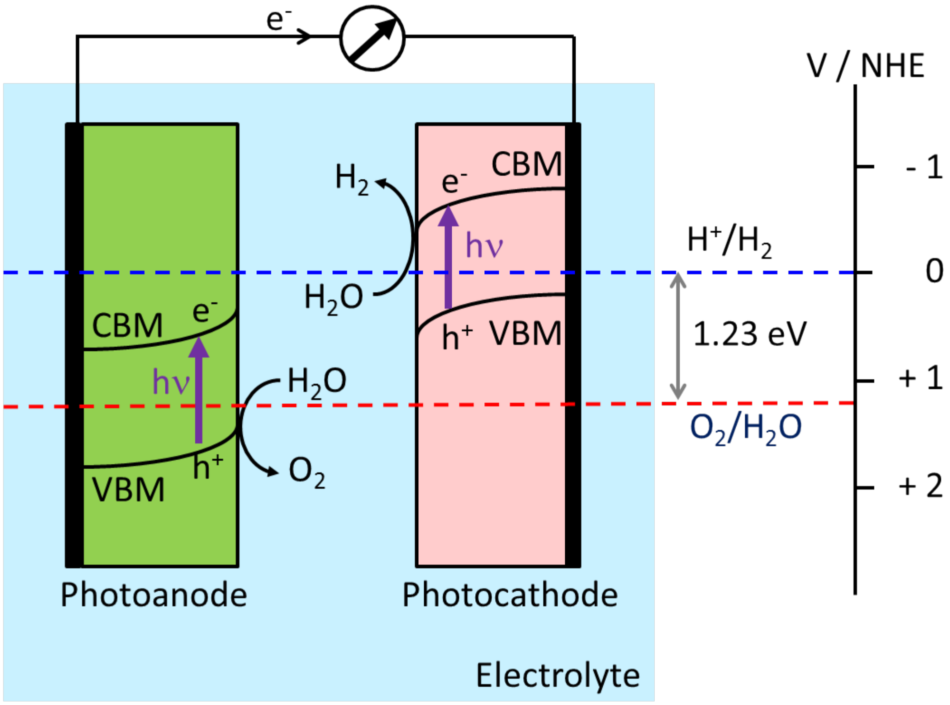

Figure 1-6. Fundamental principles of photoelectrochemical water splitting.

$$IPCE\ (\%) = \frac{Number\ of\ electrons\ out}{Number\ of\ incident\ photons} \times 100 = \frac{J_{SC}}{q\Phi} = \frac{hc}{q} \times \frac{J_{SC}}{\lambda \times P_{in}} \quad (1.4)$$

1.4. Overview of Properties $SrTiO_3$ as a Photocatalyst for Water Splitting

$SrTiO_3$ is one of the oldest photocatalytic materials [24,39,40], accompanied by TiO_2 [41,42]. On the other hand, $SrTiO_3$ also has been widely studied as different functional materials such as ferromagnetic materials, optoelectric materials and others [43]. Therefore, compare to other newly developed photocatalysts, physical, electrical, optical and chemical properties of $SrTiO_3$ are quite well reported.

The most thermodynamically stable for of $SrTiO_3$ has a perovskite structure as in Figure 1-7. It has a cubic Pm3m space group with lattice parameters of a = 3.905 Å.[44,45] $SrTiO_3$ has an indirect band gap of about 3.2 eV.[45-47] The carrier density of $SrTiO_3$ could be modified by controlling oxygen vacancies. It

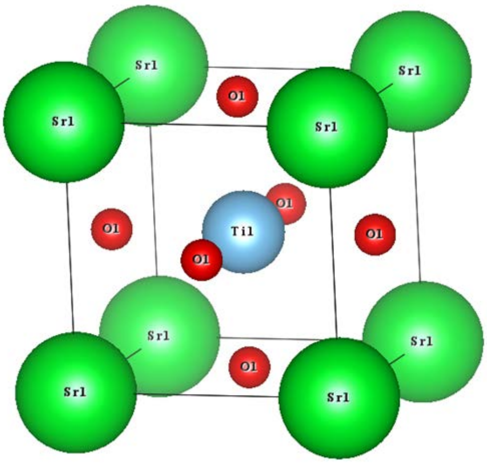

Figure 1-7. Unit cell of $SrTiO_3$, which has a perovskite structure.

has been well examined that $SrTiO_3$ could split water into hydrogen and oxygen with proper surface modifications such as deposition of NiO_x and $Rh_{2-y}Cr_yO_3$ as hydrogen evolution cocatalysts.[24-26] Recently, it was reported that the photocatalytic activity of $SrTiO_3$ to the overall water splitting could be controlled by doping lower valent cations such as Na^+ and Ga^{3+} ions into the Sr^{2+} and Ti^{4+} sites, respectively [48]. The photocatalytic activity improved more than one order of magnitude by doping these ions. The photocatalytic activity of $SrTiO_3$ to the overall water splitting was also reported to improve by flux treatment, which is one of the methods to synthesize powders with high crystallinity owing to dissolution and recrystallization of a material as in Figure 1-8. Kato et al. suggested that the enhancement of the photocatalytic activity was due to the exposure of the effective crystal facets such as {120} and {121} facets for the photocatalytic reaction by the flux treatment.[26] Still the highest reported value of the apparent quantum efficiency for $SrTiO_3$ was 4.3% at 350 nm,[26] which was much lower than the values reported of 71% for Zn-Ga_2O_3[11] and 56% for $NaTaO_3$:La.[16]

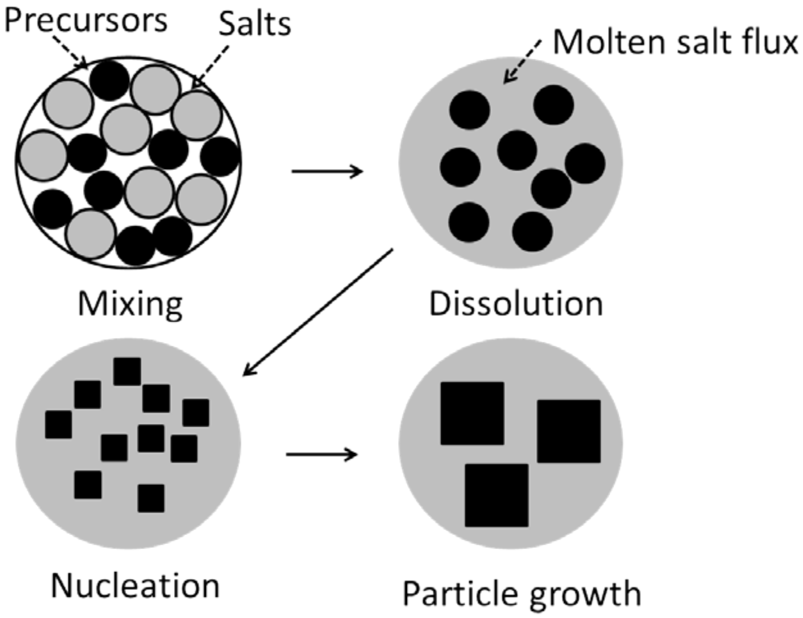

Figure 1-8. Schematic illustration of flux treatment.

1.5. The Objective of This Thesis

For the realistic application of photocatalysts for solar hydrogen production, it is important to develop photocatalysts which can utilize solar energy till the longer wavelength region. Also, it is important to modify the developed photocatalysts to improve their quantum efficiency. For my research, I focused on solving the latter problem, that is, the improvement of the quantum efficiency of a specific material. Some of the highest AQE reported for overall water splitting is summarized in Figure 1-8. In the < 300 nm range, photocatalysts with AQE over 50% have been reported [11,16]. In the ≥ 300 nm range, the highest value of AQE was about 9% for Ge_3N_4 at 300 nm [27]. I targeted to synthesize photocatalysts which shows high apparent quantum efficiencies in the ≥ 300 nm range. Therefore, $SrTiO_3$ was chosen as a material to work with because properties as a water splitting photocatalyst had already been reported. As a method to improve water splitting activity of $SrTiO_3$, metal ion doping and flux treatment were applied in my work.

Using the obtained $SrTiO_3$ photocatalyst particles, electrodes were prepared by the particle transfer method.[49] The properties of the electrodes prepared from $SrTiO_3$ particles with different photocatalytic properties and those made of single crystalline wafers of $SrTiO_3$ were compared, so that the potential of the electrodes prepared from the particles could be evaluated. Also, differences and similarities of the photocatalytic and photoelectrochemical water splitting were discussed.

1.6. General Experimental Procedures

1.6.1. Measurement of Photocatalytic Activity of $SrTiO_3$ Powder

The activities of the photocatalyst samples were tested in a closed gas circulation system with a top-irradiation-type reactor as shown in Figure 1-9. The deionized water (100 mL) was evacuated to remove air completely. The reactor was irradiated using a 300 W xenon lamp (λ >300 nm) through a quartz window or using a 450 W high-pressure mercury lamp through a quartz cooling jacket and, when necessary, a 2-cm diameter slit, a band pass filter (λ = 360 nm, FWHM = 10 nm), and a series of neutral density filters (OD = 0.3, 0.5, 1.0, and 2.0) to irradiate the sample with monochromatic light with controlled intensity. The intensity of the irradiated monochromatic light was measured with a silicon photodiode. The evolved gases were analyzed by a gas chromatograph (Shimadzu, GC-8A) equipped with a thermal conductivity detector, using Ar as a carrier gas.

1.6.2. Photoelectrochemical Measurements

Photoelectrochemical (PEC) properties were measured by a typical 3-electrode setup as shown in Figure 1-10. The prepared electrode, an Ag/AgCl electrode in 3 M NaCl aqueous solution, and a Pt wire were connected to a potentiostat (HSV-100; Hokuto Denko Corp.) as working, reference, and counter electrodes, respectively. A 300 W xenon lamp (λ >300 nm) was used as a light source. When necessary, a monochromator (CT-10) was set in front of the xenon lamp to irradiate monochromatic light. All PEC measurements were performed under an Ar atmosphere.

1.6.3. Sample Characterization

The crystal structures of the products were characterized by X-ray diffractometry (XRD; RINT Ultima III, Rigaku Co.) using Cu K_{α} radiation at 40 kV and 40 mA. XRD peaks due to Cu $K_{\alpha1}$ and $K_{\alpha2}$ radiation were deconvoluted and the full width at half maximum (FWHM) of the (110) peak due to the Cu $K_{\alpha1}$ radiation was estimated. Specific surface areas were measured with a Belsorp-miniII (BEL Japan Inc.). The morphology of the powder was observed by scanning electron microscopy (SEM; S-4700, Hitachi High-Technologies Co.). Ultraviolet-visible diffuse reflectance spectrometry (DRS; V-670, Jasco Co.) was performed using spectralon (Jasco Co.) as a reference material. The surface states of the materials were examined by X-ray photoelectron spectroscopy (XPS; JPS-9000, Jeol Ltd.) using Mg K_{α} radiation. The binding energies were corrected using the binding energy of adventitious carbon (C1s, 284.6 eV). Inductively coupled plasma optical emission spectroscopy (ICP-OES; Shimadzu Co., ICPS-8100) was used for elemental analysis. $SrTiO_3$ powder (0.01 g) was melted with 1.0 g of a 3:1 mixture of Na_2CO_3 and $B(OH)_3$ by heating. An aqueous solution of tartaric acid (5%, 10 mL), HCl (1+1, 4 mL), and H_2O_2 (30 wt%, 1 mL) were added to dissolve the melt, and diluted with distilled water to make the total volume 100 mL. The resulting solution was used to measure Al and Y. The solution was further diluted tenfold to measure Sr and Ti.

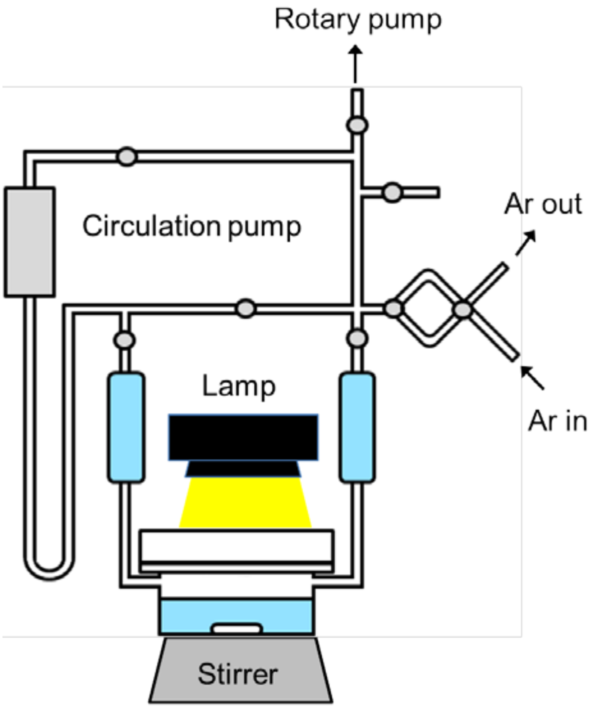

Figure 1-9. Schematic illustration of a closed-circulation system.

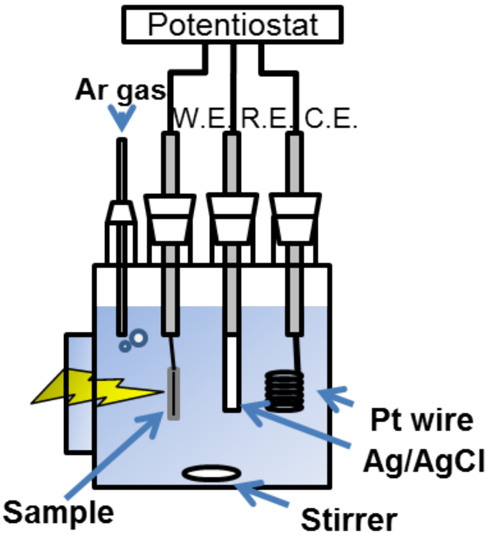

Figure 1-10. Schematic illustration of a PEC measurement cell

References

[1] S. Y. Reece, J. A. Hamel, K. Sung, T. D. Jarvi, A. J. Esswein, J. J. Pijpers, and D. G. Nocera, “Wireless solar water splitting using silicon-based semiconductors and earth-abundant catalysts,” *Science*, vol. 334, no. 6056, pp. 645–648, 2011.

[2] “Statistical Review of World Energy 2015”, (2015, Dec. 25). Retrieved from http://www.bp.com/en/global/corporate/energy-economics/statistical-review-of-world-energy.html.

[3] 3 A. Fujishima, K. Kohayakawa, and K. Honda, “Formation of hydrogen gas with an electrochemical photo-cell,” *Bulletin of the Chemical Society of Japan*, vol. 48, no. 3, pp. 1041–1042, 1975.

[4] J. Nowotny, C. Sorrell, L. Sheppard, and T. Bak, “Solarhydrogen: environmentally safe fuel for the future,” *International Journal of Hydrogen Energy*, vol. 30, no. 5, pp. 521–544, 2005.

[5] B. A. Pinaud, J. D. Benck, L. C. Seitz, A. J. Forman, Z. Chen, T. G. Deutsch, B. D. James, K. N. Baum, G. N. Baum, S. Ardo *et al.*, “Technical and economic feasibility of centralized facilities for solar hydrogen production via photocatalysis and photoelectrochemistry,” *Energy & Environmental Science*, vol. 6, no. 7, pp. 1983–2002, 2013.

[6] A. Salinaro, A. V. Emeline, J. Zhao, H. Hidaka, V. K. Ryabchuk, and N. Serpone, “Terminology, relative photonic efficiencies and quantum yields in heterogeneous photocatalysis. part ii: Experimental determination of quantum yields,” *Pure and Applied Chemistry*, vol. 71, no. 2, pp. 321–335, 1999.

[7] T. Yanagida, Y. Sakata, and H. Imamura, “Photocatalytic decomposition of H_2O into H_2 and O_2 over Ga_2O_3 loaded with nio,” *Chemistry Letters*, vol. 33, no. 6, pp. 726–727, 2004.

[8] Y. Sakata, Y. Matsuda, T. Yanagida, K. Hirata, H. Imamura, and K. Teramura, “Effect of metal ion addition in a Ni supported Ga_2O_3 photocatalyst on the photocatalytic overall splitting of H_2O,” *Catalysis letters*, vol. 125, no. 1-2, pp. 22–26, 2008.

[9] Y. Sakata, Y. Matsuda, T. Nakagawa, R. Yasunaga, H. Imamura, and K. Teramura, “Remarkable improvement of the photocatalytic activity of Ga_2O_3 towards the overall splitting of H_2O,” *ChemSusChem*, vol. 4, no. 2, pp. 181–184, 2011.

[10] Y. Sakata, T. Nakagawa, Y. Nagamatsu, Y. Matsuda, R. Yasunaga, E. Nakao, and H. Imamura, “Photocatalytic properties of gallium oxides prepared by precipitation methods toward the overall splitting of H_2O,” *Journal of Catalysis*, vol. 310, pp. 45–50, 2014.

[11] Y. Sakata, T. Hayashi, R. Yasunaga, N. Yanaga, and H. Imamura, “Remarkably high apparent quantum yield of the overall photocatalytic H_2O splitting achieved by utilizing Zn ion added Ga_2O_3 prepared using dilute $CaCl_2$ solution,” *Chemical Communications*, vol. 51, no. 65, pp. 12 935–12 938, 2015.

[12] M. Orita, H. Ohta, M. Hirano, and H. Hosono, “Deep-ultraviolet transparent conductive β-Ga_2O_3 thin films,” *Applied Physics Letters*, vol. 77, p. 4166, 2000–4168.

[13] M. Mohamed, C. Janowitz, I. Unger, R. Manzke, Z. Galazka, R. Uecker, R. Fornari, J. R.Weber, J. B. Varley, and C. G. Van de Walle, “The electronic structure of β-Ga_2O_3,” *Applied Physics Letters*, vol. 97, no. 21, p. 211903, 2010.

[14] H. Kato and A. Kudo, “Highly efficient decomposition of pure water into H_2 and O_2 over $NaTaO_3$ photocatalysts,” *Catalysis letters*, vol. 58, no. 2-3, pp. 153–155, 1999.

[15] A. Kudo and H. Kato, “Effect of lanthanide-doping into $NaTaO_3$ photocatalysts for efficient water splitting,” *Chemical Physics Letters*, vol. 331, no. 5, pp. 373–377, 2000.

[16] H. Kato, K. Asakura, and A. Kudo, “Highly efficient water splitting into H_2 and O_2 over lanthanum-doped $NaTaO_3$ photocatalysts with high crystallinity and surface nanostructure,” *Journal of the American Chemical Society*, vol. 125, no. 10, pp.3082–3089, 2003.

[17] A. Iwase, H. Kato, H. Okutomi, and A. Kudo, “Formation of surface nano-step structures and improvement of photocatalytic activities of $NaTaO_3$ by doping of alkaline earth metal ions,” *Chemistry Letters*, vol. 33, no. 10, pp. 1260–1261, 2004.

[18] H. Kim, D. Hwang, Y. Kim, J. Lee *et al.*, “Highly donor-doped (110) layered perovskite materials as novel photocatalysts for overall water splitting,” *Chemical Communications*, no. 12, pp. 1077–1078, 1999.

[19] J. Kim, D. W. Hwang, H. G. Kim, S. W. Bae, J. S. Lee, W. Li, and S. H. Oh, “Highly efficient overall water splitting through optimization of preparation and operation conditions of layered perovskite photocatalysts,” *Topics in Catalysis*, vol. 35, no. 3-4, pp. 295–303, 2005.

[20] A. Kudo, A. Tanaka, K. Domen, K. Maruya, K. Aika, and T. Onishi, “Photocatalytic decomposition of water over NiO-$K_4Nb_6O_{17}$ catalyst,” *Journal of catalysis*, vol. 111, no. 1, pp. 67–76, 1988.

[21] A. Kudo, K. Sayama, A. Tanaka, K. Asakura, K. Domen, K. Maruy, and T. Onishi, “Nickel-loaded $K_4Nb_6O_{17}$ photocatalyst in the decomposition of H_2O into H_2 and O_2: Structure and reaction mechanism,” *Journal of catalysis*, vol. 120, no. 2, pp. 337–352, 1989.

[22] K. Sayama, A. Tanaka, K. Domen, K. Maruya, and T. Onishi, “Improvement of nickel-loaded $K_4Nb_6O_{17}$ photocatalyst for the decomposition of H_2O,” *Catalysis letters*, vol. 4, no. 3, pp. 217–222, 1990.

[23] K. Sayama, A. Tanaka, K. Domen, K. Maruya, and T. Onishi, “Photocatalytic decomposition of water over a Ni-loaded $Rb_4Nb_6O_{17}$ atalyst,” *Journal of Catalysis*, vol. 124, no. 2, pp. 541–547, 1990.

[24] K. Domen, S. Naito, M. Soma, T. Onishi, and K. Tamaru, “Photocatalytic decomposition of water vapour on an NiO–$SrTiO_3$ catalyst,” *Journal of the Chemical Society, Chemical Communications*, no. 12, pp. 543–544, 1980.

[25] K. Domen, A. Kudo, T. Onishi, N. Kosugi, and H. Kuroda, “Photocatalytic decomposition of water into hydrogen and oxygen over nickel (ii) oxide-strontium titanate ($SrTiO_3$) powder. 1. structure of the catalysts,” *The Journal of Physical Chemistry*, vol. 90, no. 2, pp. 292–295, 1986.

[26] H. Kato, M. Kobayashi, M. Hara, and M. Kakihana, “Fabrication of $SrTiO_3$ exposing characteristic facets using molten salt flux and improvement of photocatalytic activity for water splitting,” *Catalysis Science & Technology*, vol. 3, no. 7, pp. 1733–1738, 2013.

[27] J. Sato, N. Saito, Y. Yamada, K. Maeda, T. Takata, J. N. Kondo, M. Hara, H. Kobayashi, K. Domen, and Y. Inoue, “RuO_2-loaded β-Ge_3N_4 as a non-oxide photocatalyst for overall water splitting,” *Journal of the American Chemical Society*, vol. 127,no. 12, pp. 4150–4151, 2005.

[28] K. Maeda, T. Takata, M. Hara, N. Saito, Y. Inoue, H. Kobayashi, and K. Domen, “GaN:ZnO solid solution as a photocatalyst for visible-light-driven overall water splitting,” *Journal of the American Chemical Society*, vol. 127, no. 23, pp. 8286–8287, 2005.

[29] K. Maeda, K. Teramura, T. Takata, M. Hara, N. Saito, K. Toda, Y. Inoue, H. Kobayashi, and K. Domen, “Overall water splitting on $(Ga_{1-x}Zn_x)(N_{1-x}O_x)$ solid solution photocatalyst: Relationship between physical properties and photocatalytic activity,” *The Journal of Physical Chemistry B*, vol. 109, no. 43, pp. 20 504–20 510, 2005.

[30] K. Maeda, K. Teramura, D. Lu, T. Takata, N. Saito, Y. Inoue, and K. Domen, “Photocatalyst releasing hydrogen from water,” *Nature*, vol. 440, no. 7082, pp. 295–295, 2006.

[31] K. Maeda, K. Teramura, and K. Domen, “Effect of postcalcination on photocatalytic activity of $(Ga_{1-x}Zn_x)(N_{1-x}O_x)$ solid solution for overall water splitting under visible light,” *Journal of catalysis*, vol. 254, no. 2, pp. 198–204, 2008.

[32] Y. Lee, H. Terashima, Y. Shimodaira, K. Teramura, M. Hara, H. Kobayashi, K. Domen, and M. Yashima, “Zinc germanium oxynitride as a photocatalyst for overall water splitting under visible light,” *The Journal of Physical Chemistry C*, vol. 111, no. 2, pp. 1042–1048, 2007.

[33] K. Maeda, D. Lu, and K. Domen, “Direct water splitting into hydrogen and oxygen under visible light by using modified TaON photocatalysts with d^0 electronic configuration,” *Chemistry-A European Journal*, vol. 19, no. 16, pp. 4986–4991, 2013.

[34] J. Xu, C. Pan, T. Takata, and K. Domen, “Photocatalytic overall water splitting on the perovskite-type transition metal oxyni-tride $CaTaO_2N$ under visible light irradiation,” *Chemical Communications*, vol. 51, no. 33, pp. 7191–7194, 2015.

[35] C. Pan, T. Takata, M. Nakabayashi, T. Matsumoto, N. Shibata, Y. Ikuhara, and K. Domen, “A complex perovskite-type oxynitride: The first photocatalyst for water splitting operable at up to 600 nm,” *Angewandte Chemie International Edition*, vol. 54, no. 10, pp. 2955–2959, 2015.

[36] C. Pan, T. Takata, and K. Domen, “Overall water splitting on the transition-metal oxynitride photocatalyst $LaMg_{1/3}Ta_{2/3}O_2N$ over a large portion of the visible-light spectrum,” *Chemistry–A European Journal*, 2015, doi: http://dx.doi.org/10.1002/chem.201504376.

[37] A. Kudo and Y. Miseki, “Heterogeneous photocatalyst materials for water splitting,” *Chemical Society Reviews*, vol. 38, no. 1, pp. 253–278, 2009.

[38] X. Chen, S. Shen, L. Guo, and S. S. Mao, “Semiconductorbased photocatalytic hydrogen generation,” *Chemical reviews*, vol. 110, no. 11, pp. 6503–6570, 2010.

[39] T. Watanabe, A. Fujishima, and K. Honda, “Photoelectrochemical reactions at $SrTiO_3$ single crystal electrode,” *Bulletin of the Chemical Society of Japan*, vol. 49, no. 2, pp. 355–358, 1976.

[40] A. Fujishima and K. Honda, “Electrochemical evidence for the mechanism of the primary stage of photosynthesis,” *Bulletin of the chemical society of Japan*, vol. 44, no. 4, pp. 1148–1150, 1971.

[41] A. Fujishima and K. Honda, “Electrochemical photolysis of water at a semiconductor electrode,” *Nature*, vol. 238, pp. 37–38, 1972.

[42] R. Waser, R. Dittmann, G. Staikov, and K. Szot, “Redoxbased resistive switching memories–nanoionic mechanisms, prospects, and challenges,” *Advanced Materials*, vol. 21, no. 25-26, pp. 2632–2663, 2009.

[43] H. D. Megaw, “Crystal structure of double oxides of the perovskite type,” *Proceedings of the Physical Society*, vol. 58, no. 2, p. 133, 1946.

[44] R. Cowley, “Lattice dynamics and phase transitions of strontium titanate,” *Physical Review*, vol. 134, no. 4A, p. A981, 1964.44 A. Kahn and A. Leyendecker, “Electronic energy bands in strontium titanate,” *Physical Review*, vol. 135, no. 5A, p.A1321, 1964.

[45] M. Capizzi and A. Frova, “Optical gap of strontium titanate (deviation from urbach tail behavior),” *Physical Review Letters*, vol. 25, no. 18, p. 1298, 1970.

[46] K. Van Benthem, C. Elsässer, and R. French, “Bulk electronic structure of $SrTiO_3$: Experiment and theory,” *Journal of Applied Physics*, vol. 90, no. 12, pp. 6156–6164, 2001.

[47] T. Takata and K. Domen, “Defect engineering of photocatalysts by doping of aliovalent metal cations for efficient water splitting,” *The Journal of Physical Chemistry C*, vol. 113, no. 45, pp. 19 386–19 388, 2009.

[48] T. Minegishi, N. Nishimura, J. Kubota, and K. Domen, “Photoelectrochemical properties of $LaTiO_2N$ electrodes prepared by particle transfer for sunlight-driven water splitting,” *Chemical Science*, vol. 4, no. 3, pp. 1120–1124, 2013.

Chapter 2: Modification of $SrTiO_3$ Particles with Cation Doping and/or Flux Treatment for Efficient Overall Water Splitting

2.1. Introduction

Photocatalytic water splitting is an important and fundamental photocatalytic reaction and has attracted much attention as a means of H_2 production from water under solar irradiation. A lot of studies have been performed to develop effective photocatalysts for overall water splitting. As a result, various types of photocatalysts have been developed. However, in most cases, the photocatalytic activity is too low for further applications. Some wide band gap oxide photocatalysts exhibit high apparent quantum efficiencies in the overall water splitting reaction but only under ultraviolet irradiation. Other visible-light-driven photocatalysts such as (oxy)nitrides[1-5] can split water under visible light but at low quantum efficiencies. Therefore, further investigations are necessary to improve the photocatalytic activity.

Studies reporting high apparent quantum efficiencies in the water splitting reaction are summarized in Figure 1-5. Zn ion added Ga_2O_3 combined with the $Rh_{0.5}Cr_{1.5}O_3$ cocatalyst was reported to show the remarkably high photocatalytic activity to the overall water splitting under UV light.[6-8] Particularly, when Ga_2O_3 was prepared in dilute $CaCl_2$ solution, the photocatalytic activity was further improved. The apparent quantum yield was reported to be 71% at 254 nm.[8] In the case of a $NaTaO_3$ photocatalyst, the photocatalytic activity was remarkably improved by doping La ions.[9,10] Here, the apparent quantum yield of the photocatalytic overall water splitting was reported to be 56% under the irradiation at 270 nm.[10] In both cases, added metal ions played significant roles for improving the photocatalytic activity. Therefore, the addition of metal ions to the photocatalytic materials is one of the effective ways for improving the photocatalytic activity of overall water splitting.

Highly crystalline particles can be obtained by using a flux as a growth medium. The flux method, which allows the growth of crystalline particles via dissolution and recrystallization of solutes driven by supersaturation, has been applied to the synthesis of metal oxides, including semiconducting oxides, such as $K_4Nb_6O_{17}$,[11] KNb_3O_8,[12] $Na_2Ti_6O_{13}$,[13] $K_2Ti_6O_{13}$,[14] and $SnNb_2O_6$.[15] Some of these oxides showed improved photocatalytic activity compared to those prepared by other synthesis methods. Some semiconducting (oxy)nitride photocatalysts such as $LaTiO_2N$,[16] C_3N_4,[17] and Ta_3N_5[18] have also been prepared with the aid of a flux. However, the downside of this method is the incorporation of impurities into the target material, a commonly observed phenomenon during flux treatment.[19,20] On the other hand, doping can often change the particle morphology dramatically and create mid-gap states essential for visible light activity of some wide-bandgap oxides. In fact, the high activity of $NaTaO_3$ and the visible light activity of $SrTiO_3$ photocatalysts rely on such doping effects. Recently, much effort has been made to understand the effect of doping in terms of carrier dynamics. From the material synthesis standpoint, the challenges in the activation of photocatalysts lie in how to lower defect densities, reduce particle sizes, and incorporate dopants effectively. The flux treatment of photocatalytic materials may offer a solution to such challenges.

$SrTiO_3$ is a classic photocatalyst that has been reported to be active in overall water splitting under UV light since 1980[21] and is still widely investigated in fundamental studies on the effects of doping,[22-25] particle morphology,[26] and cocatalysts.[27] In a recent study, Takata *et al.* found that doping of lower-valence cations in $SrTiO_3$, such as Na^+ into Sr^{2+} and Ga^{3+} into Ti^{4+}, dramatically enhanced the photocatalytic activity during the overall water splitting reaction.[24] This positive effect of doping could be attributed to the lower density of trivalent Ti states. Thus, the effects of the incorporation of even a small amount of impurity into $SrTiO_3$ during the flux treatment should be carefully investigated.

In this chapter, the effects of $SrCl_2$ flux treatment and cation doping on the physical properties and photocatalytic activity of $SrTiO_3$ were investigated.

2.2. Experimental Section

2.2.1. As-purchased $SrTiO_3$

$SrTiO_3$ (Wako Pure Chemicals Industries, Ltd., 99.9%) was employed as a raw material without any post-treatment (hereafter STO(wako)).

2.2.2. Flux Treatment on $SrTiO_3$

NaCl(Wako Pure Chemicals Industries, Ltd., 99.9%), KCl(Wako Pure Chemicals Industries, Ltd., 99.9%), and $SrCl_2$ (Kanto Chemicals Co., Inc., 98.0%, anhydrous) were used as flux. As it is represented in Figure 2-1, STO(wako) and each of flux materials were thoroughly mixed in an agate mortar with molar ratio of flux/$SrTiO_3$ = 10. The mixture was heated in an alumina crucible at 1100 °C for 10 h. After the mixture was cooled to room temperature, $SrTiO_3$ was separated from the solidified mass by repeated washing with deionized water until no white AgCl precipitate formed in rinse solutions upon adding $AgNO_3$. The final product of flux-treated $SrTiO_3$ will hereafter referred to as STO(flux) where flux represents type of flux material used.

2.2.3. $SrCl_2$ Treatment on $SrTiO_3$

For STO($SrCl_2$), treatment conditions were examined in detail. First, the molar ratio of $SrCl_2$/STO was varied from 0.01 to 20. Second, the treatment temperature was varied from 900 to 1100 °C. Third, the soaking time was varied from 1 to 20 hours. At last, the cooling rate to 500 °C was varied from 6 K min^{-1} to natural cooling. The same procedures explained in section 2.2.2 were applied except for the steps mentioned above.

2.2.4. $SrCl_2$ Treatment on $SrTiO_3$ in Yttria Crucibles

Al_2O_3 (Sigma-Aldrich Co, LLC., nanopowder), and $SrCl_2$ (Kanto Chemicals Co., Inc., 98.0%, anhydrous) were used as raw materials. STO(wako), Al_2O_3 (when used), and $SrCl_2$ were thoroughly mixed in an agate mortar. The mixture was heated either in an yttria crucible at 1100 °C for 10 h. The $SrTiO_3$ samples treated in yttria crucibles will hereafter be referred to as STO($SrCl_2$-Y), where -Y was used to highlight the use of yttria crucibles. The STO($SrCl_2$-Y) samples with Al_2O_3 addition will hereafter be referred to as *x*%Al-STO($SrCl_2$-Y), where *x*% represents the Al/Ti molar ratio in the starting mixture.

2.2.5. Al-doping on $SrTiO_3$

Al_2O_3 (Sigma-Aldrich Co, LLC., nanopowder) and $SrCl_2$ (Kanto Chemicals Co., Inc., 98.0%, anhydrous) were used as raw materials. STO(wako) and Al_2O_3 were thoroughly mixed in an agate mortar. The mixture was heated in an yttria crucible at 1100 °C for 10 h. These samples will hereafter be referred to as *x*%Al-STO, where *x*% represents the Al/Ti molar ratio in the starting mixture.

2.2.6. Polymerizable Complex Method

In a polymerizable complex method, $SrCO_3$, titanium isopropoxide, citric acid and ethylene glycol (Wako Pure Chemicals Industries, Ltd.,) were used as starting materials. Equimolar amounts of $SrCO_3$ and titanium isopropoxide were dissolved in methanol containing citric acid and ethylene glycol. The molar ratio of $SrCO_3$: titanium tetoraisopropoxide : citric acid : ethylene glycol was 1 : 1 : 4 : 10 The polymerization of citrates with ethylene glycol was performed under reflux at 458 K for 2 h. The pyrolysis of the polymerized metal complexes was carried out at 623 K for 12 h in air to obtain a carbonized powder. The carbonized sample was finally calcined at 1273 K for 10 h to prepare STO(PC).

2.2.7. Metal Ion Addition

The addition of metal ion was carried out by an impregnation method using suspension of the $SrTiO_3$ powder in an aqueous solution of desired metal salts. The obtained composite of metal salts and $SrTiO_3$ was calcined at 1273 K in air to prepare metal ion added $SrTiO_3$. Here, Li_2CO_3, Na_2CO_3, K_2CO_3, Rb_2CO_3,

Cs_2CO_3, $Mg(NO_3)_2$, $Zn(NO_3)_2$, $Ca(NO_3)_2$, $Ba(NO_3)_2$, $Al(NO_3)_3$, $Ga(NO_3)_3$, $In(NO_3)_3$, $Y(NO_3)_3$ and $La(NO_3)_3$ (Wako pure chemical) were used as the source of the added metal ions.

2.2.8. Loading of Cocatalyst

As a cocatalyst, mixed oxide of rhodium and chromium, $Rh_{2-y}Cr_yO_3$, was loaded by an impregnation method.[28] The $SrTiO_3$ samples were loaded with $Na_3RhCl_6 \cdot nH_2O$ (Rh 17.8 wt%) and $Cr(NO_3)_3 \cdot 9H_2O$ (98.0~103.0%) as Rh and Cr sources, respectively, and calcined in air at 350 °C for 1 h.

2.2.9. Sample Characterization

Photocatalytic water splitting activity and physical properties of the samples were evaluated according to the procedures described in Section 1.6.1 and 1.6.3, respectively.

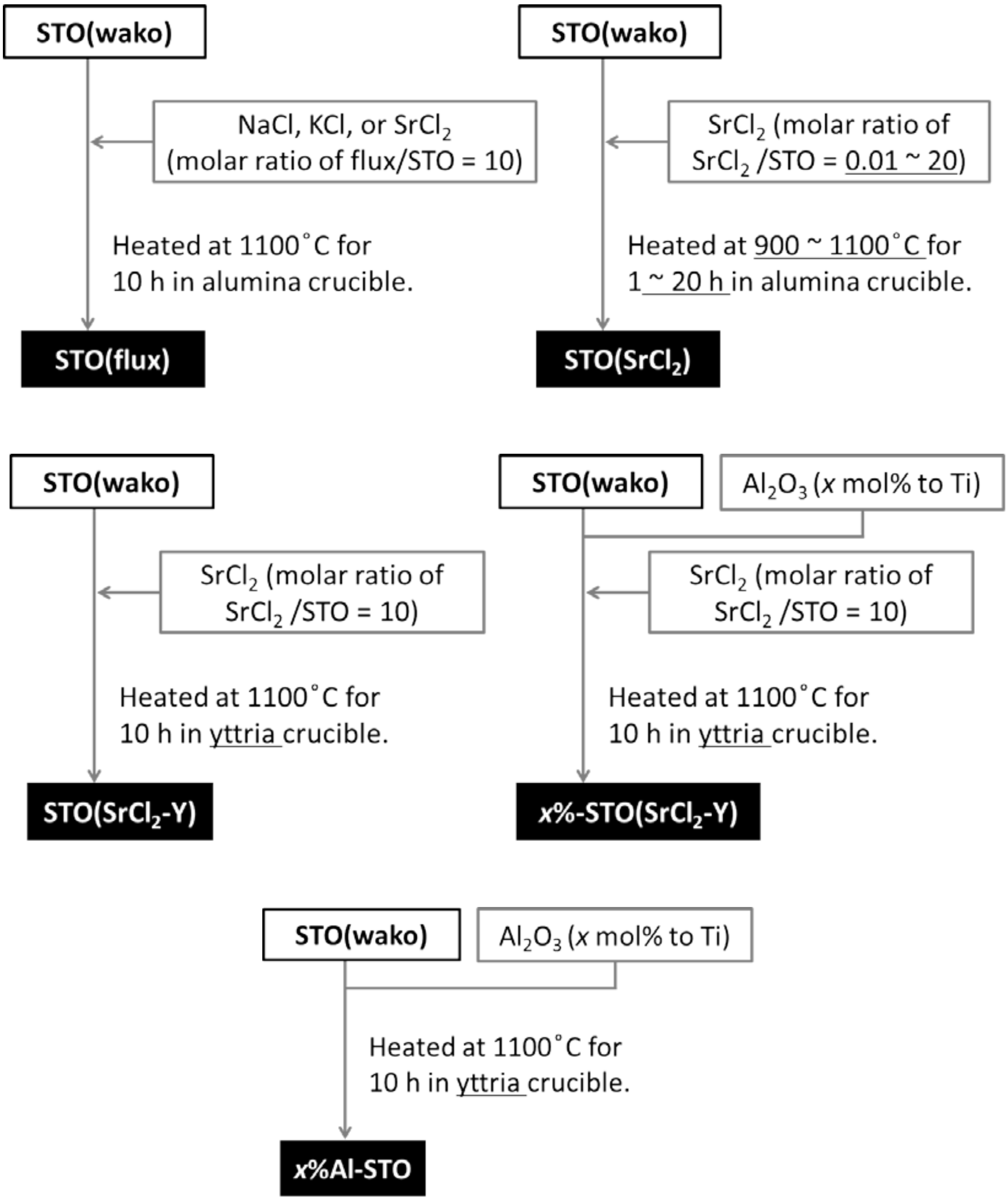

Figure 2-1. Preparation schemes of $SrTiO_3$ samples

2.3. Results and Discussion

2.3.1. Characterization of Flux-Treated $SrTiO_3$ Particles

On the basis of the preceding study by Kato *et al.* reporting that flux-treated $SrTiO_3$ shows improvement in their water splitting activity, as-purchased $SrTiO_3$, STO(wako), was treated with NaCl, KCl, and $SrCl_2$, following the procedures presented in Figure 2-1. XRD patterns of the obtained powders showed peaks assignable to the $SrTiO_3$ phase only (Figure 2-2). The peak intensity of STO(flux) was much higher compared to STO(wako), regardless of the type of flux used. The stronger peak intensity indicates improvement in the crystallinity of particles, which was the targeted effect of the flux treatment. SEM images of the obtained particles presented in Figure 2-3 show clear morphological changes after the flux treatment. STO(wako) consisted of particles with irregular shapes and sizes of about few hundred nanometers. Both STO(NaCl) and STO(KCl) consisted of particles with irregular shapes but sizes of about a few micrometers, larger than STO(wako). STO($SrCl_2$) showed the clearest morphology change among the samples prepared. STO($SrCl_2$) particles were cubic and had a large size distribution ranging over 0.2–3 μm. The equilibrium crystal shape of $SrTiO_3$ was reported to be truncated cubic.[29] Therefore, STO($SrCl_2$) is expected to be crystals closer to the equilibrium crystal than other $SrTiO_3$ powders. These morphology changes after the flux treatments reflect that the crystal growth of $SrTiO_3$ proceeded during the flux treatment and well agree with the result of XRD. However, the reason for the different morphology upon the type of flux used is not clear yet.

The diffuse reflectance spectrum (DRS) of STO(wako) and STO($SrCl_2$) are presented in Figure 2-4. The absorption edge was about 390 nm for both STO(wako) and STO($SrCl_2$), which well agreed with the reported values.[30] The Tauc plot for the indirect allowed transition was plotted for both STO(wako) and STO($SrCl_2$) as in Figure 2-5. The band gap energies acquired from this Tauc plot were approximately 3.18 eV for STO(wako) and 3.16 eV for STO($SrCl_2$). The reported band gap of undoped $SrTiO_3$ is about 3.2 eV.[31-33] Reasons for the slightly narrow band gap of STO($SrCl_2$) is discussed in section 2.3.3.

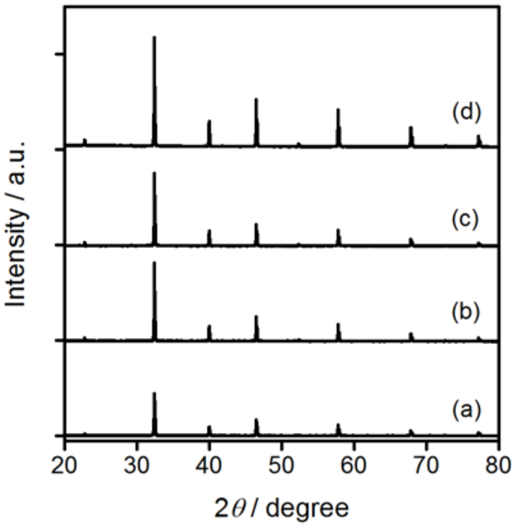

Figure 2-2. XRD patterns of (a) STO(wako), (b) STO(NaCl), (c) STO(KCl) and (d) STO($SrCl_2$).

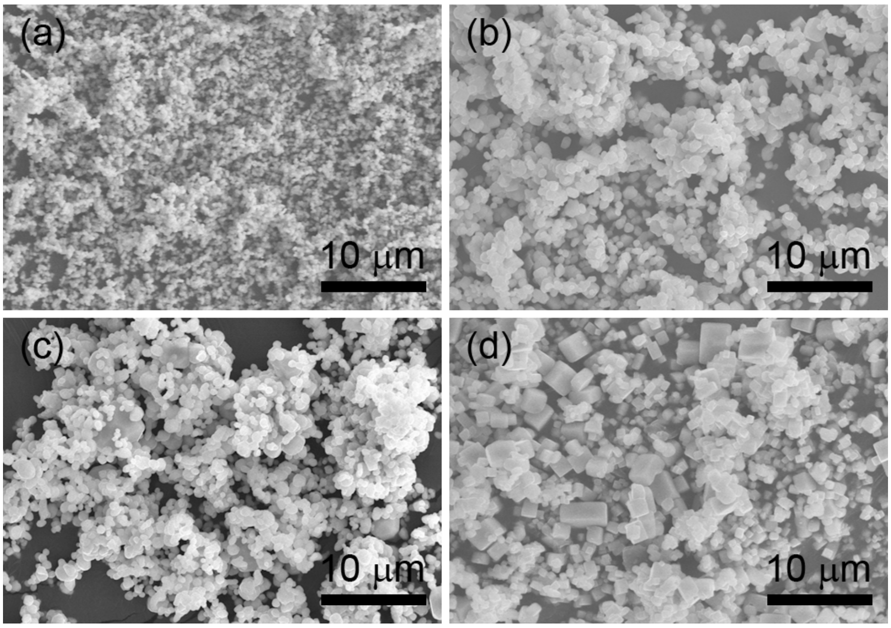

Figure 2-.3. SEM images of (a) STO(wako), (b) STO(NaCl), (c) STO(KCl) and (d) STO($SrCl_2$).

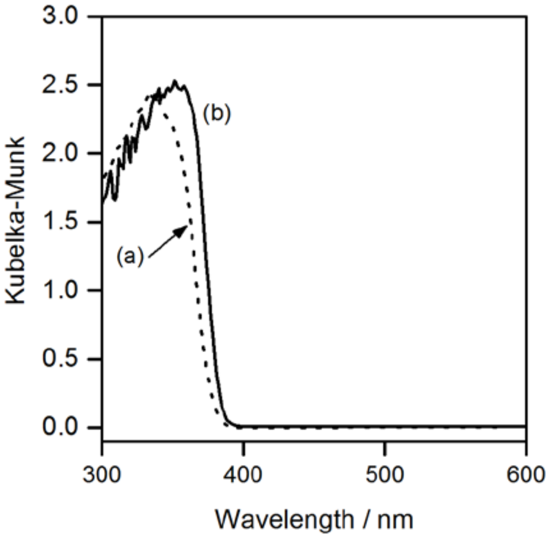

Figure 2-4. Diffuse reflectance spectra of (a) STO(wako) and (b) STO(SrCl$_2$).

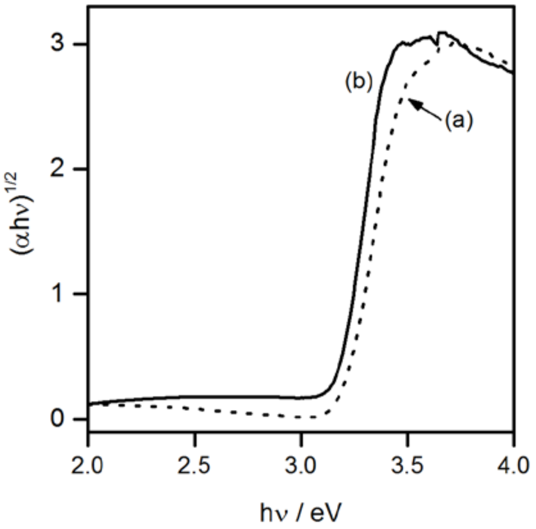

Figure 2-5. Tauc plots of (a) STO(wako) and (b) STO(SrCl$_2$).

Since only STO($SrCl_2$) resulted in particles with the clear cubic morphology, treatment conditions of STO($SrCl_2$) were further investigated. As treatment conditions, (i) treatment temperatures, (ii) soak times, (iii) cooling rates, and (iv) molar ratios of $SrTiO_3$ powder to $SrCl_2$ flux were varied (Figure 2-6). From the classical point of view, as long as the treatment temperature is over the liquidus line, the resulting crystals should independent of the treatment temperature, since there is no phase change in temperature above liquidus line. Also, the quality of crystal should depend on cooling temperature since usually, the driving force of nucleation is the supersaturation driven by cooling. The ratio of flux to precursor is also an important factor since it also affects the supersaturation.

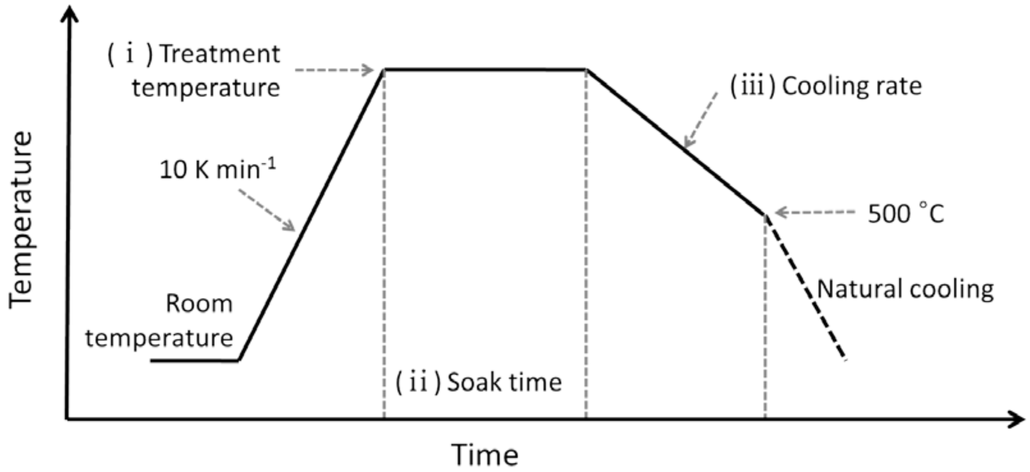

Figure 2-6. Factors involved in the $SrCl_2$ flux treatment of $SrTiO_3$. (i) treatment temperatures, (ii) soak times, (iii) cooling rates, and (iv) molar ratios of $SrTiO_3$ powder to $SrCl_2$ flux.

Treatment temperatures of 900, 1000, 1100 °C, above the melting point of $SrCl_2$ (874 °C) were examined while the ramping rate, soak time, cooling rate, and the ratio of flux to $SrTiO_3$ were fixed to 10 K min^{-1}, 10 hours, natural cooling, and $SrCl_2/SrTiO_3 = 10$, respectively. XRD patterns of the obtained samples showed only the peaks attributable to the $SrTiO_3$ phase only as in Figure 2-7. The FWHM of the (110) peak decreased with increasing the treatment temperatures (Table2-1). Under the same measurement conditions, a difference in the FWHM of XRD peaks reflects the difference in sizes and strains of crystallites. The reduction of the FWHM after the flux treatment should reflect the growth of crystallites with weaker strain, which is indicative of higher crystallinity. Therefore, higher treatment temperatures improved the crystallinity of the powder. The shape of the particles was observed with SEM as shown in Figure 2-8. The crystal shapes were all cubic regardless of the treatment temperature, although the crystal size became larger and its size distribution became broader with increasing treatment temperature. The difference in the crystal sizes observed by SEM well agreed with the BET surface areas of the samples, which decreased with increasing the treatment temperature (Table 2-1). On the basis of the morphology changes, one might consider that dissolution and recrystallization of $SrTiO_3$ particles occurred during the $SrCl_2$ treatment regardless of the treatment temperatures. This means that the binary phase of $SrTiO_3$ and $SrCl_2$ might have become liquid phase under all the treatment temperatures examined. However, in this scheme, the morphology difference upon the different treatment temperatures is unexplainable, because the binary phase which underwent a phase transition into a liquid phase should take the same phase change path upon cooling as long as the ratio of the two different phase are the same. This morphology change upon the treatment temperature could be better explained with Wanklyn's hypothesis based on their experimental results.[34] Wanklyn *et al.* suggests that during the flux treatment of $Pb_2V_2O_7$, nucleation mainly occurs at nucleation sites on the surface of crucibles. Such nucleation sites could dissolve into flux at a higher temperature when the treatment duration is long enough. Therefore, a sample treated at lower temperatures has more nucleation sites and forms many crystals with smaller sizes, while a sample treated at higher temperatures has less nucleation sites and result in fewer crystals with larger sizes as it is illustrated is in Figure 2-9.

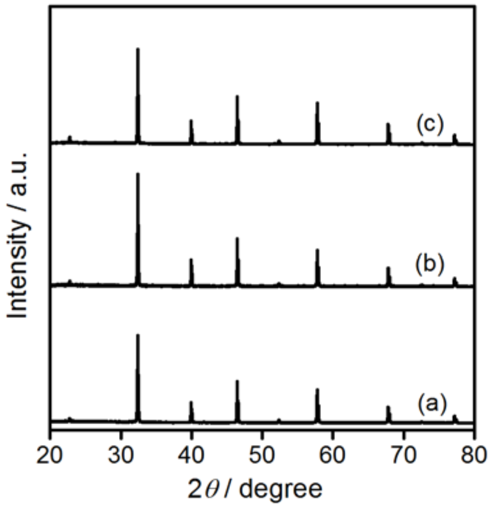

Figure 2-7. XRD patterns of STO($SrCl_2$) treated at (a) 900, (b) 1000, and (c)1100 °C.

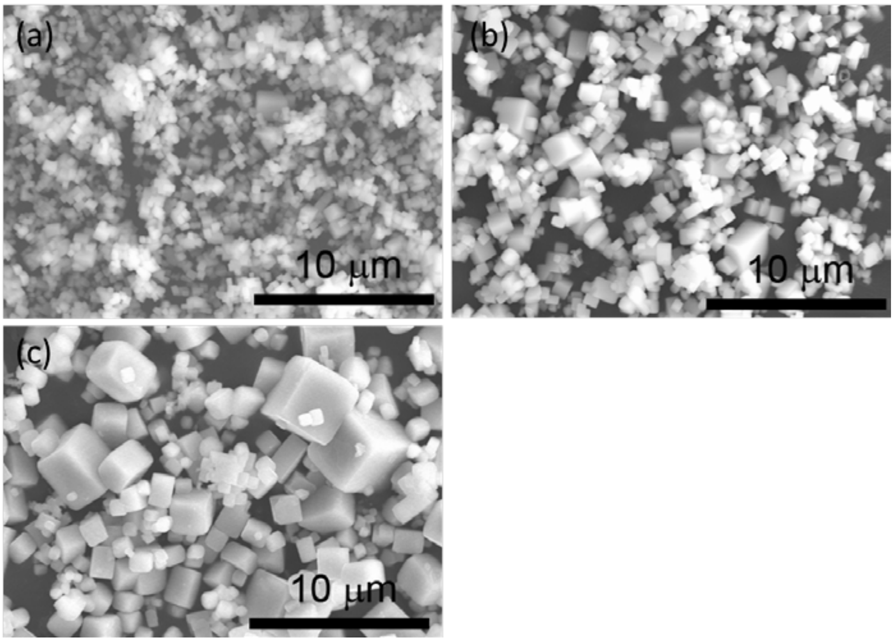

Figure 2-8. SEM images of STO($SrCl_2$) treated at (a) 900, (b) 1000, and (c)1100 °C.

Table 2-1. FWHM of (110) peak in XRD pattern, BET surface area, and molar ratio analyzed by ICP-OES of STO($SrCl_2$) treated with different treatment temperature.

Treatment temperature / °C.	FWHM of (110) peak in XRD pattern* / °	BET surface are / m^2 g^{-1}	Molar ratio 2[Al]/([Sr]+[Ti])
STO(wako)	0.103	3.6	0.04%
900	0.084	1.9	0.12%
1000	0.074	1.3	0.11%
1100	0.066	0.9	0.31%

*(110) peaks due to Cu $K_{\alpha1}$ and $K_{\alpha2}$ was deconvoluted to evaluate the FWHM originating from Cu $K_{\alpha1}$ radaition.

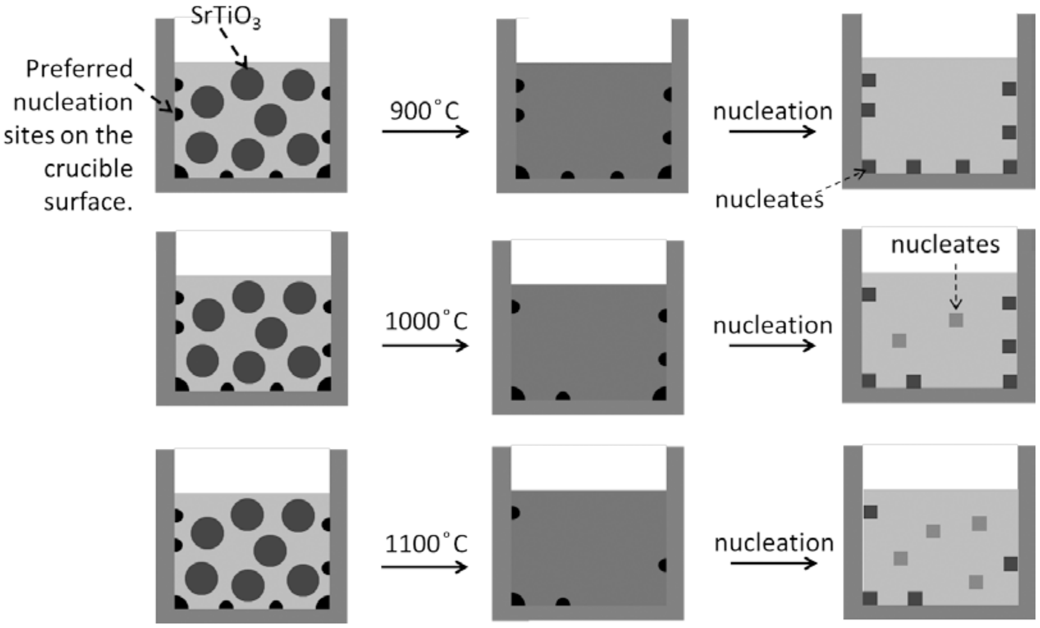

Figure 2-9. Schematic illustration of crystallization upon different treatment temperature during flux treatment.

Next, the soak times of 1, 10, and 20 h were examine. The ramping rate, treatment temperature, cooling rate, and the ratio of flux to $SrTiO_3$ were fixed to 10 K min^{-1}, 1100 °C, natural cooling, and $SrCl_2/SrTiO_3 = 10$, respectively. XRD patterns of the obtained samples showed $SrTiO_3$ phase only as it is shown in Figure 2-10. The morphology of these particles was observed with SEM. No conspicuous difference in morphology was observed among these samples (Figure 2-11). This result seems to be contradictory to the Wanklyn's premise. Wanklyn *et al.* argue that with a longer soak time, nucleation sites on the crucible surface dissolve into the flux and thereby fewer crystals with larger sizes should be obtained. However, the soak time they suggest to get rid of the nucleation sites on the crucible surface was over 100 h which is much longer than the soak time I examined.[34] I believe the soak times examined in my study was not long enough to get rid of crucible nucleation sites and resulted in particles with similar morphologies. Therefore, it could be concluded that at time range of up to 20 h, the soak time of $SrCl_2$ flux treatment has no significant influence on the morphology of STO($SrCl_2$).

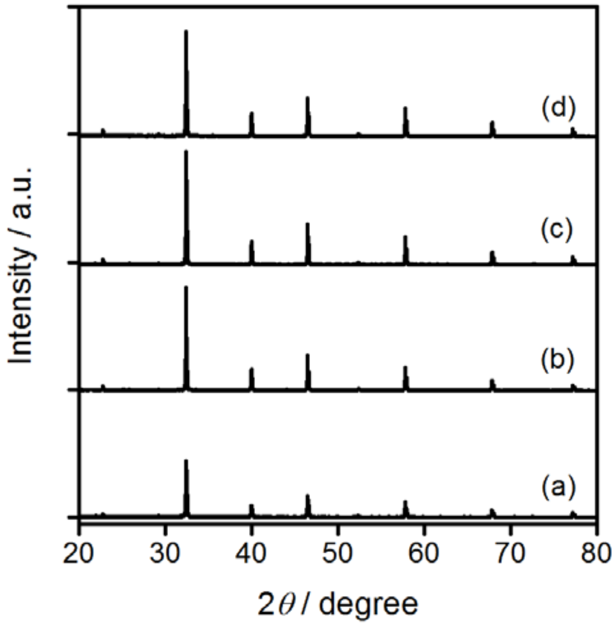

Figure 2-10. XRD patterns of (a) STO(wako) and STO($SrCl_2$) treated for (b) 1, (c) 10, and (d) 20 h .

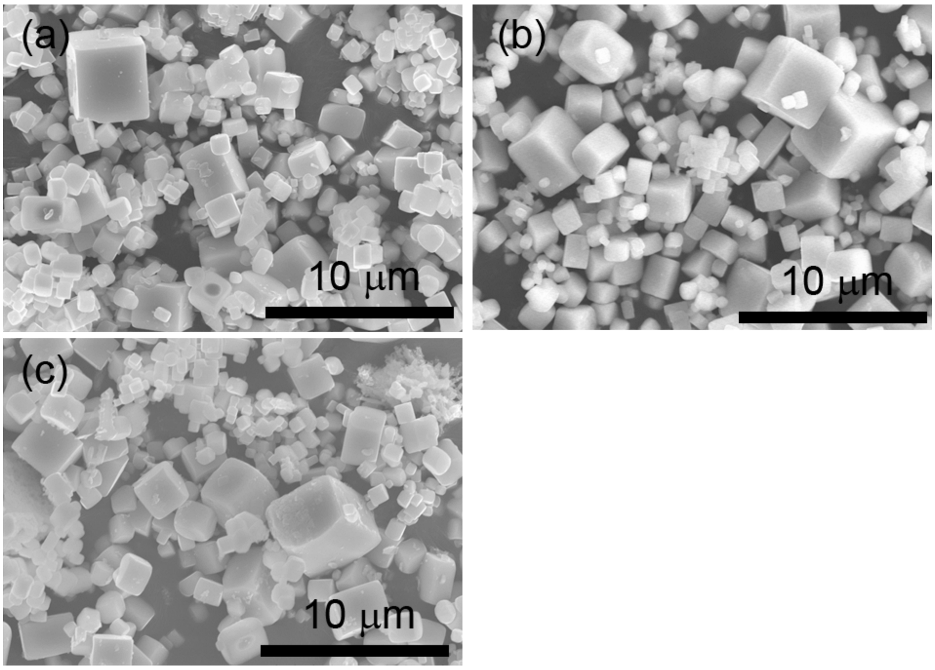

Figure 2-11. SEM images of STO($SrCl_2$) treated for (a) 1, (b) 10, and (c) 20 h .

The cooling rates to 500 °C were examined in the range of 6, 30 K h^{-1}, and natural cooling. The ramping rate, treatment temperature, soak time, and the ratio of flux to $SrTiO_3$ were fixed to 10 K min^{-1}, 1100 °C, 10 h, and $SrCl_2/SrTiO_3$ = 10, respectively. XRD patterns of the obtained samples showed the peaks of the $SrTiO_3$ phase only as shown in Figure 2-12. The morphology of these particles was observed with SEM (Figure 2-13). The particles obtained from the slower cooling rates were slightly larger. However, the difference in the particle sizes was not as prominent as the difference observed for the series of STO($SrCl_2$) samples treated with the different treatment temperatures. If the nucleation process of the crystallization is governed by the supersaturation driven by cooling, the size of crystal should be strongly dependent on the cooling rate. The fact that morphology of STO($SrCl_2$) samples treated with the different cooling rate showed little difference in their crystal sizes supports that the nucleation for this flux treatment is mainly governed by preferential nucleation on the crucible surface rather than the nucleation driven by cooling. Another possibility for the little difference in the particle size could be the fact that the temperature I controlled in my study was only the temperature of the muffle furnace, not the temperature of the sample itself. When a flux material reaches its melting point upon cooling, it starts to crystallize and evolve latent heat and can maintain a constant temperature. Once solidification is complete, steady cooling resumes. Therefore, even though the controlling the temperature of the muffle furnace was controlled, there is a possibility that the temperature of the material was kept constant around the melting point regardless of the difference cooling rate.

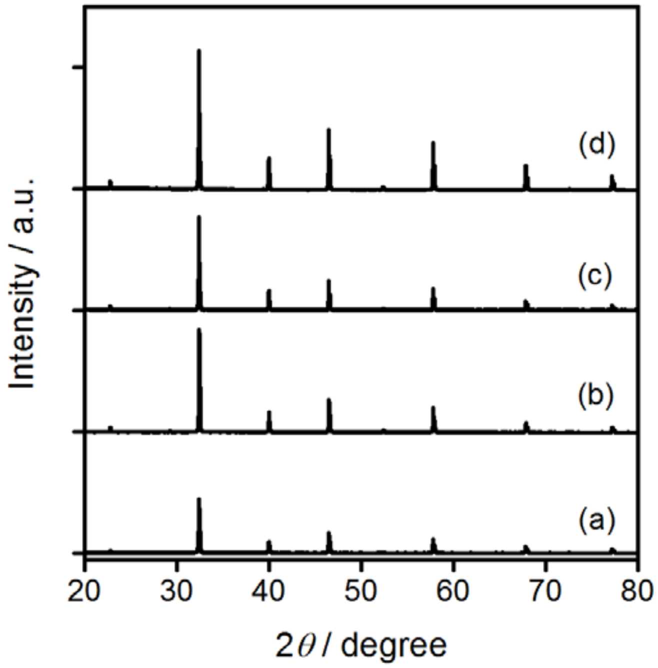

Figure 2-12. XRD patterns of STO($SrCl_2$) treated with different cooling rate of (a) 6 K h^{-1}, (b) 30 K h^{-1}, and (c) natural cooling.

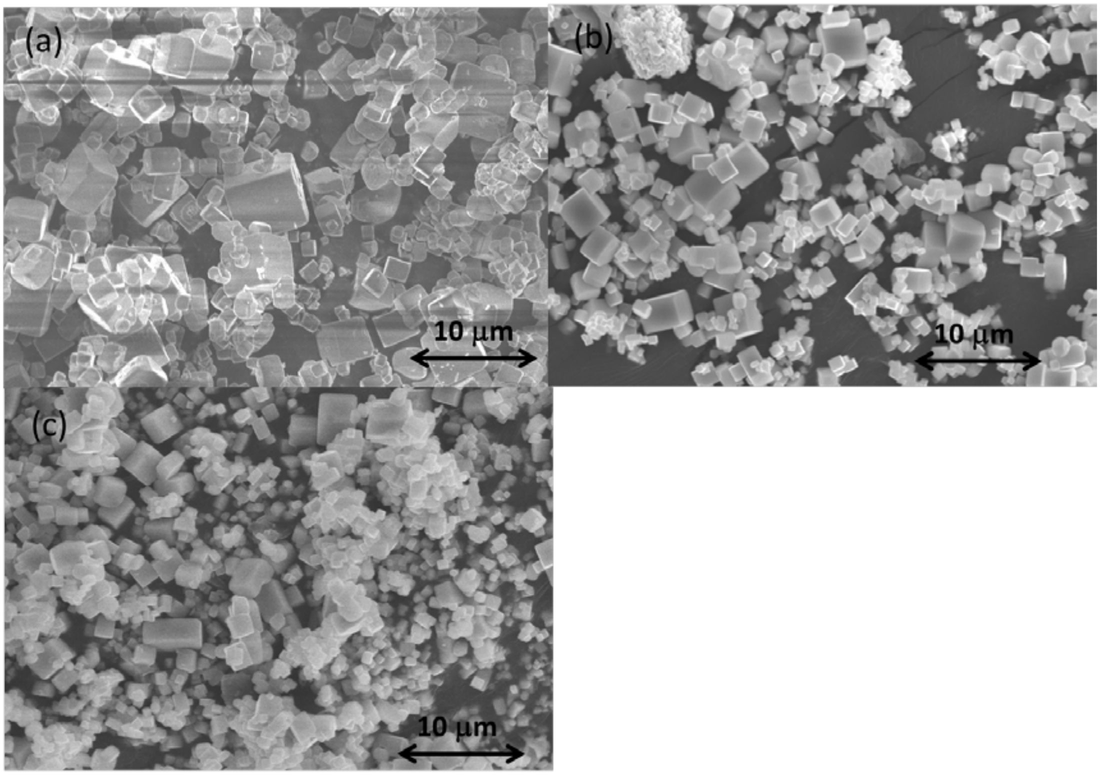

Figure 2-13. SEM images of STO($SrCl_2$) treated with different cooling rate of (a) 6 K h^{-1}, (b) 30 K h^{-1}, and (c) natural cooling.

Next the amount of flux was examined from $SrCl_2/SrTiO_3$ = 0.01 to 20 in the molar ratio. The ramping rate, treatment temperature, soak time, and the cooling rate were fixed to fixed to 10 K min^{-1}, 1100 °C, 10 h, and natural cooling, respectively. XRD patterns of the obtained samples showed the $SrTiO_3$ phase only as shown in Figure 2-14. The crystallinity of the samples were evaluated from the FWHM of (110) peak (Table 2-2). The crystallinity of the samples became better with increasing the amount of $SrCl_2$ up to $SrCl_2/SrTiO_3$ = 0.1 but lowered with further increase of the $SrCl_2$ gradually. It seems that for $SrCl_2/SrTiO_3$ = 0.01 and 0.1, the amount of $SrCl_2$ was not enough for all $SrTiO_3$ to dissolve in. The morphology of the particles observed by SEM also supports this speculation (Figure2-15). For the sample prepared with

$SrCl_2/SrTiO_3$ = 0.01, the morphology of the particles were very similar to STO(wako). Small particles of a few hundred nanometers were agglomerated into secondary particles of a few micrometers in size. The minor difference between these samples was that the primary particles of STO(wako) were irregular in shape while primary particles STO($SrCl_2$) treated with of $SrCl_2/SrTiO_3$ = 0.01 were mostly cubic. This cubic shape of primary particles could be due to the dissolution and recrystallization occurred only on the surface of $SrTiO_3$ which was in direct contact with $SrCl_2$. The morphology of the particles drastically changed when $SrCl_2$ was increased from $SrCl_2/SrTiO_3$ = 0.01 to 0.1. Most of the particles observed were free from agglomeration and rather imperfect cubic although some were cubic. The size distribution of this sample was the largest among the samples prepared. Small particles were a few hundred nanometers in size but some particles were larger than 10 μm. This is probably due to repeated dissolution and recrystallization. The amount of $SrCl_2$ at $SrCl_2/SrTiO_3$ = 0.1 was not large for all $SrTiO_3$ to dissolve in but probably large enough to partly dissolve $SrTiO_3$. The constant dissolution and recrystallization result in particles free from agglomeration. However, because the amount of $SrCl_2$ was not sufficient to completely dissolve $SrTiO_3$, an excess amount of $SrTiO_3$ were consumed to grow on other $SrTiO_3$ particles, producing larger particles with the shape deviating from its ideal cubic shape. It seems that the mixture experienced liquid phase when $SrCl_2/SrTiO_3$ = 1.0, 10, and 20. Almost all particles had cubic shapes and they were free from agglomerates. The BET surface areas of the samples are tabulated in Table 2-2. The surface area seemed to be reasonable based on the morphology change observed from SEM. The surface area decreased from 3.6 m^2 g^{-1} for STO(wako) to 0.3 m^2 g^{-1} for $SrCl_2/SrTiO_3$ = 0.1. When the amount of $SrCl_2$ further increased from 0.1 to 10, the surface area gradually increased from 0.3 to 0.9 m^2 g^{-1}.

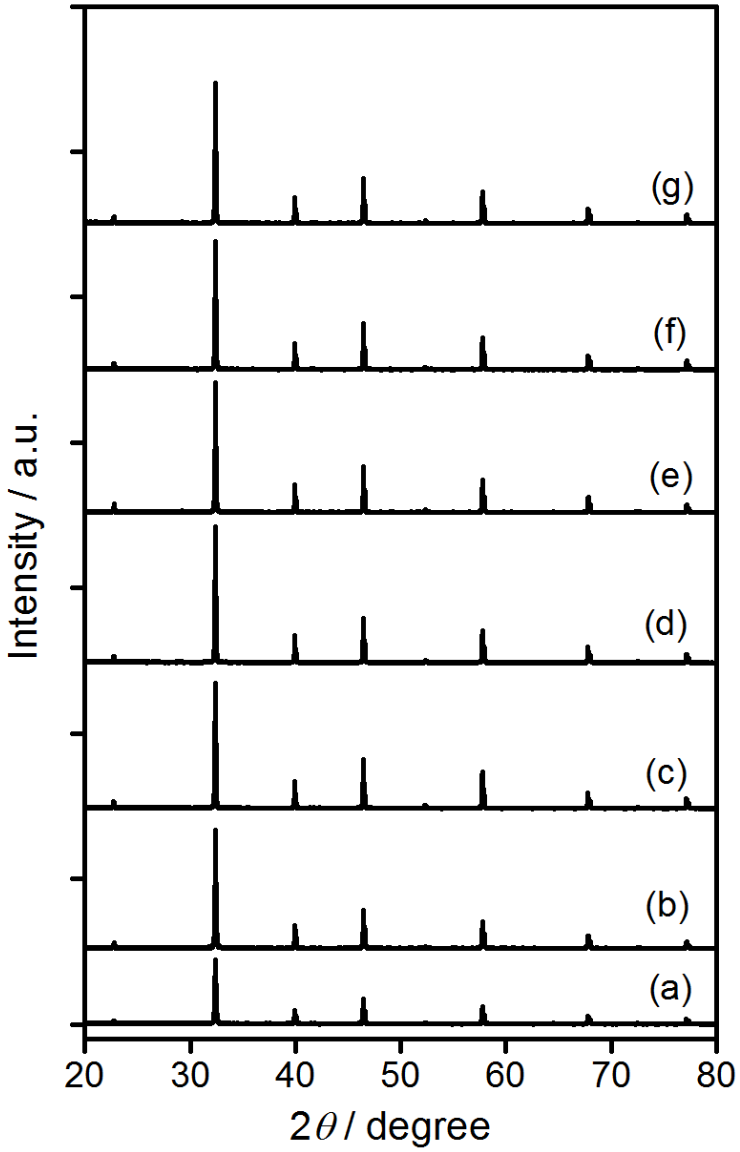

Figure 2-14. XRD patterns of (a) STO(wako) and STO($SrCl_2$) treated with different amount of $SrCl_2$. $SrCl_2$/$SrTiO_3$ = (b) 0.01, (c) 0.1, (d) 1.0, (e) 5, (f) 10 and (g) 20.

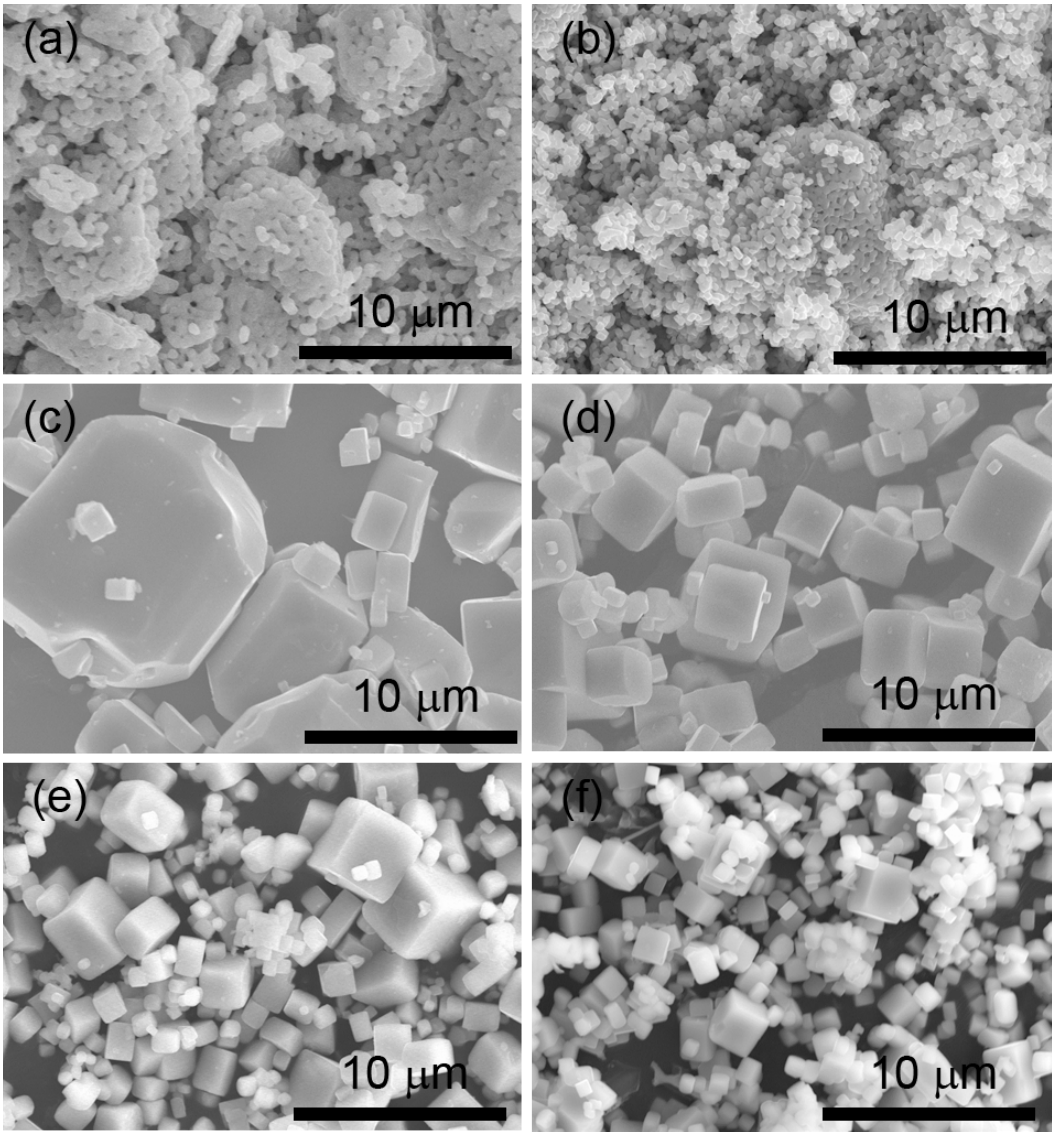

Figure 2-15.SEM images of (a) STO(wako) and STO($SrCl_2$) treated with different amount of $SrCl_2$. $SrCl_2/SrTiO_3$ = (b) 0.01, (c) 0.1, (d) 1.0, (e) 5, (f) 10 and (g) 20.

Table 2-2. FWHM of (110) peak in XRD pattern, BET surface area, and molar ratio analyzed by ICP-OES of STO($SrCl_2$) treated with different amount of $SrCl_2$.

Molar ratio of $SrCl_2/SrTiO_3$	FWHM of (110) peak in XRD pattern* / °	BET surface are / m^2 g^{-1}	Molar ratio 2[Al]/([Sr]+[Ti])
STO(wako)	0.103	3.6	0.04%
0.01	0.084	1.9	0.20%
0.1	0.058	-	0.19%
1	0.061	< 0.3	0.18%
5	0.064	0.5	-
10	0.066	0.9	0.31%
20	0.066		-

*(110) peaks due to Cu $K_{\alpha1}$ and $K_{\alpha2}$ was deconvoluted to evaluate the FWHM originating from Cu $K_{\alpha1}$ radaition.

2.3.2. Photocatalytic Overall Water Splitting on Flux-Treated $SrTiO_3$ Particles

The water splitting activity of STO(wako), and $SrTiO_3$ treated with NaCl, KCl, and $SrCl_2$ are presented in Figure 2-16. Compared to STO(wako), which showed water splitting activity of about 5.1 H_2-μmol h^{-1} and 2.6 O_2-μmol h^{-1}, STO(flux) showed two orders of magnitude higher activity, regardless of the types of flux used. STO($SrCl_2$) showed the highest water splitting activity, reaching 448 H_2-μmol h^{-1} and 234 O_2-μmol h^{-1}, among the flux examined. The apparent quantum efficiency, AQE, of STO($SrCl_2$) in the overall water splitting reaction was 30% at 360 nm. This is much higher than the previously reported value of 4.3% at 350 nm for KCl-treated $SrTiO_3$.[26] To elucidate the reason for this improved water splitting activity,

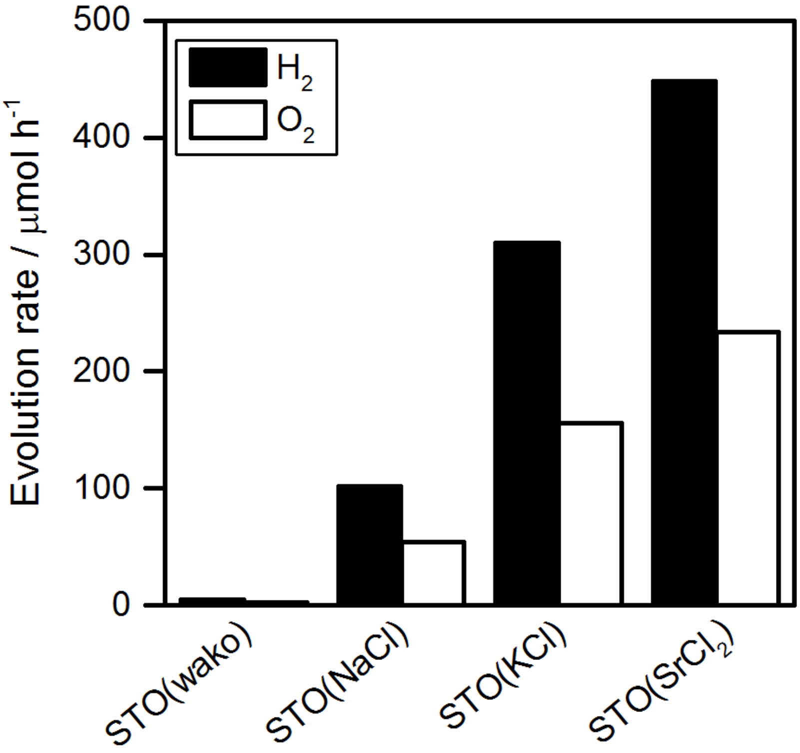

Figure 2-16. Evolution rate during the water splitting reaction on STO(wako), STO(NaCl), STO(KCl), and STO(SrCl$_2$). Reaction conditions: Catalyst, 0.1 g; Cocatalyst, $Rh_{2-y}Cr_yO_3$ (Rh 0.3 wt%, Cr 0.3 wt%); Reaction solution, 100 mL H_2O; Light source, 300 W Xe lamp (λ>300 nm).

treatment condition of STO(SrCl$_2$) was further examined. It should be noted that all the $SrTiO_3$ powders discussed in this study split water into hydrogen and oxygen with constant rate at least for 5 hours as presented in Figure 2-17.

The water splitting activity of STO(SrCl$_2$) treated at different temperatures became markedly higher when the treatment temperature increased (Figure 2-18). The water splitting activity of STO(SrCl$_2$) treated at 900 °C was about 20 times higher than STO(wako). When the treatment temperature was increased from 900 °C to 1000 °C, the water splitting activity of the obtained STO(SrCl$_2$) photocatalyst improved about 20 times. When the treatment temperature was further incensed to 1100 °C the activity remained almost the same. This enhancement in water splitting activity of STO(SrCl$_2$) had no direct relationship with their BET

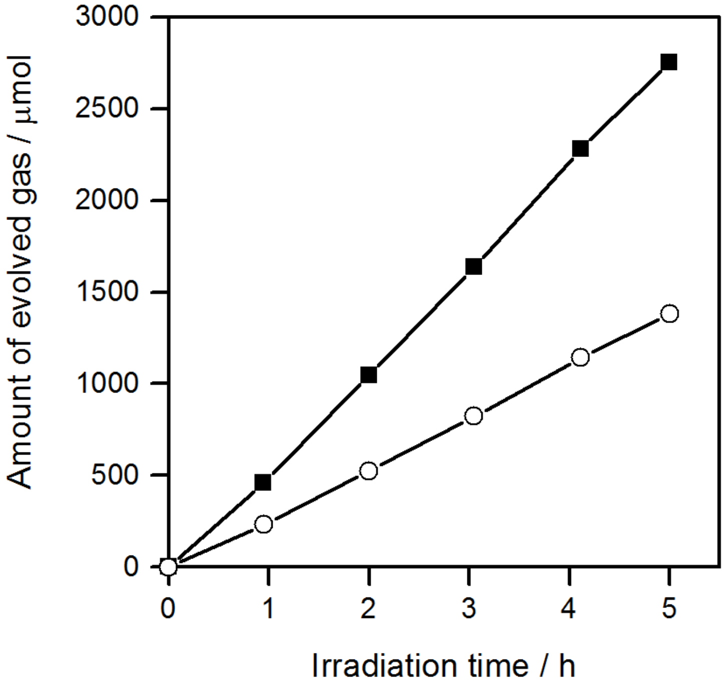

Figure 2-17. Gas evolution during the water splitting reaction on STO($SrCl_2$). H_2(■) and O_2(□). Reaction conditions: Catalyst, 0.1 g; Cocatalyst, $Rh_{2-y}Cr_yO_3$ (Rh 0.1 wt%, Cr 0.1 wt%); Reaction solution, 100 mL H_2O; Light source, 300 W Xe lamp (λ>300 nm).

surface area (Table 2-1) as it was reported.[26] Though their FWHM of the (110) peak decreased with increasing the treatment temperature, the relationship between the water splitting activity and the crystallinity was not linear to each other. Therefore, it is reasonable to suspect that the improvement in crystallinity is not the sole reason for the enhanced activity of STO($SrCl_2$)

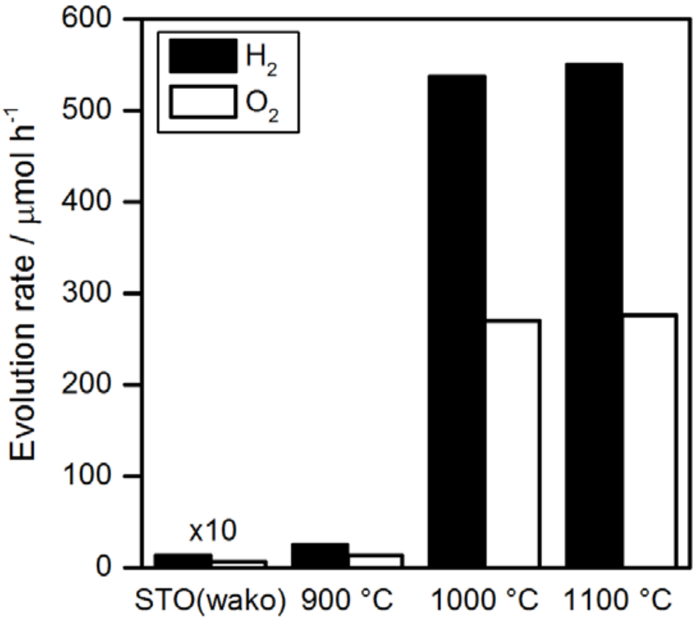

Figure 2-18. Evolution rate during the water splitting reaction on STO(wako) and STO($SrCl_2$) samples treated with different temperatures. Reaction conditions: Catalyst, 0.1 g; Cocatalyst, $Rh_{2-y}Cr_yO_3$ (Rh 0.3 wt%, Cr 0.3 wt%); Reaction solution, 100 mL H_2O; Light source, 300 W Xe lamp (λ>300 nm).

The water splitting activity of STO($SrCl_2$) treated with different soak times and different cooling rates are tabulated in Table 2-3. The water splitting activity of STO($SrCl_2$) had no clear relationship with either the soak times or the cooling rates. Still, they all showed large enhancement in the activity compared to STO(wako) though the magnitude of the enhancement was different. Since varying either soak times or cooling rates resulted in little change in the morphology and crystallinity of STO($SrCl_2$), as was explained in section 2.3.1, this result again supports the existence of another factor that influences the water splitting activity of STO($SrCl_2$) other than its crystallinity.

Table 2-3.Gas evolution rate during the water splitting reaction on STO($SrCl_2$) treated with different soak times and cooling rates.

Soak time / h	Cooling rate	Evolution rate / μmol h^{-1}	
		H_2	O_2
1	Natural	390	210
10	Natural	440	40
20	Natural	420	220
10	6	380	200
10	30	500	270

Reaction conditions: Catalyst, 0.1 g; Cocatalyst, $Rh_{2-y}Cr_yO_3$ (Rh 0.3 wt%, Cr 0.3 wt%); Reaction solution, 100 mL H_2O; Light source, 300 W Xe lamp (λ >300 nm).source.

The water splitting activity of STO($SrCl_2$) treated with different amounts of $SrCl_2$ is shown in Figure 2-19. The activity of STO($SrCl_2$) increased with increasing the amounts of $SrCl_2$ up to $SrCl_2/SrTiO_3$ = 5 and reached plateau upon further increase. This enhancement in the water splitting activity of STO($SrCl_2$) had no direct relationship with their BET surface areas or with their FWHM of the (110) peak (Table 2-2). The existence of another factor that influences the water splitting activity of STO($SrCl_2$) other than the crystallinity is now quite clear. Since the water splitting activity of STO($SrCl_2$) increased with increasing the temperature and with increasing amount of $SrCl_2$ to some extent, incorporation of impurity into STO($SrCl_2$) is suspected. No conspicuous impurity peak was observed in STO($SrCl_2$) treated at 1100 °C and with $SrCl_2/SrTiO_3$ = 10 from XPS or EDS analysis. However, with ICP analysis it was revealed that very small amounts of Al (< 1%) were indeed incorporated into STO($SrCl_2$). It seems that Al impurity was derived from the alumina crucibles during the flux treatment. The amount of Al detected by ICP-OES was

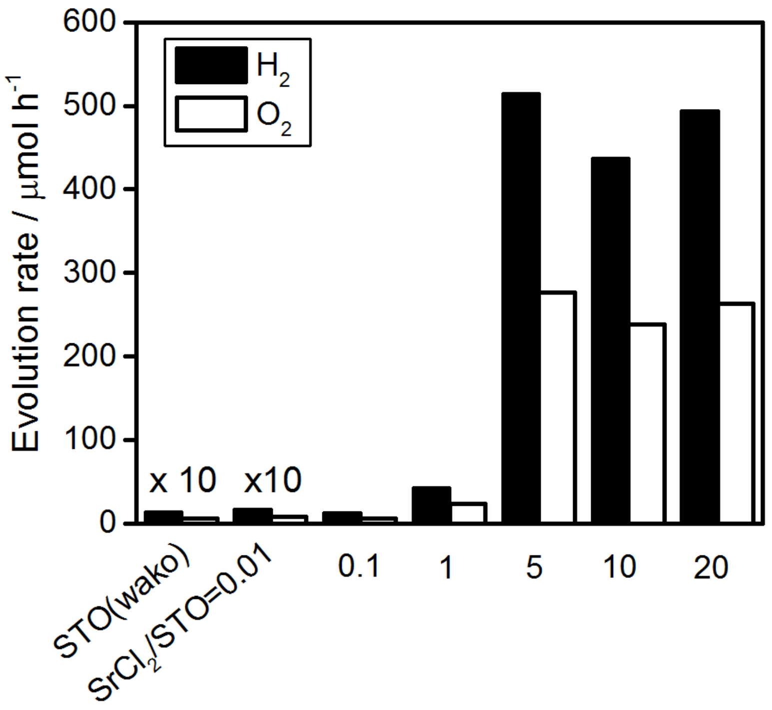

Figure 2-19. Evolution rate during the water splitting reaction on STO(wako) and STO($SrCl_2$) samples treated with different molar ratio of $SrCl_2/SrTiO_3$. Reaction conditions: Catalyst, 0.1 g; Cocatalyst, $Rh_{2-y}Cr_yO_3$ (Rh 0.3 wt%, Cr 0.3 wt%); Reaction solution, 100 mL H_2O; Light source, 300 W Xe lamp (λ>300 nm).

analyzed quantitatively and tabulated in Table 2-1 and Table 2-2. XPS and EDS failed to detect Al since their detection limits are around 1%.

It has been reported that doping $SrTiO_3$ with lower valence cations can boost its photocatalytic activity.[27] Commonly, as-synthesized $SrTiO_3$ has oxygen vacancies. These oxygen vacancies will result in trivalent Ti species as presented in equation 2.1.

$$SrTiO_3 = SrTiO_{3-x} + \tfrac{1}{2}xO_2 + 2xe^- + xV_0 = SrTi^{4+}{}_{1-2x}Ti^{3+}{}_{2x}O_{3-x} + \tfrac{1}{2}xO_2 + xV_0 \quad (2.1)$$

This trivalent Ti species is reported to work as a recombination site of excited charges. The incorporation of lower valence cation into $SrTiO_3$ into the Sr sit and the Ti site could suppress the formation of this trivalent Ti species. Since Al is the most stable as trivalent species. When Al^{3+} is incorporated into $SrTiO_3$, it would substitute the Ti^{4+} site, considering their ionic radii (Ti^{4+}: 74.5 pm, Al^{3+}: 67.5 pm). Al impurity incorporated into $SrTiO_3$ could suppress the formation of trivalent Ti species. The effect of Al doping will be further discussed in the next section.

2.3.3. Effect of Al Doping on $SrTiO_3$ Particles during the Flux Treatment

To synthesize $SrCl_2$ treated $SrTiO_3$ which is free from Al impurity, yttria crucibles were used for the treatment as presented in Figure 2-1. The XRD patterns of STO($SrCl_2$-Y) showed only peaks attributable to the $SrTiO_3$ phase as it is presented in Figure 2-20(a). The FWHM of the (110) XRD peak was 0.103° for STO(wako) and it was reduced to 0.071 for STO($SrCl_2$-Y) (Table 2-4). This reduction of FWHM indicates improved crystallinity as it was mentioned in section 2.3.1. The SEM image of STO($SrCl_2$-Y) is shown in Figure 2-21(b). The morphology of STO($SrCl_2$-Y) particles was cubic with 0.2–2 μm in size. From these two results it could be concluded that the $SrCl_2$ treatment in an yttria crucible results in $SrTiO_3$ particles with high crystallinity, similar to the $SrCl_2$ treatment in an alumina crucible. The slight difference in their average particle size seems to come from the different shapes of the crucible used. The average particle size of $SrTiO_3$ powder obtained by the flux treatment is greatly affected by the shape of crucible used as it was discussed in the appendix. The BET surface area of STO($SrCl_2$-Y) was much smaller than STO(wako), and larger than STO($SrCl_2$) prepared under same condition to STO($SrCl_2$-Y) but in alumina crucible (Table 2-4). This result well agreed with the difference in their particle sizes. For the $SrTiO_3$ samples treated in yttria crucibles, both Al and Y elements were quantitatively analyzed by ICP-OES (Table 2-4). As expected, STO($SrCl_2$-Y) was free of Al, but instead, it was doped with Y from the yttria crucibles.

Table 2-4. FWHM of (110) peak in XRD pattern, BET surface area, and molar ratio determined by ICP-OES of STO($SrCl_2$) treated with different amount of $SrCl_2$.

Sample	FWHM of (110) peak in XRD pattern* / °	BET surface are / m^2 g^{-1}	Molar ratio	
			2[Al]/([Sr]+[Ti])	2[Y]/([Sr]+[Ti])
STO(wako)	0.103	3.6	0.04%	0.00%
STO($SrCl_2$-Y)	0.071	1.5	0.02%	0.48%
0.1%Al STO($SrCl_2$-Y)	0.067	0.9	0.12%	0.16%
1%Al STO($SrCl_2$-Y)	0.096	2.7	1.01%	0.70%
10%Al STO($SrCl_2$-Y)	0.091	2.4	1.36%	0.57%

*(110) peaks due to Cu $K_{\alpha1}$ and $K_{\alpha2}$ was deconvoluted to evaluate the FWHM originating from Cu $K_{\alpha1}$ radaition.

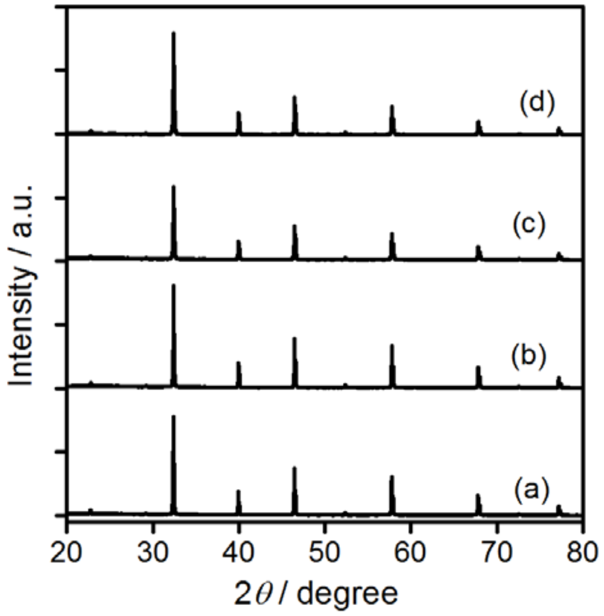

Figure 2-20. XRD patterns of (a) STO($SrCl_2$-Y), (b) 0.1%Al STO($SrCl_2$-Y), (c) 1%Al STO($SrCl_2$-Y), and (d) 10%Al STO($SrCl_2$-Y).

In an attempt to control Al doping in the presence of the $SrCl_2$ flux, $SrTiO_3$ and Al_2O_3 were mixed at molar ratios of Al/Ti = 0.1%, 1%, 10%, 30%, and 100% and heated together with the $SrCl_2$ flux in yttria crucibles as shown in Figure 2-1. The XRD patterns, SEM images, and BET surface areas of the samples are presented in Figure 2-20, Figure2-21, and Table 2-4, respectively. The amount of Al doped was not directly proportional to the amount of Al_2O_3 added, but did increase with it (Table 2-4). In addition, certain amounts of Y were introduced from the yttria crucibles, similar to the case for the STO($SrCl_2$-Y) sample. 0.1%Al-STO($SrCl_2$-Y) exhibited an XRD pattern similar to that of STO($SrCl_2$). Single-phase $SrTiO_3$ was observed, and the FWHM of the (110) diffraction peak was 0.067. The morphology and BET surface area for 0.1%Al-STO($SrCl_2$-Y) were also comparable to those for STO($SrCl_2$). The XRD patterns of 1%Al-STO($SrCl_2$-Y) to 100%Al-STO($SrCl_2$-Y) also showed only phases assignable to $SrTiO_3$ phase. The FWHM of the (110) peaks of 1%Al-STO($SrCl_2$-Y) and 10%Al-STO($SrCl_2$-Y) was smaller than that of STO(wako) but larger than 0.1%Al-STO($SrCl_2$-Y). The particle size of *x*%Al-STO($SrCl_2$-Y) decreased upon Al addition. The crystals of 1%Al-STO($SrCl_2$-Y) were mostly cubic, and their the average particle size became much smaller than 0.1%Al-STO($SrCl_2$-Y). The crystals of 10%Al-STO($SrCl_2$-Y) started to lose clear crystal facets, though most of them were cubic. 30%Al-STO($SrCl_2$-Y) and 100%Al-STO($SrCl_2$-Y) both consisted of irregular particles. This change in the morphologies indicates that the excess Al_2O_3 can suppress the crystal growth of $SrTiO_3$ in flux. The clear mechanism of this crystal growth process is yet to be elucidated, but the similar phenomena could be found for $NaTaO_3$ doped La.[10,35]

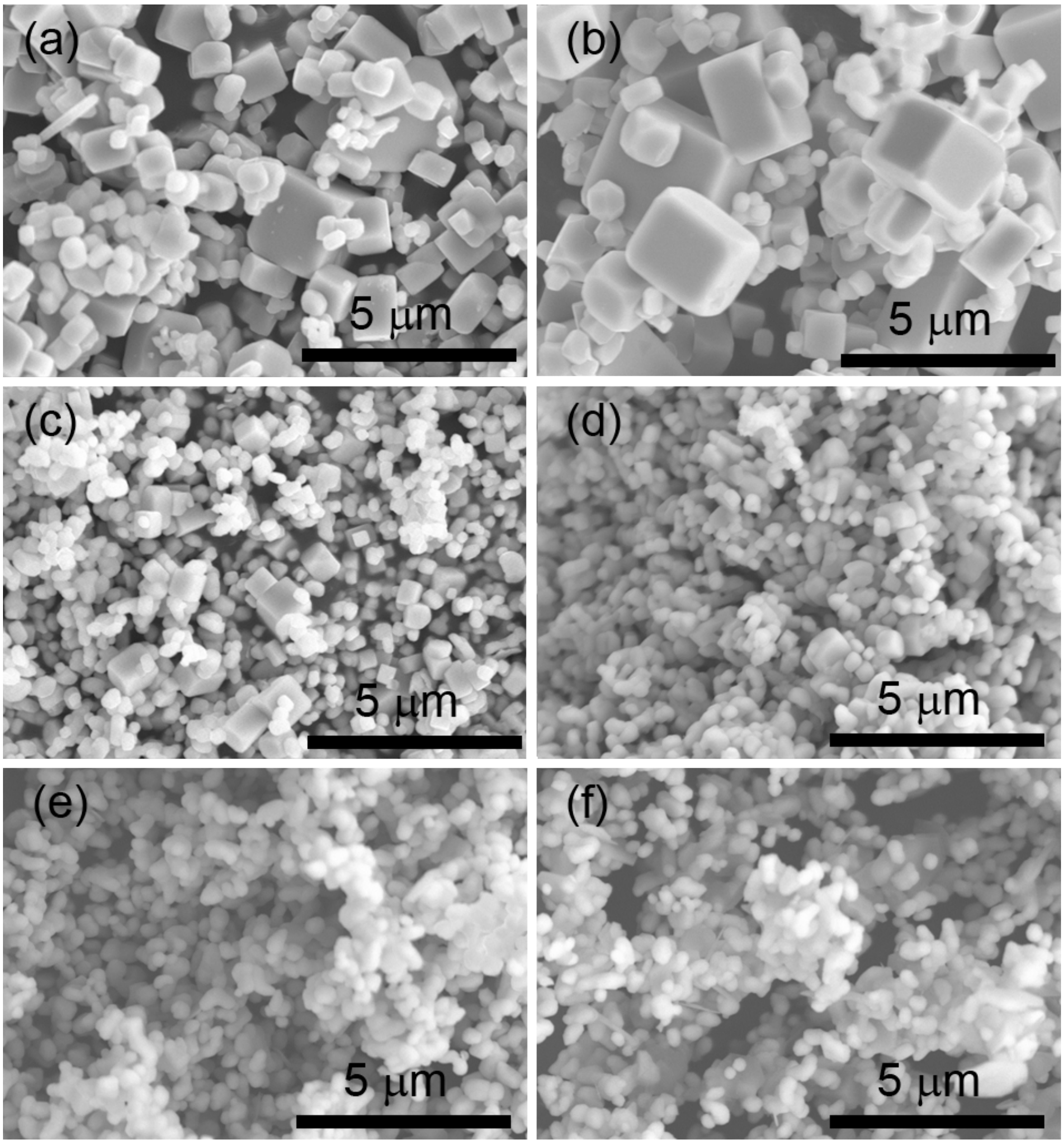

Figure 2-21. SEM images of (a) STO($SrCl_2$-Y), (b) 0.1%Al STO($SrCl_2$-Y), (c) 1%Al STO($SrCl_2$-Y), (d) 10%Al STO($SrCl_2$-Y), (e) 30%Al STO($SrCl_2$-Y), and (f) 100%Al STO($SrCl_2$-Y).

Figure 2-22 shows the water splitting activities of STO($SrCl_2$-Y) and *x*%Al-STO($SrCl_2$-Y). The water splitting activity of STO(wako) was roughly tripled upon $SrCl_2$ flux treatment in an yttria crucible. This is presumably due to the improvement in crystallinity. However, this improvement was much smaller than the improvement observed for the STO($SrCl_2$) which was treated in an alumina crucible. The FWHM of the (110) XRD peak for STO($SrCl_2$) treated at 1100 °C in alumina crucible and STO($SrCl_2$-Y) were 0.066 and 0.071°, respectively (Table 2-1, 2-4). This might explain the large difference in the enhancement of photocatalytic activity by $SrCl_2$ flux treatment in alumina and yttria crucibles. However, FWHM of the (110) XRD peak for STO($SrCl_2$) treated at 900 °C at 1000 °C were 0.084 and 0.074, both lager than that of STO($SrCl_2$-Y). It is clear that the improved water splitting activity upon flux treatment was not exclusively due to the crystallinity. A high activity for the overall water splitting reaction, comparable to that for STO($SrCl_2$), treated at 1100 °C was obtained using an yttria crucible when more than 1% of Al was added. This result suggests that Al doping is the controlling factor for the enhancement of photocatalytic activity of $SrTiO_3$. On the other hand, the high activity of 10%Al-STO($SrCl_2$-Y) despite its comparatively lower crystallinity may have resulted from the small particle sizes, which shorten the time needed for the migration of photoexcited carriers from the interior to the surface of photocatalyst particles.[36]

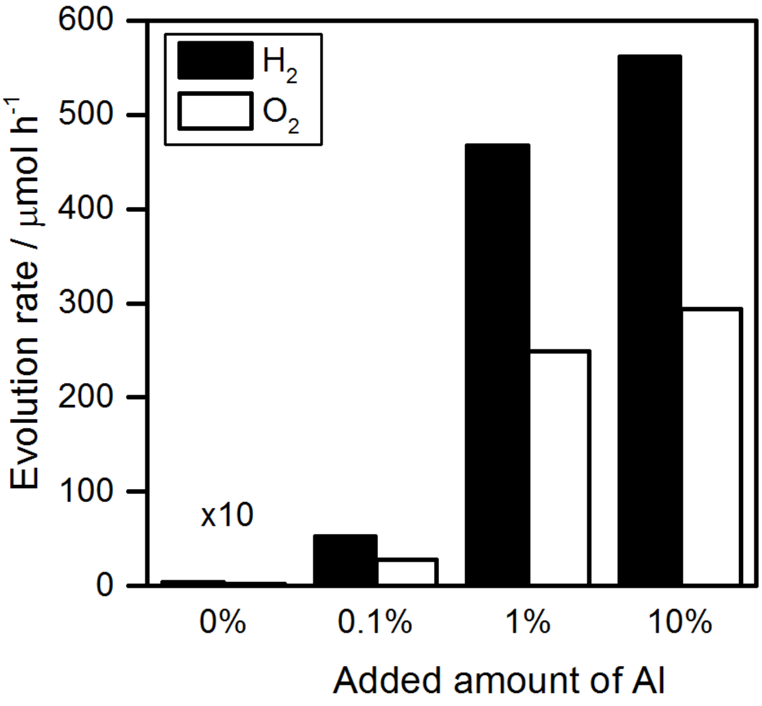

Figure 2-22. Evolution rate during the water splitting reaction on *x*%Al STO($SrCl_2$-Y). Reaction conditions: Catalyst, 0.1 g; Cocatalyst, $Rh_{2-y}Cr_yO_3$ (Rh 0.1 wt%, Cr 0.1 wt%); Reaction solution, 100 mL H_2O; Light source, 300 W Xe lamp (λ>300 nm).

To examine the effect of aluminum doping separately, Al_2O_3 was added as a dopant to $SrTiO_3$ at Al/Ti molar ratios ranging from 0.1% to 10%, and the mixtures were calcined in the absence of the $SrCl_2$ flux for a solid state reaction as shown in Figure 2-1. As tabulated in Table 2-5, the Al content increased monotonically with increasing amount of Al_2O_3 addition, although the amounts detected were somehow lower than the amounts added to the starting material for high Al_2O_3 contents (Al >5%). At this doping amount, no impurity phase was detected in the XRD patterns of the sample (Figure 2-23). As tabulated in Table 2-5, the BET surface areas of 5%Al- and 10%Al-STO(ssr) were larger than that of STO(wako), probably due to the presence of unreacted, amorphous Al_2O_3. The BET surface area of 1% Al-STO(ssr) was smaller than that of STO(wako), probably owing to the sintering process. The BET surface 0.1%Al-STO(ssr) was much smaller than that of STO(wako). This magnitude of decrease in the surface area was quite large for sintering process. I suspect that abnormal crystal growth occurred for this sample as in the case of Al_2O_3 added $BaTiO_3$,[37] due to the small amount of Al_2O_3 in the starting mixture. It should be noted that no significant difference in the morphology was observed between STO(wako) and *x*%Al-STO(ssr) as shown in Figure 2-24. These results suggest the necessity of the $SrCl_2$ flux for the improvement in crystallinity and the morphological change. The amount of Al incorporated into $SrTiO_3$ had a significant influence on the water splitting activity of the resulting samples. The water splitting activity peaked for 0.1%Al-STO(ssr), as shown in Figure 2-25.

Table 2-5. FWHM of (110) peak in XRD pattern, BET surface area, and molar ratio determined by ICP-OES of x%Al-STO(ssr).

Sample	FWHM of (110) peak in XRD pattern* / °	BET surface are / m^2 g^{-1}	Molar ratio 2[Al]/([Sr]+[Ti])
0.1%Al-STO(ssr)	0.077	1.7	0.10%
1%Al-STO(ssr)	0.094	3.0	1.07%
5%Al-STO(ssr)	0.095	3.7	4.24%
10%Al-STO(ssr)	0.096	3.9	8.25%

*(110) peaks due to Cu $K_{\alpha1}$ and $K_{\alpha2}$ was deconvoluted to evaluate the FWHM originating from Cu $K_{\alpha1}$ radaition.

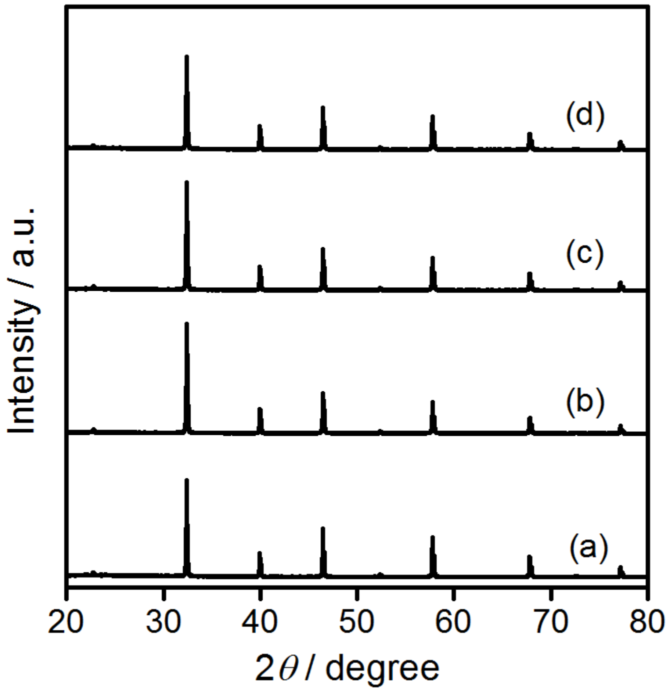

Figure 2-23. XRD patterns of (a) 0.1%Al-, (b) 1%Al-, (c) 5%Al-, and (d) 10%Al-STO(ssr).

It should be noted that Al doping of $SrTiO_3$ was more effective when $SrCl_2$ was present during the heating. The doping amount of Al in the STO($SrCl_2$) sample from an alumina crucible may vary depending on the treatment conditions. Nevertheless, this sample showed a higher photocatalytic activity than the *x*%Al-STO(ssr) samples containing various and controlled amounts of Al. It is thought that Al was not effectively doped into $SrTiO_3$ during the solid state reaction because Al had to diffuse from the outer surface of the particles. In contrast, a significant portion of the $SrTiO_3$ particles was once dissolved and recrystallized in the presence of $SrCl_2$ flux, together with alumina derived from the crucibles. During this process, some of the Al ions may be doped into the middle part of the $SrTiO_3$ particles and occupy the most stable state thermodynamically. As a result, Al doping can show stronger enhancement of photocatalytic activity when the $SrCl_2$ flux is used. Thus, it is concluded that the dramatic improvement in

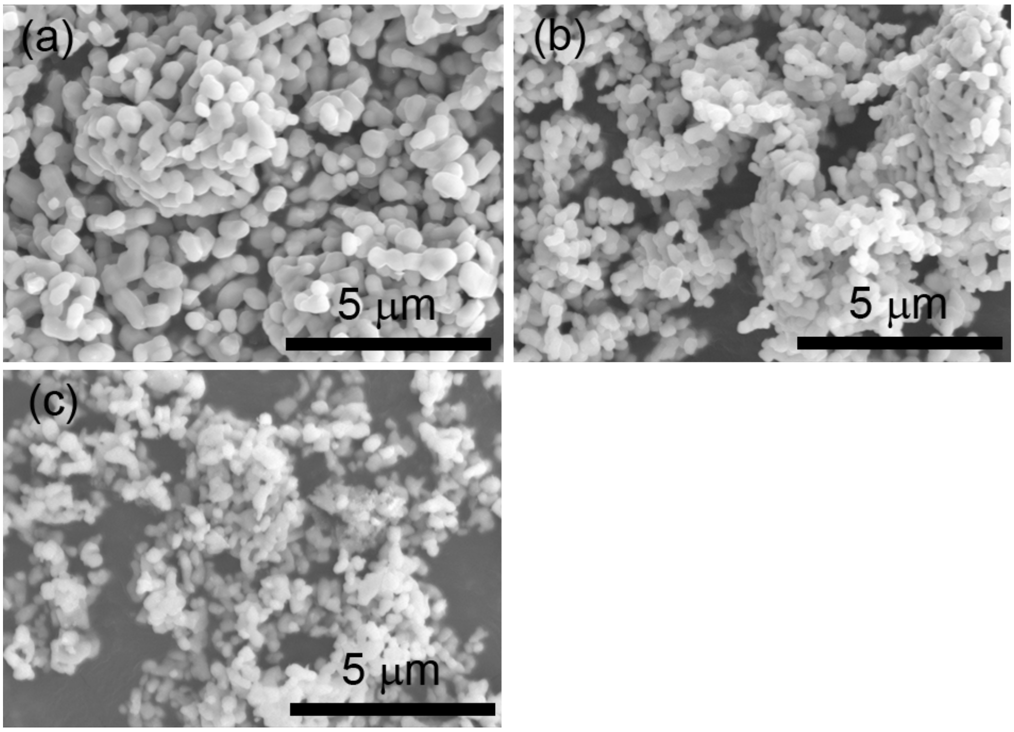

Figure 2-24.SEM images of (a) 0.1%Al-, (b) 1%Al-, (c) 5%Al-, and (d) 10%Al-STO(ssr).

the photocatalytic activity of STO($SrCl_2$) was due to Al doping and the enhancement of crystallinity observed upon flux treatment.

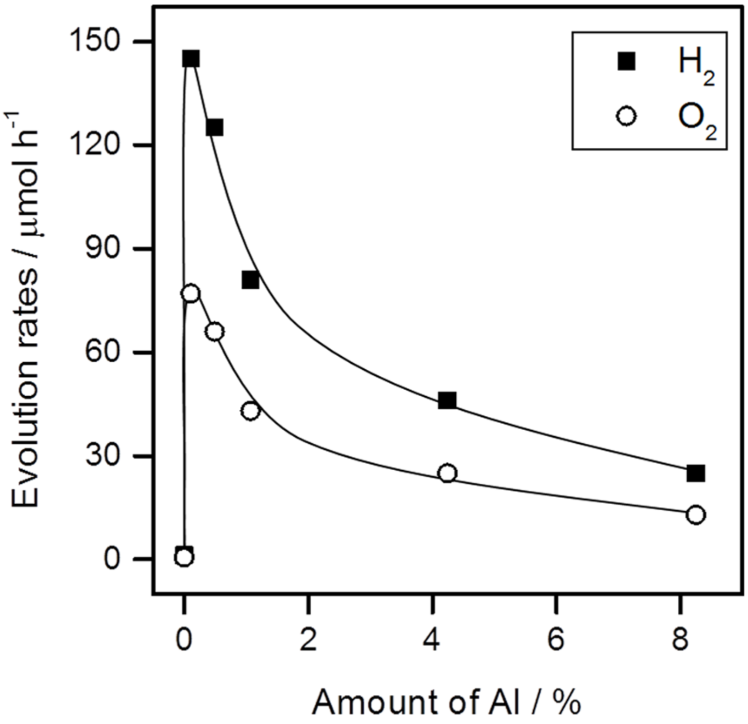

Figure 2-25. Dependence of the water splitting activity of STO(ssr-Y) on the amount of Al doping. Reaction conditions: Catalyst, 0.1 g; Cocatalyst, $Rh_{2-y}Cr_yO_3$ (Rh 0.1 wt%, Cr 0.1 wt%); Reaction solution, 100 mL H_2O; Light source, 300 W Xe lamp (λ >300 nm).

2.3.4. Effect of Cation Doping on $SrTiO_3$ Particles

From section 2.3.3, it was revealed that the Al doping on $SrTiO_3$ was a more dominant factor than the flux treatment. Therefore, further cation doping was examined. STO(wako) was used to examine the effect of the addition of various metal ions. The water splitting activity of M-STO(wako) is presented in Figure 2-26. Relatively high photocatalytic activity was obtained by the addition of Li^+, Na^+, K^+, Rb^+, Cs^+, Mg^{2+}, Al^{3+}, Ga^{3+}, and In^{3+} ions, while the photocatalytic activity was not enhanced drastically by the addition of

Ca^{2+}, Ba^{2+}, Y^{3+} and La^{3+}ions. As it was mentioned in section 2.3.2, improvement of the photocatalytic activity for overall water splitting was achieved by doping lower valence cations into $SrTiO_3$.[24] The results in Figure 2-26 almost agree with this explanation. The addition of Mg^{2+} ion is also effective to enhance the highly photocatalytic activity. This is probably caused by exchange of the Ti^{4+} in $SrTiO_3$ with Mg^{2+}. The results clearly demonstrate that the addition of lower valence cations which can replace to Sr^{2+} ion or Ti^{4+} ion to $SrTiO_3$ by an impregnation method also improves the photocatalytic activity of $SrTiO_3$ in overall water splitting remarkably.

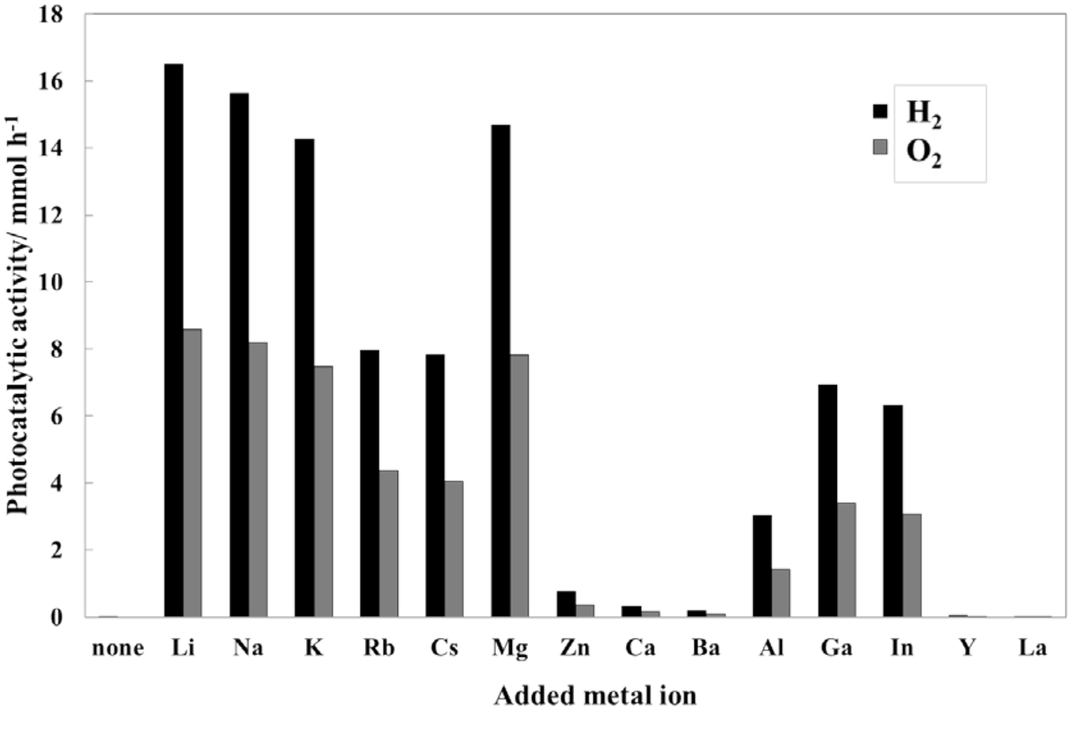

Figure 2-26. Evolution rate during the water splitting reaction on 1.5%M-STO(wako). Reaction conditions: Catalyst, 0.3 g; Cocatalyst, $Rh_{2-y}Cr_yO_3$ (Rh 0.1 wt%, Cr 0.1 wt%); Reaction solution, 400 mL H_2O; Light source, 450 W high pressure Hg lamp.

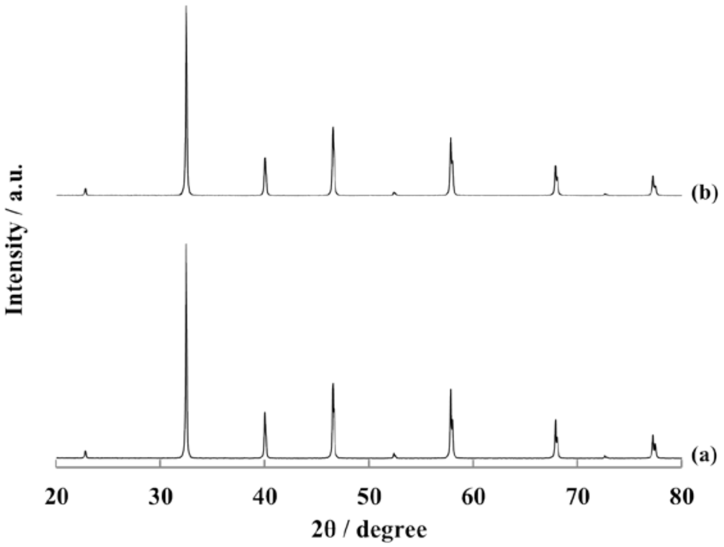

Figure 2-27. XRD patterns of (a) STO(PC) and (b)2% NaSTO(PC).

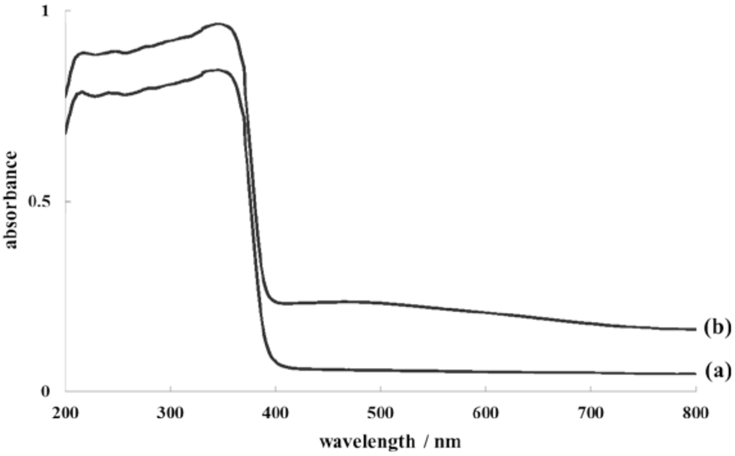

Figure 2-28. UV-vis spectra of (a) STO(PC) and (b) 2%Na-STO(PC).

The Na addition was chosen for the further examination of the cation doping. $SrTiO_3$ was synthesized by a polymerizable complex method (STO(PC)) and Na was subsequently added by an impregnation method (Na-STO(PC)). The XRD pattern, and absorption spectrum of 2%Na-STO(PC) are presented in Figure 2-27 and Figure 2-28, respectively. No significant changes were observed before and after the addition of Na in the XRD pattern and absorption spectrum. The surface areas of STO(PC) and 2%Na-STO(PC) were 1.7 m^2 g^{-1} and similar to each other. These results show that the Na-addition had no significant influence on the morphology of $SrTiO_3$. The state of the 2%Na-STO(PC) was examined in detail by TEM (Figure 2-29). 2%Na-STO(PC) consisted of fine particles with up to several hundred nm in size. No significant changes in surface morphology was observed. These results suggest that the addition of Na to $SrTiO_3$ do not change its the surface morphology.

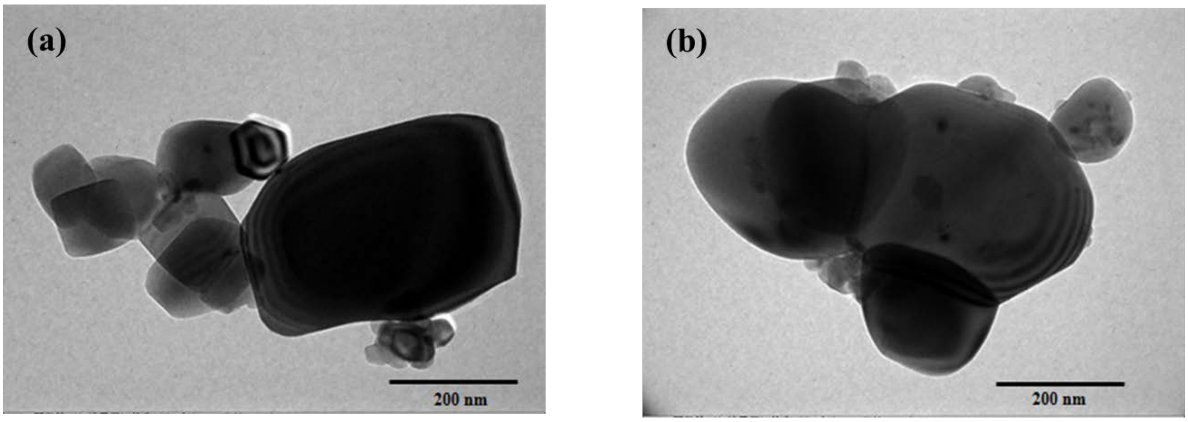

Figure 2-29. TEM images of $SrTiO_3$(PC) (a) before and (b) after Na(2 atm %) addition.

Figure 2-30 shows a STEM photograph of 2%Na-STO(PC) and the distribution of Sr, Ti and Na estimated from the results of EDS simultaneously measured with the STEM photograph. As shown in Fig. 2-30d, Na^+ ions were confirmed to disperse homogeneously in the $SrTiO_3$ particle. This result suggests that addition of Na give no significant influence to the morphology and crystallography of $SrTiO_3$. The added

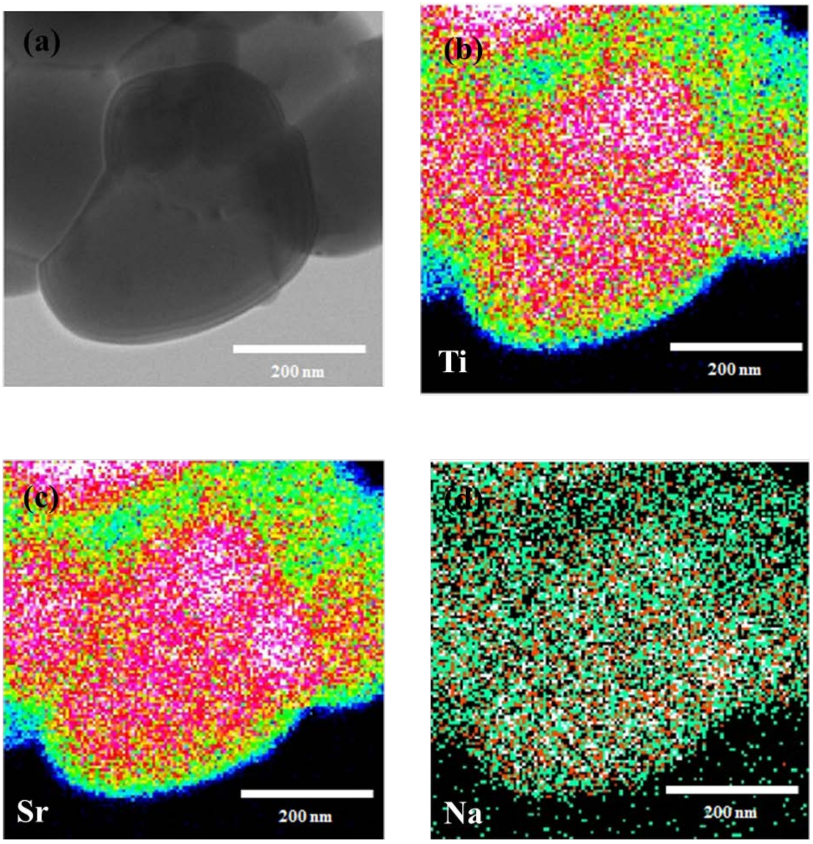

Figure 2-30. STEM image (a) and the distribution of (b) Ti, (c) Sr and (d) Na measured by EDS in 2%Na- $SrTiO_3$(PC).

Na may exchange Sr ions in the $SrTiO_3$ crystal and induce the same effects as doping Na at the preparation atmosphere. This probably leads to the remarkable improvement of the photocatalytic activity to the overall water splitting.

Figure 2-31 shows water splitting activity of 2%Na-STO(PC) compared to that of STO(PC). H_2 and O_2 produced in the stoichiometric ratio of overall water splitting from the beginning of the reaction over both of the photocatalysts. The activity of 2%Na-STO(PC) was remarkably higher than that of STO(PC). This clearly shows that the addition of Na by impregnation to $SrTiO_3$ has positive effect on its photocatalytic activity.

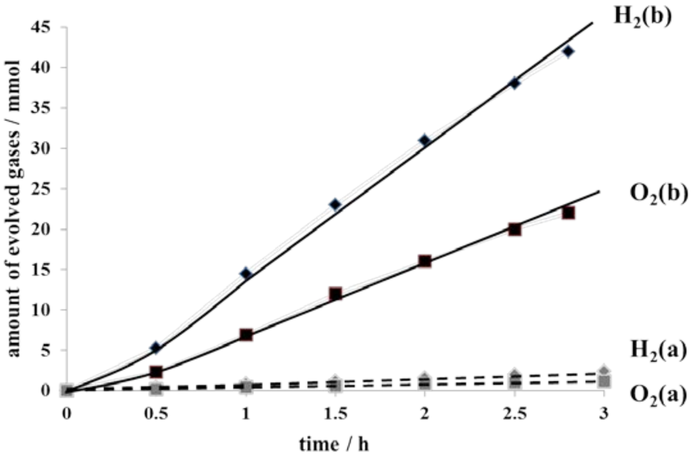

Figure 2-31. Gas evolution during the water splitting reaction on (a) STO(PC) and (b)2%Na-STO(PC). Reaction conditions: Catalyst, 0.3 g; Cocatalyst, $Rh_{2-y}Cr_yO_3$ (Rh 0.3 wt%, Cr 0.5 wt%); Reaction solution, 400 mL H_2O; Light source, 450 W high pressure Hg lamp.

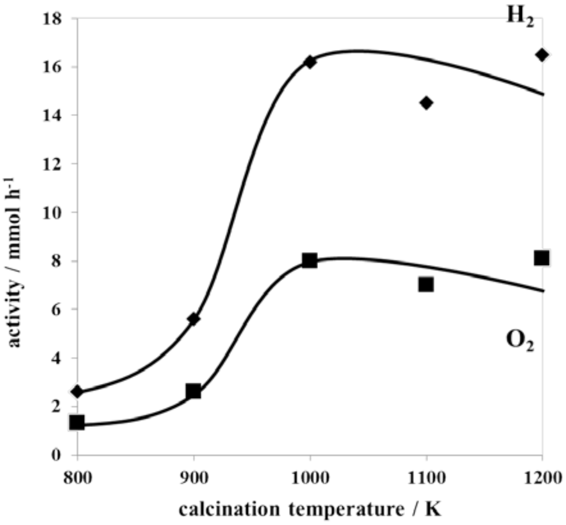

Figure 2-32. Photocatalytic activity of 2%Na-STO(PC) depend on the calcination temperature. Catalyst, 0.3 g; Cocatalyst, $Rh_{2-y}Cr_yO_3$ (Rh 0.3 wt%, Cr 0.5 wt%); Reaction solution, 400 mL H_2O; Light source, 450 W high pressure Hg lamp.

Figure 2-32 shows the photocatalytic activity of 2%Na-STO(PC) to the overall H_2O splitting as a function of the calcination temperatures. The photocatalytic activity is noticed to depend on the calcination temperature. Particularly, the photocatalytic activity remarkably improved when Na-STO(PC) was prepared at over 1273 K. It could be concluded that high temperature is necessary to generate the effects of the Na addition. Therefore, strong interaction between added Na ion and $SrTiO_3$, such as substitution of Na ion to Sr ion in $SrTiO_3$, seems to be necessary to obtain high photocatalytic activity.

2.3.6. Relationship between Light Intensity and Water Splitting Activity of $SrTiO_3$

The apparent quantum efficiency, AQE, of STO(STO($SrCl_2$) was measured to be 30% at 360 nm. This is much higher than the 4.3% reported for KCl-treated $SrTiO_3$, although the difference in reaction conditions should be taken into account.[26] It is worth mentioning that the apparent quantum efficiency was in fact dependent on the intensity of the incident light. As shown in Figure 2-34, the AQE increased with light intensity under the experimental conditions examined. This result is not consistent with reaction orders to light intensity commonly observed in photocatalytic reactions, which is a first order.[37] It is possible that a certain kind of trap state with a limited density may have to be filled with photoexcited carriers to attain sufficient photoconductivity for charge separation.

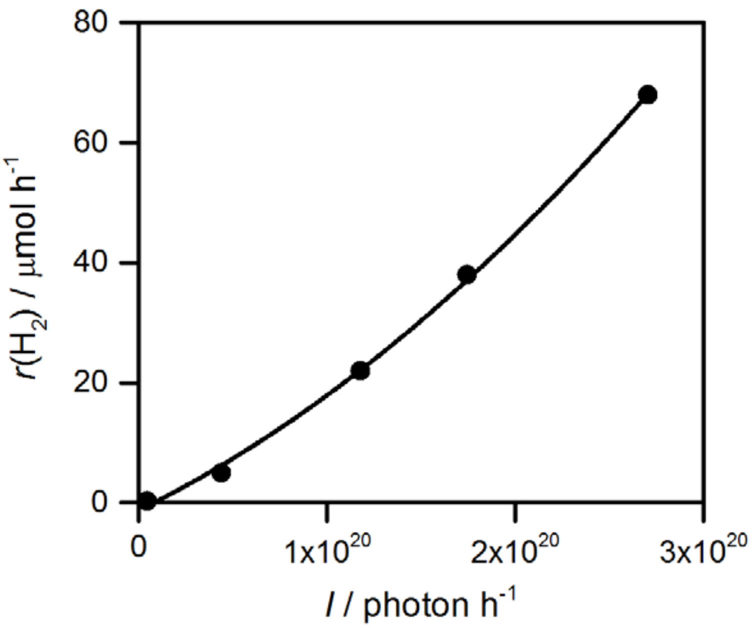

Figure 2-34 Dependence of the water splitting activity of STO(flux-Al) on light intensity. Reaction conditions: Catalyst, 0.1 g; Cocatalyst, $Rh_{2-y}Cr_yO_3$ (Rh 0.3 wt%, Cr 0.3 wt%); Reaction solution, 150 ml H_2O; Light source, 450 W high-pressure Hg lamp (λ = 360 nm, FWHM= 10 nm).

2.4. Conclusions

The photocatalytic activity of $SrTiO_3$ in the overall water splitting reaction was dramatically improved by $SrCl_2$ flux treatment at 1100 °C in an alumina crucible. The improvement in activity was attributed mainly to the doping of Al derived from the crucibles. The morphological change and the enhanced crystallinity also improved the photocatalytic activity, although these factors were found to be less significant than the effect of Al doping on the basis of the results of flux treatment in Al-free conditions.

It was confirmed that $SrTiO_3$ doped with Al under a $SrCl_2$ flux showed even higher water splitting activity than $SrTiO_3$ doped with Al by a solid state reaction. It is believed that the flux worked as a medium to dissolve the Al_2O_3 dopant and the host $SrTiO_3$ particles, facilitating the Al doping of $SrTiO_3$. As a consequence, the apparent quantum efficiency in overall water splitting was increased to 30% at 360 nm. Flux-mediated doping is expected to greatly broaden the possibilities of photocatalytic materials by activating them under visible light irradiation. In addition, the incorporation of impurities into the samples during flux treatment was a common occurrence and could have strong impact on the photocatalytic activity. Therefore, particular attention should be paid to flux treatment of photocatalysts.

The crystallinity and water splitting activity of $SrTiO_3$ were dramatically improved by the flux treatment in alumina crucibles. A small amount of Al doped into $SrTiO_3$ from an alumina crucible was found to be responsible for the enhancement in photocatalytic activity. It was found that the external doping of Al in the presence of flux was the most effective for controlled Al doping and produced an apparent quantum efficiency exceeding 30% at 360 nm, the highest value reported so far in this wavelength region and on $SrTiO_3$ powder.

The influences of the addition of metal ions to $SrTiO_3$ were further investigated. The addition of Li^+, Na^+, K^+, Rb^+, Cs^+, Mg^{2+}, Al^{3+}, Ga^{3+}, and In^{3+} ions effectively improved the photocatalytic activity of $SrTiO_3$ to overall water splitting. Remarkable improvement of the photocatalytic activity of $SrTiO_3$ was observed by the addition of Na^+ ion by impregnation method. The activity was 16 mmol/h for H_2 and 8 mmol/h for O_2 production, respectively, and the apparent quantum yield of the photocatalytic reaction was 16 % under the irradiation through a band-pass filter at 360 nm.

References

[1] K. Maeda, K. Teramura, D. Lu, T. Takata, N. Saito, Y. Inoue, and K. Domen, “Photocatalyst releasing hydrogen from water,” *Nature*, vol. 440, no. 7082, pp. 295–295, 2006.

[2] Y. Lee, H. Terashima, Y. Shimodaira, K. Teramura, M. Hara, H. Kobayashi, K. Domen, and M. Yashima, “Zinc germanium oxynitride as a photocatalyst for overall water splitting under visible light,” *The Journal of Physical Chemistry C*, vol. 111, no. 2, pp. 1042–1048, 2007.

[3] K. Maeda, D. Lu, and K. Domen, “Direct water splitting into hydrogen and oxygen under visible light by using modified taon photocatalysts with d^0 electronic configuration,” *Chemistry-A European Journal*, vol. 19, no. 16, pp. 4986–4991, 2013.

[4] J. Xu, C. Pan, T. Takata, and K. Domen, “Photocatalytic overall water splitting on the perovskite-type transition metal oxynitride $CaTaO_2N$ under visible light irradiation,” *Chemical Communications*, vol. 51, no. 33, pp. 7191–7194, 2015.

[5] C. Pan, T. Takata, M. Nakabayashi, T. Matsumoto, N. Shibata, Y. Ikuhara, and K. Domen, “A complex perovskite-type oxynitride: The first photocatalyst for water splitting operable at up to 600 nm,” *Angewandte Chemie*, vol. 127, no. 10, pp. 2998–3002, 2015.

[6] Y. Sakata, Y. Matsuda, T. Nakagawa, R. Yasunaga, H. Imamura, and K. Teramura, “Remarkable improvement of the photocatalytic activity of Ga_2O_3 towards the overall splitting of H_2O,” *ChemSusChem*, vol. 4, no. 2, pp. 181–184, 2011.

[7] Y. Sakata, T. Nakagawa, Y. Nagamatsu, Y. Matsuda, R. Yasunaga, E. Nakao, and H. Imamura, “Photocatalytic properties of gallium oxides prepared by precipitation methods toward the overall splitting of H_2O,” *Journal of Catalysis*, vol. 310, pp. 45–50, 2014.

[8] Y. Sakata, T. Hayashi, R. Yasunaga, N. Yanaga, and H. Imamura, “Remarkably high apparent quantum yield of the overall photocatalytic H_2O splitting achieved by utilizing Zn ion added Ga_2O_3 prepared using dilute $CaCl_2$ solution,” *Chemical Communications*, vol. 51, no. 65, pp. 12 935–12 938, 2015.

[9] A. Kudo and H. Kato, “Effect of lanthanide-doping into $NaTaO_3$ photocatalysts for efficient water splitting,” *Chemical Physics Letters*, vol. 331, no. 5, pp. 373–377, 2000.

[10] K. Teshima, K. Horita, T. Suzuki, N. Ishizawa, and S. Oishi, “Flux growth and characterization of layered $K_4Nb_6O_{17}$ crystals,” *Chemistry of materials*, vol. 18, no. 16, pp. 3693–3697, 2006.

[11] S. Suzuki, K. Teshima, A. Yamaguchi, K. Yubuta, T. Shishido, and S. Oishi, “Fabrication and photocatalytic performance of highly crystalline nanosheets derived from flux-grown KNb_3O_8 crystals,” *CrystEngComm*, vol. 14, no. 3, pp. 987–992, 2012.

[12] K. Teshima, K. Yubuta, T. Shimodaira, T. Suzuki, M. Endo, T. Shishido, and S. Oishi, “Environmentally friendly growth of highly crystalline photocatalytic $Na_2Ti_6O_{13}$ whiskers from a NaCl flux,” *Crystal Growth & Design*, vol. 8, no. 2, pp. 465–469, 2008.

[13] H. Yoshida, M. Takeuchi, M. Sato, L. Zhang, T. Teshima, and M. G. Chaskar, “Potassium hexatitanate photocatalysts prepared by a flux method for water splitting,” *Catalysis Today*, vol. 232, pp. 158–164, 2014.

[14] D. Noureldine, D. H. Anjum, and K. Takanabe, “Flux-assisted synthesis of $SnNb_2O_6$ for tuning photocatalytic properties,” *Physical Chemistry Chemical Physics*, vol. 16, no. 22, pp. 10 762–10 769, 2014.

[15] F. Zhang, A. Yamakata, K. Maeda, Y. Moriya, T. Takata, J. Kubota, K. Teshima, S. Oishi, and K. Domen, “Cobalt-modified porous single-crystalline $LatTiO_2N$ for highly efficient water oxidation under visible light,” *Journal of the American Chemical Society*, vol. 134, no. 20, pp. 8348–8351, 2012.

[16] M. J. Bojdys, J.-O. Müller, M. Antonietti, and A. Thomas, “Ionothermal synthesis of crystalline, condensed, graphitic carbon nitride,” *Chemistry-A European Journal*, vol. 14, no. 27, pp. 8177–8182, 2008.

[17] T. Takata, D. Lu, and K. Domen, “Synthesis of structurally defined Ta_3N_5 particles by flux-assisted nitridation,” *Crystal Growth & Design*, vol. 11, no. 1, pp. 33–38, 2010.

[18] T. Sugai, S. Hasegawa, and G. Ohara, Growth of strontium titanate single crystals from molten salts,” *Japanese Journal of Applied Physics*, vol. 7, no. 4, pp. 358–362, 1968.

[19] G. Muller, A. Ostrogorsky, and D. Hurle, “Flux growth” *Handbook of Crystal Growth*. North Holland Amsterdam, 1994, ch. 4, sec. 2, pp. 573–574.

[20] K. Domen, S. Naito, M. Soma, T. Onishi, and K. Tamaru, “Photocatalytic decomposition of water vapour on an NiO–$SrTiO_3$ catalyst,” *Journal of the Chemical Society, Chemical Communications*, no. 12, pp. 543–544, 1980.

[21] R. Asai, H. Nemoto, Q. Jia, K. Saito, A. Iwase, and A. Kudo, “A visible light responsive rhodium and antimony-codoped $SrTiO_3$ powdered photocatalyst loaded with an IrO_2 cocatalyst for solar water splitting,” *Chemical Communications*, vol. 50, no. 19, pp. 2543–2546, 2014.

[22] K. Furuhashi, Q. Jia, A. Kudo, and H. Onishi, “Time-resolved infrared absorption study of $SrTiO_3$ photocatalysts codoped with rhodium and antimony,” *The Journal of Physical Chemistry C*, vol. 117, no. 37, pp. 19 101–19 106, 2013.

[23] T. Takata and K. Domen, “Defect engineering of photocatalysts by doping of aliovalent metal cations for efficient water splitting,” *The Journal of Physical Chemistry C*, vol. 113, no. 45, pp. 19 386–19 388, 2009.

[24] Q. Wang, T. Hisatomi, S. S. K. Ma, Y. Li, and K. Domen, “Core/shell structured La-and Rh-codoped $SrTiO_3$ as a hydrogen evolution photocatalyst in z-scheme overall water splitting under visible light irradiation,” *Chemistry of Materials*, vol. 26, no. 14, pp. 4144–4150, 2014.

[25] H. Kato, M. Kobayashi, M. Hara, and M. Kakihana, “Fabrication of $SrTiO_3$ exposing characteristic facets using molten salt flux and improvement of photocatalytic activity for water splitting,” *Catalysis Science & Technology*, vol. 3, no. 7, pp. 1733–1738, 2013.

[26] T. K. Townsend, N. D. Browning, and F. E. Osterloh, “Overall photocatalytic water splitting with NiO_x– $SrTiO_3$–a revised mechanism,” *Energy & Environmental Science*, vol. 5, no. 11, pp. 9543–9550, 2012.

[27] K. Maeda, K. Teramura, H. Masuda, T. Takata, N. Saito, Y. Inoue, and K. Domen, “Efficient overall water splitting under visible-light irradiation on $(Ga_{1-x}Zn_x)(N_{1-x}O_x)$ dispersed with Rh-Cr mixed-oxide nanoparticles: Effect of reaction conditions on photocatalytic activity,” *The Journal of Physical Chemistry B*, vol. 110, no. 26, pp. 13 107–13 112, 2006.

[28] T. Sano, D. M. Saylor, and G. S. Rohrer, “Surface energy anisotropy of $SrTiO_3$ at 1400 ˚ C in air,” *Journal of the American Ceramic Society*, vol. 86, no. 11, pp. 1933–1939, 2003.

[29] M. Matsumura, M. Hiramoto, and H. Tsubomura, “Photoelectrolysis of water under visible light with doped $SrTiO_3$ electrodes,” *Journal of The Electrochemical Society*, vol. 130, no. 2, pp. 326–330, 1983.

[30] A. Kahn and A. Leyendecker, “Electronic energy bands in strontium titanate,” *Physical Review*, vol. 135, no. 5A, p. A1321, 1964.

[31] M. Capizzi and A. Frova, “Optical gap of strontium titanate (deviation from urbach tail behavior),” *Physical Review Letters*, vol. 25, no. 18, p. 1298, 1970.

[32] K. Van Benthem, C. Elsässer, and R. French, “Bulk electronic structure of $SrTiO_3$: Experiment and theory,” *Journal of Applied Physics*, vol. 90, no. 12, pp. 6156–6164, 2001.

[33] B. Wanklyn and B. Watts, “Nucleation sites on platinum surfaces in flux growth,” *Materials Research Bulletin*, vol. 19, no. 6, pp. 711–716, 1984.

[34] A. Iwase, H. Kato, and A. Kudo, “The effect of alkaline earth metal ion dopants on photocatalytic water splitting by natao3 powder,” *ChemSusChem*, vol. 2, no. 9, pp. 873–877, 2009.

[35] A. Kudo and Y. Miseki, “Heterogeneous photocatalyst materials for water splitting,” *Chemical Society Reviews*, vol. 38, no. 1, pp. 253–278, 2009.

[36] J. G. Fisher, B.-K. Lee, S.-Y. Choi, S.-M. Wang, and S.-J. L. Kang, “Inhibition of abnormal grain growth in $BaTiO_3$ by addition of Al_2O_3,” *Journal of the European Ceramic Society*, vol. 26, no. 9, pp. 1619–1628, 2006.

[37] T. Hisatomi, K. Maeda, K. Takanabe, J. Kubota, and K. Domen, “Aspects of the water splitting mechanism on $(Ga_{1-x}Zn_x)(N_{1-x}O_x)$ photocatalyst modified with $Rh_{2-y}Cr_yO_3$ cocatalyst,” *The Journal of Physical Chemistry C*, vol. 113, no. 51, pp. 21 458–21 466, 2009.

Chapter 3: Excited Carrier Dynamics in Particulate $SrTiO_3$ Samples

3.1. Introduction

$SrTiO_3$ is one of the most widely used materials for optical and electronic devices, owing to the large dielectric constant, strong nonlinear optical effect, and ferroelectricity. It is also used as a photocatalyst since it is nontoxic and stable during photocatalytic reactions.[1–4] Furthermore, it functions as a visible-light-responsive photocatalyst when doped with impurities such as Cr, Ni and Rh: doping induces visible light absorption and promotes photocatalytic reactions under visible light.[2–4] For optoelectronic devices, well defined single crystals are often used, but for photocatalysts, the powder form may preferred because the surface area of powder is much larger than that of a single crystal. However, there is a disadvantage associated with powders: they are richer in surface defects than single crystals. It is widely believed that these defects capture photogenerated charge carriers and decrease the photo-catalytic activity. Therefore, in principle, the number of defects should be reduced in order to increase the photocatalytic activity. The flux treatment is a powerful method that can be used to this end, because dissolution and recrystallization of a photocatalytic material proceed in molten salts. It has been reported that the treatments of $CaZrTi_2O_7$,[5] Ta_3N_5,[6,7] $LaTiO_2N$,[8] and $SrTiO_3$,[9] result in well-crystallized particles exposing well-defined surfaces and enhance their photocatalytic activity. The behavior of charge carriers should be elucidated for a precise understanding of the role of flux treatment in activity enhancement because it determines the photocatalytic activity.

Time-resolved absorption spectroscopy in the visible to mid-IR region [10,11] is a powerful method for elucidating the behavior of photogenerated charge carriers as it is illustrated in Figure 3-1. Free electrons [12–20] in the conduction band (CB) give rise to broad absorption in the mid-IR region and trapped electrons and holes in mid-gap states give transient absorption peaks in the visible or near-IR (NIR) regions.[21–27] Therefore, the energy states of photogenerated charge carriers as well as their decay processes could be examined. This method was used to investigate the behavior of charge carriers in powder and single crystalline $SrTiO_3$.[11] It was elucidated that the free or shallowly trapped electrons were dominant in single crystals, while most charge carriers in powder particles are deeply trapped. However, the trapped charge carriers in $SrTiO_3$ particles have longer lifetimes than those in single crystalline $SrTiO_3$ and showed reactivity toward reactant molecules.

In this chapter, time-resolved visible to mid-IR spectroscopy was employed to study the effects of the flux treatment on the behavior of photogenerated charge carriers in $SrTiO_3$ particles prepared in Chapter 2. Relationship between the steady-state photocatalytic activity and the carrier dynamics of the $SrTiO_3$ powder was discussed.

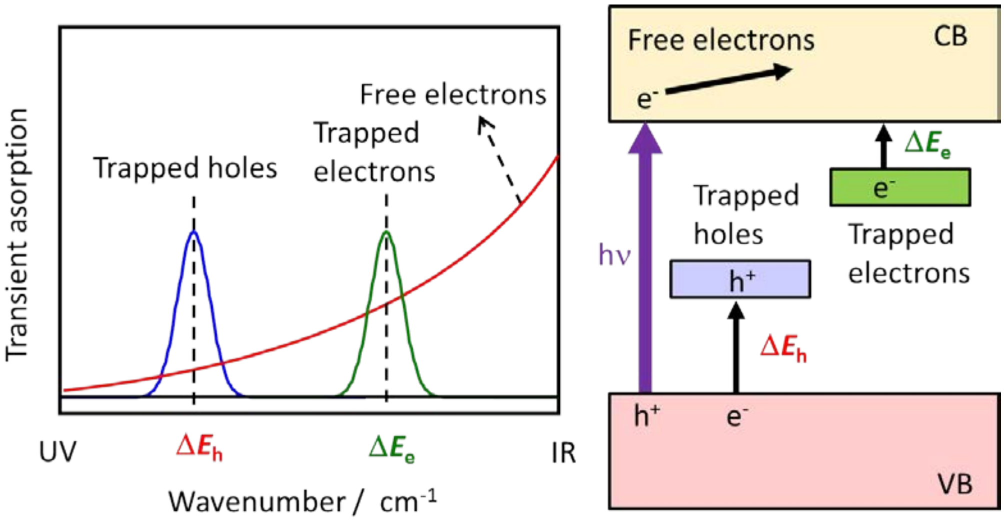

Figure 3-1. Schematic illustration of visible to mid-IR absorption spectroscopy.

3.2. Experimental Section

3.2.1. Synthesis of $SrTiO_3$ Powders

A pristine $SrTiO_3$ (STO(wako)), and $SrTiO_3$ particles treated with $SrCl_2$ flux were measured. The STO(wako) and $SrCl_2$ were thoroughly mixed with different molar ratio, and was heated at 1100 ˚C for 10 h in alumina crucibles The sample treated at the $SrCl_2/SrTiO_3$ ratio of 0.01, 0.1, 1, 10 will be referred to as STO($SrCl_2$/STO = 0.01), STO($SrCl_2$/STO = 0.1), STO($SrCl_2$/STO = 1), and STO($SrCl_2$/STO = 10), respectively in this chapter.

3.2.2. Time-Resolved Absorption Measurements

Time-resolved absorption measurements were performed with laboratory-built spectrometers as schematically shown in Figure 3-2. In the mid-IR region, the probe light emitted from $MoSi_2$ coil was focused on the sample and the transmitted light was introduced into a spectrometer (Acton, SP-2300i). The monochromatized light from the spectrometer was detected by a photovoltaic MCT (Kolmar), and temporal profiles of the signal intensity were recorded by a digital oscilloscope (Iwatsu, DS-4262). In the case of visible to NIR region, the experiments were performed in the diffuse-reflection mode. A halogen lamp (50W) and a Si-photodiode (Hamamatsu) or an InGaAs detector (Hamamatsu) were used as a light source and detectors, respectively. The powder photocatalyst was fixed on a CaF_2 plate with a density of about 1 mg cm^{-2}, and thus the obtained sample plate was placed in a stainless-steel IR cell.

The band gap of the photocatalysts was excited by 355-nm laser pulses from a Nd:YAG laser (Continuum, Surelite I, 6 ns duration, repetition rate of 10~0.2 Hz). In the visible (25,000~10,000 cm^{-1}) and near-IR (NIR; 10,000~6000 cm^{-1}) regions, the probe light from a halogen lamp (50 W) was focused on the sample, and the diffuse reflected light was monochromated by the spectrometer. The monochromated visible or NIR light was detected by a Siphotodiode or InGaAs detector, respectively. The time resolution of this spectrometer in the NIR and IR regions was 1~2 ms, limited by the AC-coupled amplifier (Stanford Research Systems, SR560), and that in the visible region was 4 ms, limited by the stray light of the pump pulse and/or short-lived strong emission from the sample.

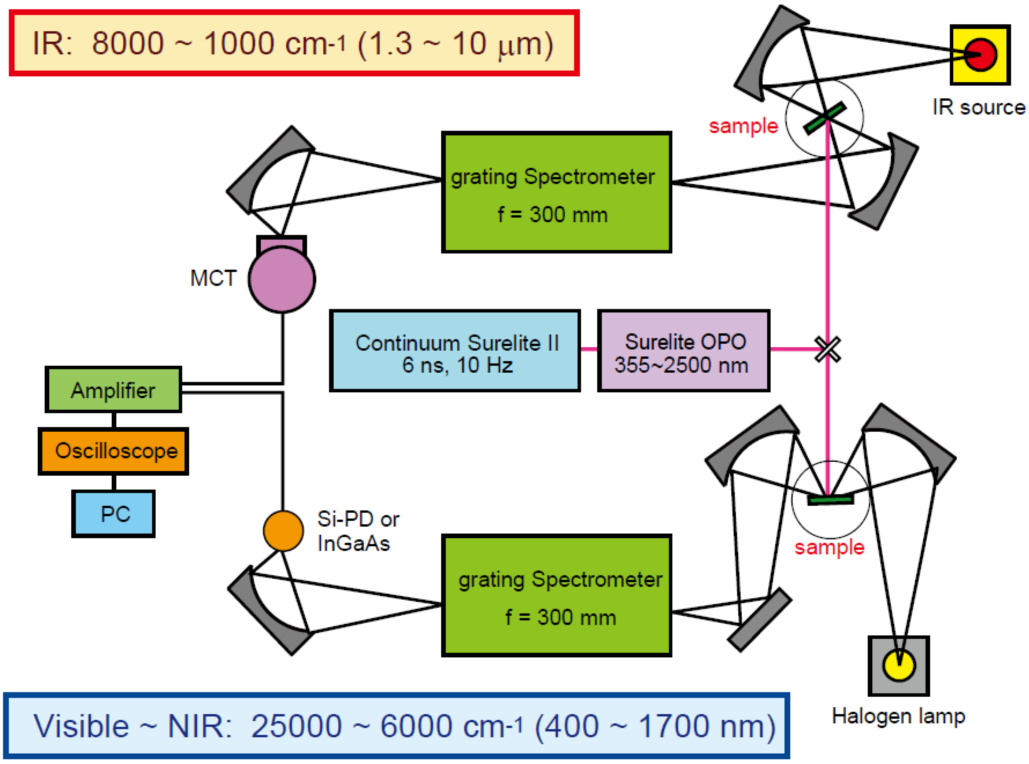

Figure 3-2. Illustration of the laboratory-built microsecond time-resolved visible, NIR and IR absorption spectrometers.

3.3. Results and Discussion

3.3.1. Behavior of Photogenerated Charge Carriers in Pristine $SrTiO_3$ Particles

Figure 3-3(a) shows the transient absorption spectra of STO(wako) particles. A clear absorption peak is observed around 11,000 cm^{-1}. This spectral shape of STO(wako) was totally different from that of other commercial $SrTiO_3$ powders purchased from Aldrich and Kojundo Co., reported elsewhere. [11]

In the case of $SrTiO_3$ powders purchased from Aldrich and Kojundo powders, three peaks appear at around 20,000, 11,000 and 2500 cm^{-1}, which are assigned to trapped holes, trapped electrons, and shallowly trapped electrons, respectively. However, in the case of the STO(wako), the absorption intensities around 20,000 and 2500 cm^{-1} were very small. This suggests that the energy states of the photogenerated charge carriers in STO(wako) are completely different from that of $SrTiO_3$ powders purchased from Aldrich and Kojundo powders.

The cause of the transient absorption is investigated by observing the decay processes of the transient absorption in the presence and absence of electron- and hole-consuming reagents, O_2 gas and MeOH vapor, respectively. Figure 3-4 shows the decay curves of the transient absorption at 2500, 11,000, and 20,000 cm^{-1} for STO(wako). The intensity change at 2500 cm^{-1} shows that the decay is accelerated by exposure to O_2 and decelerated by exposure to MeOH. Since O_2[13] and MeOH[16] consume electrons and holes, respectively, this result suggests that the intensity at 2500 cm^{-1} reflects the number of electrons. At 20,000 cm^{-1}, the decay is decelerated by the exposure to O_2. This suggests that the absorption peak at wavenumber mainly reflects the number of holes. However, the exposure to MeOH did not accelerate the decay. It is possible that the trapped holes giving the transient absorption at 20,000 cm^{-1} are less reactive with MeOH. More reactive free or shallowly trapped holes may be present in the photocatalyst, but it may not give transient absorption in the range from visible to mid-IR. Yamakata *et al.* demonstrated that no signal derived from free or shallowly trapped holes was observed in defect-free single crystalline $SrTiO_3$.[11]

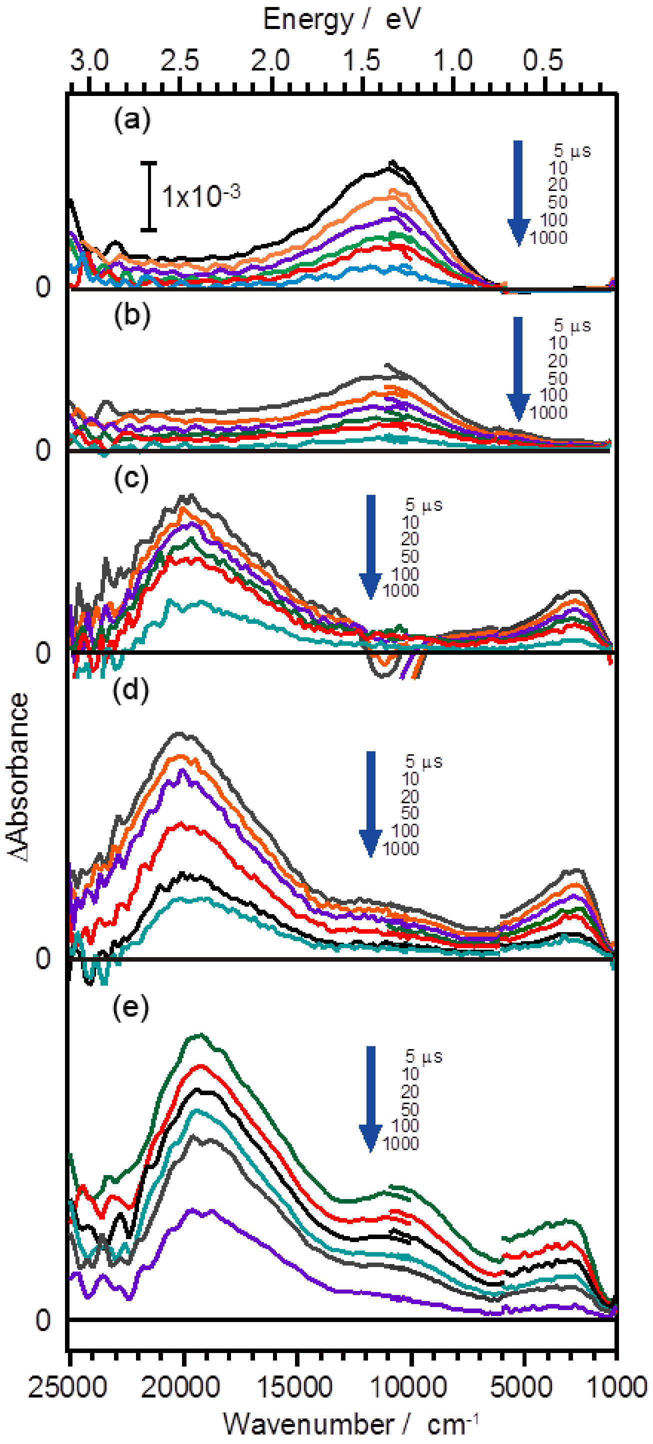

Figure 3-3. Transient absorption spectra of (a) STO(wako), and STO($SrCl_2$) treated with different amount molar ratio of $SrCl_2/SrTiO_3$ = (b) 0.01, (c) 0.1, (d) 1, and (e) 10. Pump energy was 0.5 mJ per pulse, and the repetition rate was 5 Hz.

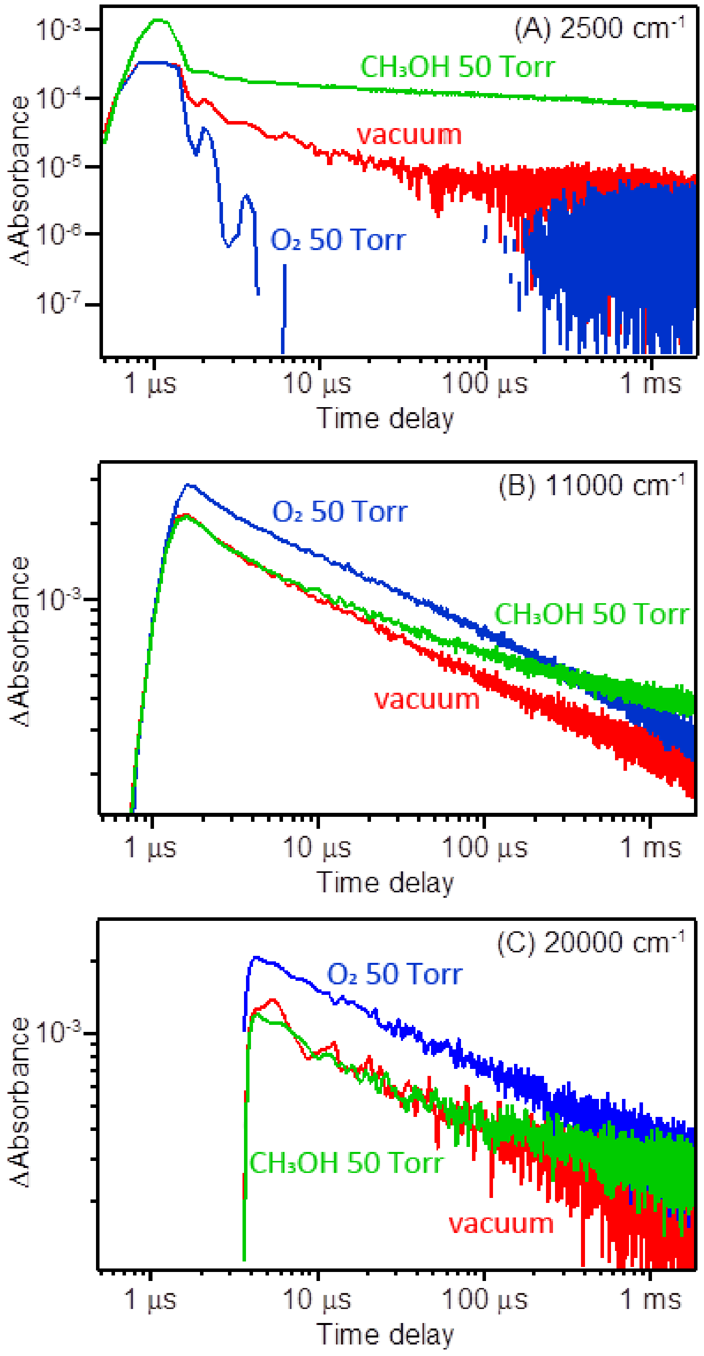

Figure 3-4. Decay curves of transient absorption of STO(wako) irradiated by 355 nm laser pulses (0.5 mJ per pulse at 0.2 Hz). The decay curves were measured at 2500 cm^{-1} (a), 11000 cm^{-1} (b), and 20000 cm^{-1} (c), in vacuum, 50 Torr O_2, and CH_3OH.

The intensity at 11,000 cm^{-1} exhibited complex changes: as shown in Figure 3-4(b), exposures to MeOH and O_2 vapors both decelerated the transient decay. This suggests that the band intensity at 11,000 cm^{-1} involves contributions from both photogenerated electrons and holes. This result can be explained as follows: the hole-consuming reaction decreases the number of holes but increases the number of surviving electrons, and vice versa. Numerical simulation [13] is useful to understand these phenomena. Therefore, the decay curves of the number of electrons and holes are calculated based on a simple model. As discussed in previous studies [10,12–14], the decay of carriers in microsecond regions follow the first-order law, suggesting that the number of electron–hole pair is less than one pair per one particle. In this case, the recombination should be represented as in equation 4.1 [13], where e–h is the electron–hole pair existing in $SrTiO_3$ particles, and k_1 is the rate constant of recombination. On the other hand, the electron and hole-consuming reactions by adsorbed O_2 and methoxy species (MeO) derived from adsorbed MeOH should be represented by equation 4.2 and 4.3, respectively, where k_2 and k_3 are the rate constants, and e_s and h_s represent the electron and hole separated from electron–hole pair in $SrTiO_3$ particles, respectively. The variable $k_2[O_2]$ and $k_3[\mathrm{MeO}]$ could be replaced by k_2' and k_3' for the simplicity. Then the rate equation for electron–hole pair and separated electron could be represented as in equation 4.4 and 4.5, respectively.

$$\mathrm{e-h} \overset{k_1}{\rightarrow} h\nu \ and\ \Delta \quad (4.1)$$

$$\mathrm{e-h} + O_2(a) \overset{k_2}{\rightarrow} {h_s}^{+} + O_2^{-}(a)\ and\ {e_s}^{-} + O_2(a) \overset{k_2}{\rightarrow} O_2^{-}(a) \quad (4.2)$$

$$\mathrm{e-h} + MeO^{-}(a) \overset{k_3}{\rightarrow} {e_s}^{-} + MeO^{\bullet}(a)\ and\ {h_s}^{+} + MeO^{-}(a) \overset{k_3}{\rightarrow} MeO^{\bullet}(a) \quad (4.3)$$

$$\frac{d[\mathrm{e-h}]}{dt} = -(k_1 + {k_2}' + {k_3}')[\mathrm{e-h}] \quad (4.4)$$

$$\frac{d[e_s]}{dt} = {k_3}'[\mathrm{e-h}] - {k_2}'[e_s] \quad (4.5)$$

For the simplicity of the model, it could be assumed that the single component of recombination and initial values at time zero were set to $[\mathrm{e} - \mathrm{h}] = 1$, $[e_s] = [h_s] = 0$. The decay curves in a vacuum were calculated by setting the rate constants to $k_1 = 0.01$, $k_2' = k_3' = 0$. In the presence of O_2, k_2' was changed to 0.002. The calculated $[e^-] = [\mathrm{e} - \mathrm{h}] + [e_s]$, $[h^+] = [\mathrm{e} - \mathrm{h}] + [h_s]$, and the sum of $[e^-]$ and $[h^+]$ are shown in

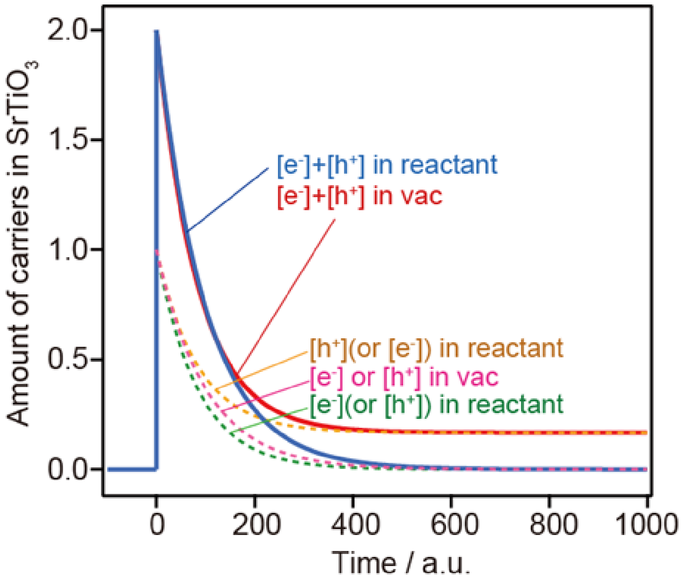

Figure 3-5. Numerically simulated decay curves of electrons, holes, and the sum of electrons and holes in $SrTiO_3$. The number of electrons and holes are calculated in the absence and presence of electron-scavenger (or hole-scavenger). The solid lines show the sum of $[e^-]$ and $[h^+]$, and the dotted lines show each of $[e^-]$ and $[h^+]$.

Figure 3-5. It was clearly shown that the decay of electrons was accelerated by the reaction with O_2, but that of holes was decelerated. As a result, the decay of the sum of $[e^-]$ and $[h^+]$ is slowed down by the exposure to O_2 compared to that in a vacuum. Essentially, the same results are obtained for MeOH, by setting the parameters to $k_2' = 0$ and $k_3' = 0.00005$. These results confirm that either the electron- or hole-consuming reaction increases the sum of the number of surviving electrons and holes, when the charge-consuming reactions proceed during the recombination. The behavior observed for the peak at 11,000 cm^{-1} for STO(wako) as in Figure 3-4(b) could be explained by these calculated results.

It has been reported in the previous paper [11] that the absorption intensity around 11,000 cm^{-1} was very sensitive to the defect structure: this absorption intensity mainly reflects the number of electrons in the case of the Aldrich powder, whereas it reflects mainly holes in the case of the Kojundo powder. These results indicate that the defects on STO(wako) particles that give transient absorption at 11,000 cm^{-1} have mixed properties with respect to those of Aldrich and Kojundo, although the detailed structure of the defects are still unknown.

3.3.2. Behavior of Photogenerated Charge Carriers on Flux-Treated Fine $SrTiO_3$ Particles

When STO(wako) was treated with $SrCl_2$ flux, the spectral shape changed dramatically, as shown in Figure 3-3(b)–(e). The peak intensity at 11,000 cm^{-1} decreased slightly for STO($SrCl_2$) treated with the molar ratio of $SrCl_2/SrTiO_3 = 0.01$ (Fig. 3-3(b)). The peak disappeared almost completely for $SrCl_2/SrTiO_3 = 0.1$ (Figure 3-3(c)). Interestingly, new peaks appeared at 20,000 and 2500 cm^{-1} with a cut-off at around 2000 cm^{-1}. The peak at 11,000 cm^{-1} appeared to split into two bands at 20,000 and 2500 cm^{-1}. Upon further increase of the $SrCl_2/SrTiO_3$ ratio to 1 (Figure 3-3(d)), the intensities at 20,000 and 2500 cm^{-1} increased further. As discussed in section 2.3.1, the shape of the $SrTiO_3$ particles was greatly changed from irregular to fine-cubic shapes by increasing the $SrCl_2/SrTiO_3$ ratio up to 1. The particle agglomerates broke up, and fine cubic crystals were formed. The Al concentration increased upon the flux treatment; however, the concentration of doped Al remained constant at 0.2% at the $SrCl_2/SrTiO_3$ ratios between 0.01 and 1. Thus, the abrupt change in the transient spectra between $SrCl_2/SrTiO_3 = 0.01$ and 1 is presumably associated with the morphological change of the STO($SrCl_2$) particles.

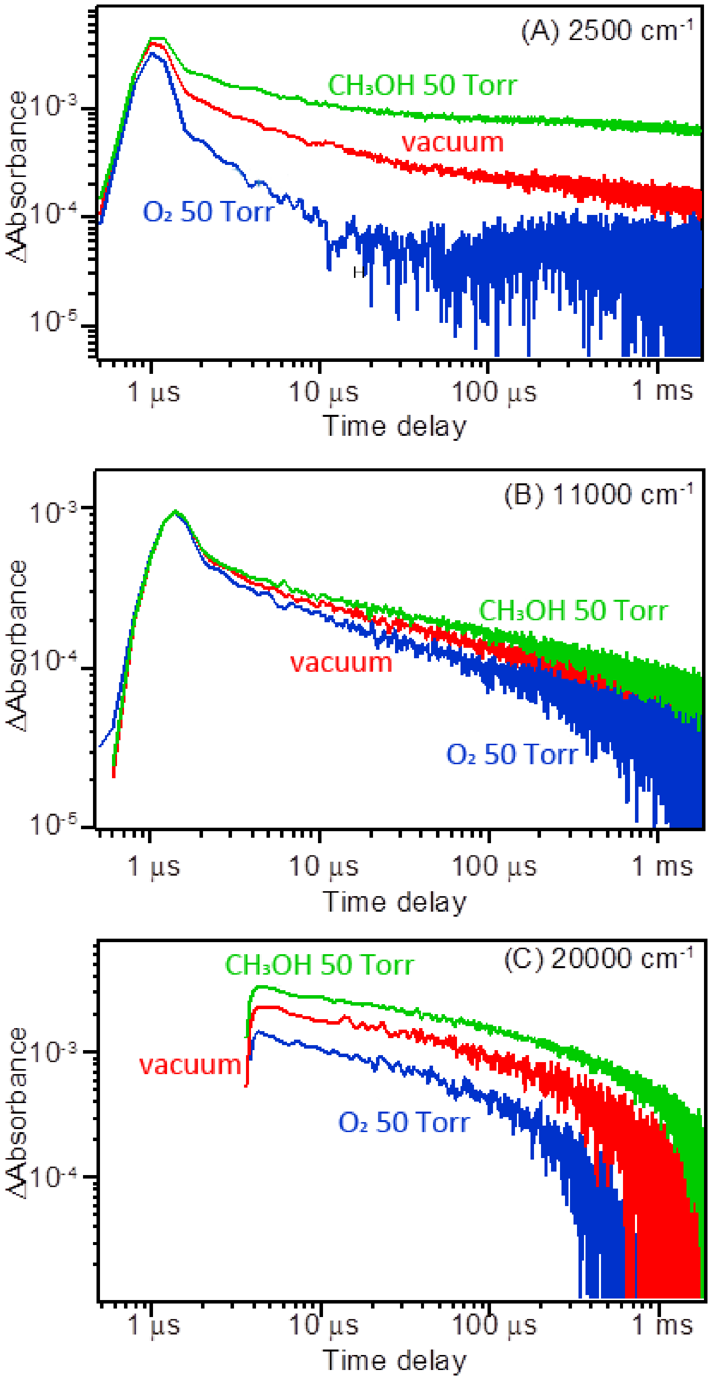

Figure 3-6. Decay curves of transient absorption of STO($SrCl_2$) treated with $SrCl_2/SrTiO_3 = 1$ irradiated by 355 nm laser pulses (0.5 mJ per pulse at 0.2 Hz). The decay curves were measured at 2500 cm^{-1} (A), 11000 cm^{-1} (B), and 20000 cm^{-1} (C) in vacuum, 50 Torr O_2, and CH_3OH.

The cause of the transient absorption is investigated by observing the intensity change in the presence and absence of electron- and hole-consuming reagents. Figure 3-6 shows the decay curves for the transient absorption at 2500, 11,000, and 20,000 cm^{-1} on $SrCl_2/SrTiO_3$ = 1. The absorption band at 2500 cm^{-1} was ascribed to shallowly trapped electrons, because it decreased and increased upon exposure to O_2 and MeOH, respectively. The depth of the electron trap is estimated to be 0.24 eV from the low-frequency cut-off wavenumber located at around 2000 cm^{-1} (0.24 eV), which is shallower than that estimated from the position of the peak located at 2500 cm^{-1} (0.31 eV). As for the absorption at 11,000 and 20,000 cm^{-1}, the intensity also increased and decreased upon exposure to O_2 and MeOH, respectively. These results suggest that the absorption at 11,000 and 20,000 cm^{-1} mainly reflects the number of trapped electrons. It should be noted that these charge carriers are trapped in the defects, but they still show reactivity toward the reactant molecules.

3.3.3. Behavior of Photogenerated Charge Carriers on Al-doped $SrTiO_3$ Particles

Further increase of the $SrCl_2/SrTiO_3$ ratio to 10 induced a dramatic change in the shape of the transient absorption spectra (Figure 3-2(e)): the band intensities at 20,000 and 2500 cm^{-1} increased further. However, the peak at 11,000 cm^{-1}, which was present in the as-purchased sample (Figure 3-2(a)) but had disappeared upon the flux treatments ($SrCl_2/SrTiO_3$ = 0.1 and = 1, Figure 3-2(c) and (d)), reappeared. SEM and XRD analyses revealed that there was no large difference in the particle morphology and crystallinity of the $SrTiO_3$ samples treated at the $SrCl_2/SrTiO_3$ molar ratios of 1 and 10. Therefore, the reappearance of the 11,000 cm^{-1} peak could not be due to a change in the morphology of the crystal. As shown in Table 2-3, the concentration of doped Al increased to 0.31% when the ratio of flux increased to $SrCl_2/SrTiO_3$ = 10. Thus, the appearance of the 11,000 cm^{-1} band is presumably associated with the Al doping.

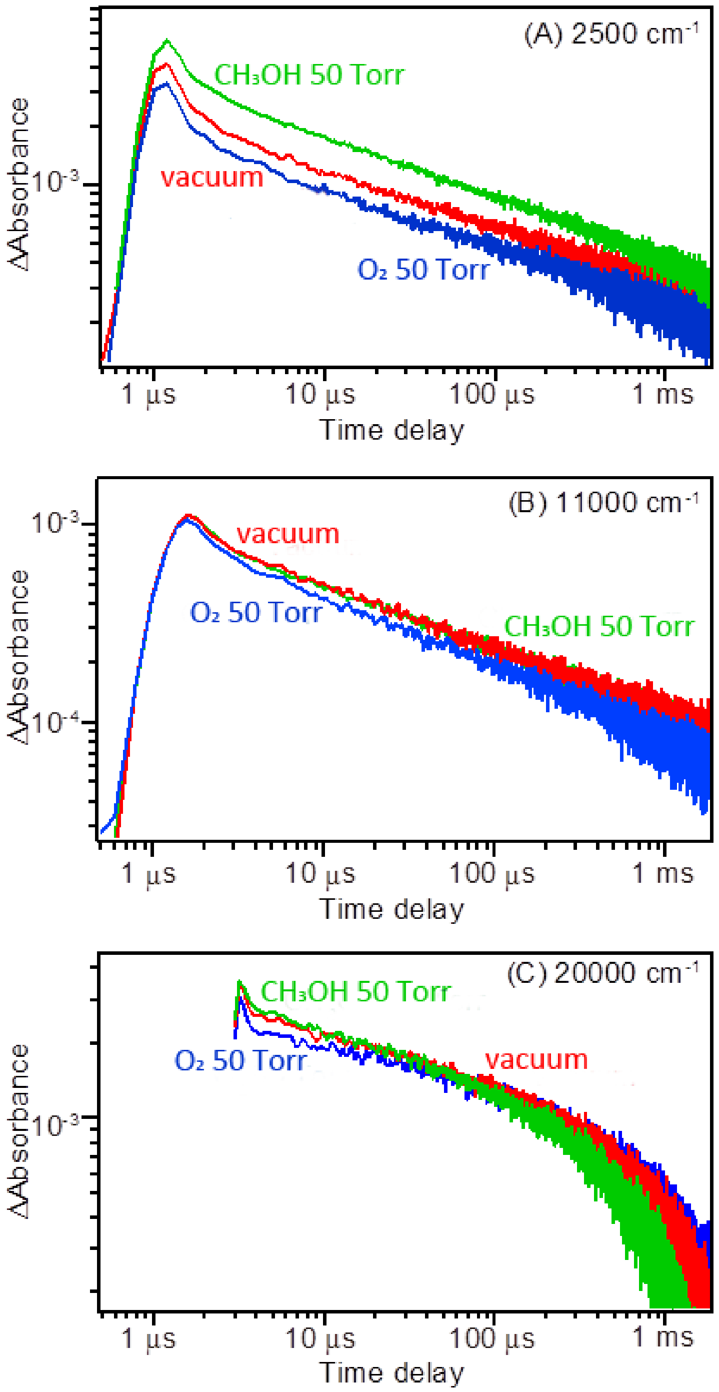

Figure 3-7. Decay curves of transient absorption of STO($SrCl_2$) treated with $SrCl_2/SrTiO_3$ = 10 irradiated by 355 nm laser pulses (0.5 mJ per pulse at 0.2 Hz). The decay curves were measured at 2500 cm^{-1} (A), 11000 cm^{-1} (B), and 20000 cm^{-1} (C) in vacuum, 50 Torr O_2, and CH_3OH.

The decay processes for the transient absorption at 20,000, 11,000, and 2500 cm^{-1} are further investigated in the presence and absence of reactant gases (Figure 3-7). The decay of the absorption at 2500 cm^{-1} was slightly accelerated and decelerated upon exposure to O_2 and MeOH, respectively. However, the change was not as large as in the cases of STO(wako) and STO($SrCl_2$/STO = 1). On the other hand, the band intensities at 20,000 and 11,000 cm^{-1} were changed little by exposure to O_2 or MeOH, presumably due to weakre adsorption amounts of these molecules on the surface. It is reported that O_2 [31] and MeOH [32,33] prefer to adsorb on surface defects. Therefore, it is expected that adsorption occurs only a little on the fine crystal surfaces: it is widely believed that surface defects of $SrTiO_3$ work as reaction centers for chemical adsorption of O_2 or MeOH. [31–33]

The decay curves for the shallowly trapped electrons on STO(wako), STO($SrCl_2$/STO = 1), and STO($SrCl_2$/STO = 10) are plotted in Figure 3-8(a). It is clearly seen that the lifetime of electrons observed at 2500 cm^{-1} was prolonged by the treatments with larger amounts of $SrCl_2$ flux. This trend is well correlated with the steady-state photocatalytic activity, as shown in Table 2-2. In contrast, the decay curves for the deeply trapped electrons and holes, which exhibited transient absorption peaks at 20,000 and 11,000 cm^{-1}, were much more complex (Figure 3-8(b) and (c)). There was no correlation with the steady-state photocatalytic activity, indicating that the deeply trapped carriers were less reactive with water. As discussed in the previous sections, both electrons and holes can show a transient absorption in the visible to NIR region. Therefore, it is very difficult to distinguish the contribution from electrons and holes. However, it should be noted here that the transient absorption in the visible to NIR region is absent in defect-free single-crystalline $SrTiO_3$ [11] and is very sensitive to the structure of defects and impurities. This study demonstrates that the spectral shape changes dramatically upon flux treatment. I believe that a detailed analysis of the transient absorption in the visible to mid-IR region would enable a fuller understanding of photogenerated charge carriers associated with defects. It is difficult to remove defects and impurities from powder particles; therefore, a thorough understanding of the behavior of photogenerated charge carriers at defects and impurities is essential for the development of highly active photocatalysts.

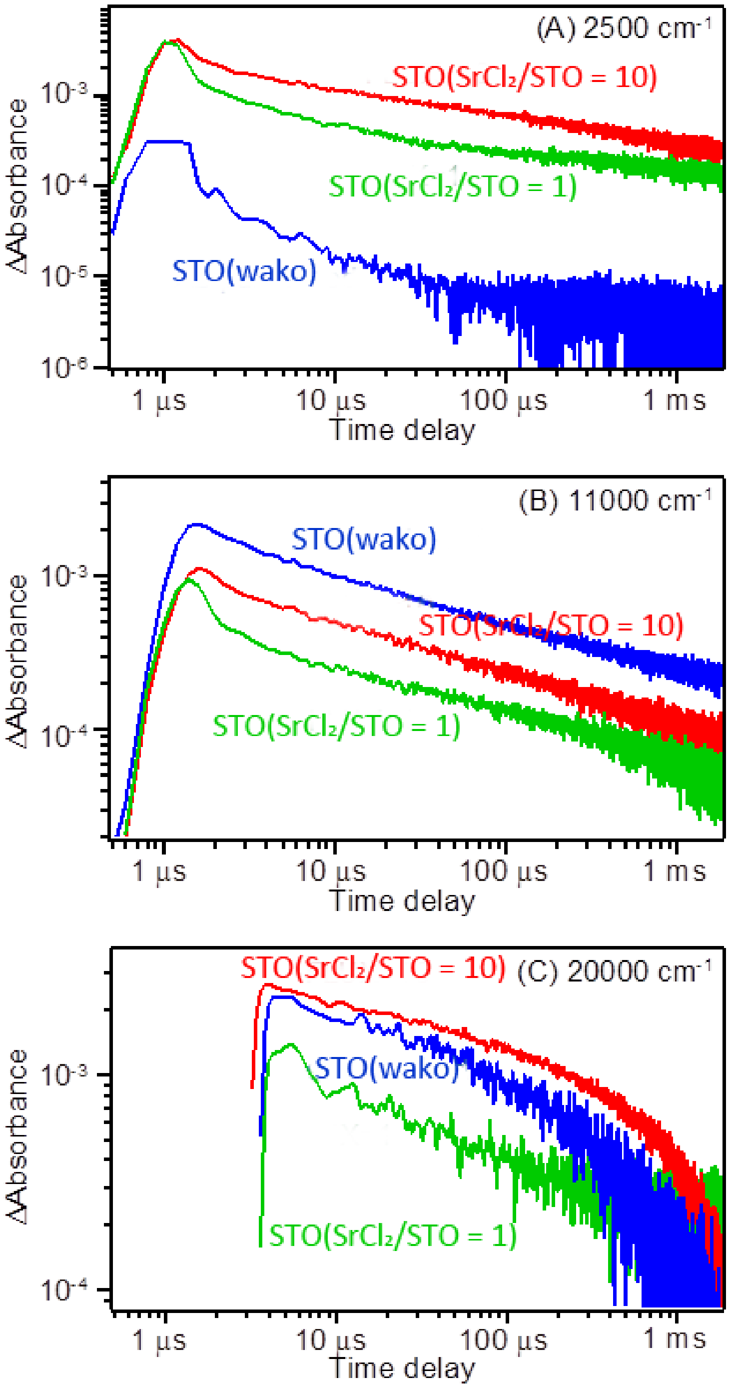

Figure 3-8. Flux dependent decay curves of transient absorption of different $SrTiO_3$ irradiated by 355 nm laser pulses (0.5 mJ per pulse at 0.2 Hz). The decay curves were measured at 2500 cm^{-1} (A), 11000 cm^{-1} (B), and 20000 cm^{-1} (C) in vacuum, 50 Torr O_2, and CH_3OH.

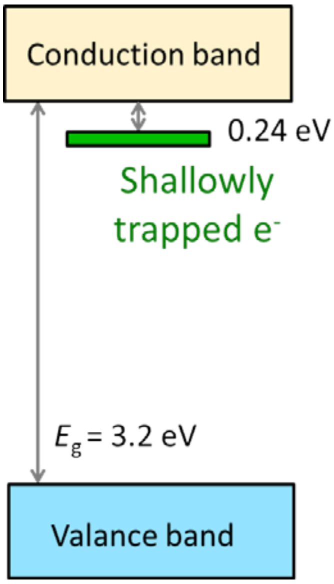

Figure 3-9. Schematic illustration of assigned shallowly trap state.

3.4. Conclusions

In this chapter, time-resolved visible to mid-IR absorption spectroscopy was performed to investigate the effects of flux treatment on the behavior of photogenerated charge carriers in $SrTiO_3$ particles. In the case of the STO(wako), most of the charge carriers generated by bandgap excitation were deeply trapped at defects. The depth of the trapped states depended on the defect structure. When STO(wako) was treated with $SrCl_2$ flux, the number of defects was much reduced and fine cubic crystals were formed. In the flux-treated sample, the number of deeply trapped charge carriers was reduced while that of shallowly trapped electrons was increased. It was also found that the flux treatment in an Al_2O_3 crucible induced Al doping into $SrTiO_3$ and led to further changes in the transient absorption spectra: a new peak appeared and the lifetime of shallowly trapped electrons was prolonged.

References

[1] K. Domen, S. Naito, M. Soma, T. Onishi, and K. Tamaru, “Photocatalytic decomposition of water vapour on an NiO–$SrTiO_3$ catalyst,” *Journal of the Chemical Society, Chemical Communications*, no. 12, pp. 543–544, 1980.

[2] A. Kudo and Y. Miseki, “Heterogeneous photocatalyst materials for water splitting,” *Chemical Society Reviews*, vol. 38, no. 1, pp. 253–278, 2009.

[3] H. Kato and A. Kudo, “Visible-light-response and photocatalytic activities of TiO_2 and $SrTiO_3$ photocatalysts codoped with antimony and chromium,” *The Journal of Physical Chemistry B*, vol. 106, no. 19, pp. 5029–5034, 2002.

[4] K. Furuhashi, Q. Jia, A. Kudo, and H. Onishi, “Time-resolved infrared absorption study of $SrTiO_3$ photocatalysts codoped with rhodium and antimony,” *The Journal of Physical Chemistry C*, vol. 117, no. 37, pp. 19 101–19 106, 2013.

[5] Y. Miseki, K. Saito, and A. Kudo, “Nanocrystalline $CaZrTi_2O_7$ photocatalyst prepared by a polymerizable complex method in the presence of Cs_2CO_3 flux for water splitting,” *Chemistry Letters*, vol. 38, no. 2, pp. 180–181, 2009.

[6] T. Takata, D. Lu, and K. Domen, “Synthesis of structurally defined Ta_3N_5 particles by flux-assisted nitridation,” *Crystal Growth & Design*, vol. 11, no. 1, pp. 33–38, 2011.

[7] S. S. K. Ma, T. Hisatomi, K. Maeda, Y. Moriya, and K. Domen, “Enhanced water oxidation on Ta_3N_5 photocatalysts by modification with alkaline metal salts,” *Journal of the American Chemical Society*, vol. 134, no. 49, pp. 19 993–19 996, 2012.

[8] F. Zhang, A. Yamakata, K. Maeda, Y. Moriya, T. Takata, J. Kubota, K. Teshima, S. Oishi, and K. Domen, “Cobalt-modified porous single-crystalline $LaTiO_2N$ for highly efficient water oxidation under visible light,” *Journal of the American Chemical Society*, vol. 134, no. 20, pp. 8348–8351, 2012.

[9] H. Kato, M. Kobayashi, M. Hara, and M. Kakihana, “Fabrication of $SrTiO_3$ exposing characteristic facets using molten salt flux and improvement of photocatalytic activity for water splitting,” *Catalysis Science & Technology*, vol. 3, no. 7, pp. 1733–1738, 2013.

[10] A. Yamakata, M. Kawaguchi, N. Nishimura, T. Minegishi, J. Kubota, and K. Domen, “Behavior and energy states of Photogenerated charge carriers on Pt- or CoO_x-loaded $LaTiO_2N$ photocatalysts: Time-resolved visible to mid-infrared absorption study,” *The Journal of Physical Chemistry C*, vol. 118, no. 41, pp. 23 897–23 906, 2014.

[11] A. Yamakata, J. J. M. Vequizo, and M. Kawaguchi, “Behavior and energy state of photogenerated charge carriers in single-crystalline and polycrystalline powder $SrTiO_3$ studied by time-resolved absorption spectroscopy in the visible to mid-infrared region,” *The Journal of Physical Chemistry C*, vol. 119, no. 4, pp. 1880–1885, 2015.

[12] A. Yamakata, T. Ishibashi, and H. Onishi, “Time-resolved infrared absorption spectroscopy of photogenerated electrons in platinized TiO_2 particles,” *Chemical Physics Letters*, vol. 333, no. 3, pp. 271–277, 2001.

[13] A. Yamakata, T. Ishibashi, and H. Onishi, “Water-and oxygen-induced decay kinetics of Photogenerated electrons in TiO_2 and Pt/TiO_2: a time-resolved infrared absorption study,” *The Journal of Physical Chemistry B*, vol. 105, no. 30, pp. 7258–7262, 2001.

[14] A. Yamakata, T. Ishibashi, H. Kato, A. Kudo, and H. Onishi, “Photodynamics of $NaTaO_3$ catalysts for efficient water splitting,” *The Journal of Physical Chemistry B*, vol. 107, no. 51, pp. 14 383–14 387, 2003.

[15] A. Yamakata, M. Yoshida, J. Kubota, M. Osawa, and K. Domen, “Potential-dependent recombination kinetics of photogenerated electrons in n-and p-type GaN photoelectrodes studied by time-resolved IR absorption spectroscopy,” *Journal of the American Chemical Society*, vol. 133, no. 29, pp. 11 351–11 357, 2011.

[16] A. Yamakata, T. Ishibashi, and H. Onishi, “Electron-and hole-capture reactions on Pt/TiO_2 photocatalyst exposed to methanol vapor studied with time-resolved infrared absorption spectroscopy,” *The Journal of Physical Chemistry B*, vol. 106, no. 35, pp. 9122–9125, 2002.

[17] A. Yamakata, T. Ishibashi, and H. Onishi, “Effects of water addition on the methanol oxidation on Pt/TiO_2 photocatalyst studied by time-resolved infrared absorption spectroscopy,” *The Journal of Physical Chemistry B*, vol. 107, no. 36, pp. 9820–9823, 2003.

[18] A. Yamakata, T. Ishibashi, and H. Onishi, “Microsecond kinetics of photocatalytic oxidation on Pt/TiO_2 traced by vibrational spectroscopy,” *Chemical physics letters*, vol. 376, no. 5, pp. 576–580, 2003.

[19] A. Yamakata, I. Takaaki, and H. Onishi, “Effects of accumulated electrons on the decay kinetics of Photogenerated electrons in Pt/TiO_2 photocatalyst studied by time-resolved infrared absorption spectroscopy,” *Journal of Photochemistry and Photobiology A: Chemistry*, vol. 160, no. 1, pp. 33–36, 2003.

[20] T. Chen, Z. Feng, G. Wu, J. Shi, G. Ma, P. Ying, and C. Li, “Mechanistic studies of photocatalytic reaction of methanol for hydrogen production on Pt/TiO_2 by in situ fourier transform IR and time-resolved IR spectroscopy,” *The Journal of Physical Chemistry C*, vol. 111, no. 22, pp. 8005–8014, 2007.

[21] B. H. Meekins and P. V. Kamat, “Role of water oxidation catalyst IrO_2 in shuttling photogenerated holes across TiO_2 interface,” *The Journal of Physical Chemistry Letters*, vol. 2, no. 18, pp. 2304–2310, 2011.

[22] D. Bahnemann, A. Henglein, J. Lilie, and L. Spanhel, “Flash photolysis observation of the absorption spectra of trapped positive holes and electrons in colloidal titanium dioxide,” *The Journal of Physical Chemistry*, vol. 88, no. 4, pp. 709–711, 1984.

[23] D. W. Bahnemann, M. Hilgendorff, and R. Memming, “Charge carrier dynamics at TiO_2 particles: reactivity of free and trapped holes,” *The Journal of Physical Chemistry B*, vol. 101, no. 21, pp. 4265–4275, 1997.

[24] T. Yoshihara, R. Katoh, A. Furube, Y. Tamaki, M. Murai, K. Hara, S. Murata, H. Arakawa, and M. Tachiya, “Identification of reactive species in photoexcited nanocrystalline TiO_2 films by wide-

wavelength-range (400-2500 nm) transient absorption spectroscopy," *The Journal of Physical Chemistry B*, vol. 108, no. 12, pp. 3817–3823, 2004.

[25] Y. Tamaki, A. Furube, M. Murai, K. Hara, R. Katoh, and M. Tachiya, "Direct observation of reactive trapped holes in TiO_2 undergoing photocatalytic oxidation of adsorbed alcohols: evaluation of the reaction rates and yields," *Journal of the American Chemical Society*, vol. 128, no. 2, pp. 416–417, 2006.

[26] M. Barroso, A. J. Cowan, S. R. Pendlebury, M. Grätzel, D. R. Klug, and J. R. Durrant, "The role of cobalt phosphate in enhancing the photocatalytic activity of α-Fe_2O_3 toward water oxidation," *Journal of the American Chemical Society*, vol. 133, no. 38, pp. 14 868–14 871, 2011.

[27] M. Barroso, C. A. Mesa, S. R. Pendlebury, A. J. Cowan, T. Hisatomi, K. Sivula, M. Grätzel, D. R. Klug, and J. R. Durrant, "Dynamics of photogenerated holes in surface modified α-Fe_2O_3 photoanodes for solar water splitting," *Proceedings of the National Academy of Sciences*, vol. 109, no. 39, pp. 15 640–15 645, 2012.

[28] A. Yamakata, E. Soeta, T. Ishiyama, M. Osawa, and A. Morita, "Real-time observation of the destruction of hydration shells under electrochemical force," *Journal of the American Chemical Society*, vol. 135, no. 40, pp. 15 033–15 039, 2013.

[29] K. Maeda, K. Teramura, H. Masuda, T. Takata, N. Saito, Y. Inoue, and K. Domen, "Efficient overall water splitting under visible-light irradiation on $(Ga_{1-x}Zn_x)(N_{1-x}O_x)$ dispersed with Rh-Cr mixed-oxide nanoparticles: Effect of reaction conditions on photocatalytic activity," *The Journal of Physical Chemistry B*, vol. 110, no. 26, pp. 13 107–13 112, 2006.

[30] T. Takata and K. Domen, "Defect engineering of photocatalysts by doping of aliovalent metal cations for efficient water splitting," *The Journal of Physical Chemistry C*, vol. 113, no. 45, pp. 19 386–19 388, 2009.

[31] H. Tanaka, T. Matsumoto, T. Kawai, and S. Kawai, "Interaction of oxygen vacancies with O_2 on a reduced $SrTiO_3(100)\sqrt{5}\times\sqrt{5}$-R26.6 ° surface observed by STM," *Surface science*, vol. 318, no. 1, pp. 29–38, 1994.

[32] T. Yoshikawa and M. Bowker, “Reductive coupling desorption of methanol on reduced $SrTiO_3$(110),” *Phys. Chem. Chem. Phys.*, vol. 1, no. 5, pp. 913–920, 1999.

[33] L.-Q. Wang, K. F. Ferris, S. Azad, and M. H. Engelhard, “Adsorption and reaction of methanol on stoichiometric and defective $SrTiO_3$(110) surfaces,” *The Journal of Physical Chemistry B*, vol. 109, no. 10, pp. 4507–4513, 2005.

Chapter 4: Photoelectrochemical Water Splitting on Particulate $SrTiO_3$ Electrodes

4.1. Introduction

Photoelectrochemical (PEC) water splitting is one of the promising environmentally-friendly methods for directly converting solar energy into chemical energy stored in the bonds of hydrogen and oxygen [1,2]. In terms of implementing practical applications based on these technologies, the scalability of solar hydrogen production systems is critical. One of the advantages of PEC water splitting is its flexibility regarding the morphology of the photoelectrodes, which can be porous, nanostructured, or particulate-based, due to the use of solid-liquid interfaces [3]. Single-crystal and epitaxial thin-film materials have been frequently employed as photoelectrode materials to achieve efficient water splitting. However, such electrodes are expensive, which makes them unsatisfactory for use in large-scale applications.

The fabrication of electrodes from photocatalytic particles has been studied as a promising method to prepare scalable photoelectrodes [4-8]. The advantages of this method are its simplicity in terms of preparation and the scalability of the powder synthesis. However, the low crystallinity of the particles as well as poor conductivity between the particles and the substrate thus have limited the performance of these photoelectrodes.

If photoelectrodes with a desirable structure, no grain boundaries between a solid-liquid interface and a backside contact, could be fabricated from photocatalytic particles, a higher efficiency and deeper understanding of the photocatalytic materials could be obtained. To this end, the particle transfer (PT) method has been developed recently as a means to fabricate electrodes from photocatalytic particles [9]. The PT method can be used to produce a mechanically strong and high-quality electrical contact between a semiconductor and a substrate making it one of the most promising methods to obtain highly efficient photoelectrodes from photocatalytic particles. There has been some reports of photoelectrodes prepared by PT method using particulate (oxy)nitrides and (oxy) chalcogenides such as $LaTiO_2N$ [9], $BaTaO_2N$ [10], Ta_3N_5 [11], Cu-Ga-Se [12], and $La_5Ti_2(Cu, Ag)S_5O_7$ [13]. These photoelectrodes show relatively high photocurrent at around 1.23 V_{RHE} for photoanodes and at around 0 V_{RHE} for photocathodes because of the preferable structure of photoelectrode fabricated by PT method. However, their onset potential of photocurrent are not sufficient because, considering the construction of overall water splitting system, onset potentials of photoanode and photocathode need to be overlapped each other significantly. The possible reasons of the limited PEC performance of the photoelectrodes prepared by PT method are the crystallinities, surface properties, and structural feature of photocatalytic particles used in the photoelectrodes.

In this chapter, PEC properties of photoanode prepared through PT method using particulate $SrTiO_3$ developed in Chapter 2 are discussed. A study about the contact layer material revealed that the backside contact have significant influence on the value and significant onset of photocurrent; formation of Schottky barrier clearly hinder both onset potential and photocurrent especially at relatively low applied potential. The $SrTiO_3$ photoanode fabricated by PT method using proper contact layer and high quality of particles showed comparable photocurrent to that of single crystalline wafer of Nb doped $SrTiO_3$. I believe this is the first report of the electrode prepared from semiconductor powders having a high activity as electrode fabricated from single crystalline wafer of the same material.

4.2. Experimental Section

4.2.1. Synthesis of $SrTiO_3$ Powders

A pristine $SrTiO_3$(STO(wako)), a 1% Al doped $SrTiO_3$ synthesized by solid state reaction (Al-STO(ssr)), a $SrTiO_3$ synthesized by flux method using $SrCl_2$ in yttria crucible (STO(flux)), and a 1% Al doped $SrTiO_3$ synthesized by flux method using $SrCl_2$ in yttria crucible (Al-STO(flux)) were prepared as described in section 2.2 and they were used for photoelectrode fabrication through PT method.

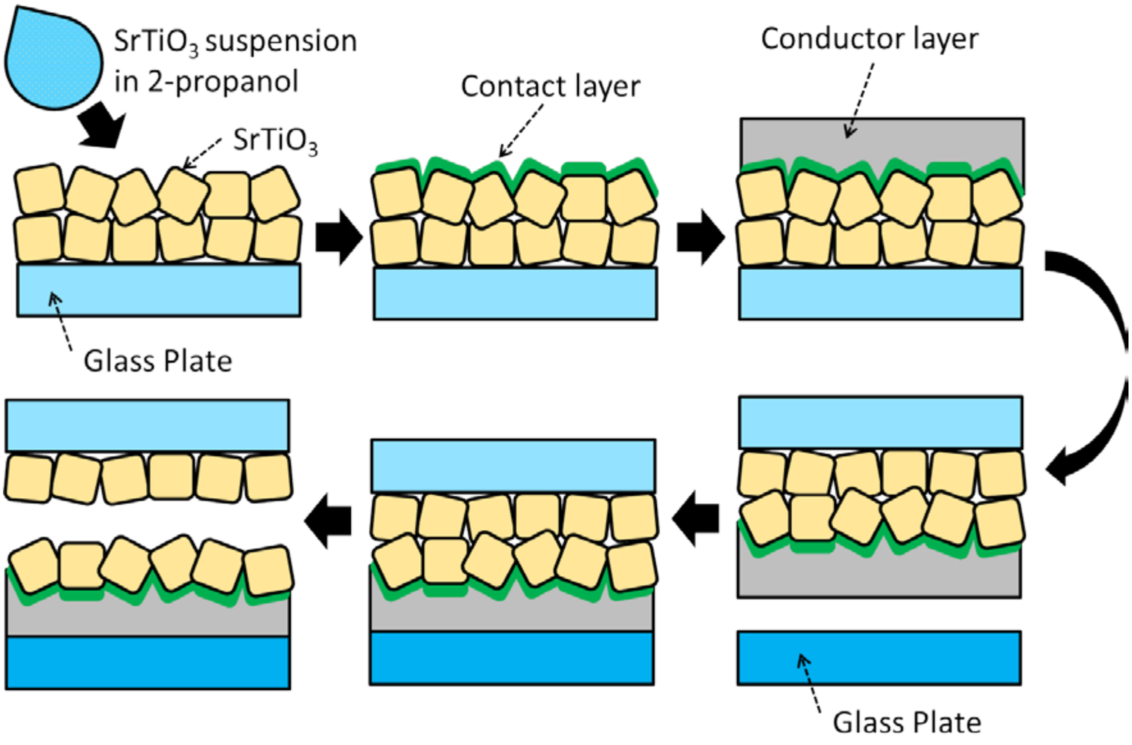

Figure 4-1. Schematic of the particle transfer method.

4.2.2. Fabrication of $SrTiO_3$ Electrodes by Particle Transfer Method.

The particle transfer (PT) method is illustrated in Figure 4-1. A suspension of $SrTiO_3$ powder was prepared by dispersing 100 mg of $SrTiO_3$ powder in 1 ml of isopropanol by sonication and stirring. The photocatalytic particles were coated on a 30×10 mm sized glass plate using the prepared suspension through a drop casting followed by drying. The contact and conductor layers were deposited either by vacuum evaporation method or radio-frequency magnetron sputtering method. For the radio-frequency magnetron sputtering method, powder coated glass plates were placed in a vacuum chamber with a base pressure of $< 10^{-3}$ Pa. The contact layer was deposited with RF power of 50 W, an Ar pressure of 0.1 Pa and a sample temperature of 373 or 573 K. The deposition time was 10 min for Ta, Ti, Mo and 50 min for Ni. To obtain sufficient conductivity and mechanical strength, a thicker conductor layer was formed using radio-frequency magnetron sputtering on top of the contact layer. The thickness of contact, and conductor layers were estimated to be 100~ 300 nm for contact, and ~5 μm for conductor layers, respectively. The layers were bonded to another glass plate by adhesives, such as epoxy resin or double-sided tapes, and then peeled off from the original glass plate. The excess particles on the electrode which are not contact with contact layer directly were removed by ultra-sonication in water. Electrodes prepared from each type of $SrTiO_3$ will hereafter be referred to as STO(wako)/M, STO(flux)/M, Al-STO(flux)/M, and Al-STO(ssr)/M, respectively, where M represents the type of metal used as a contact layer.

4.2.3. Fabrication of Electrodes from Single Crystalline $SrTiO_3$ Wafer.

Single crystalline wafer of Nb doped $SrTiO_3$ (Shinkosha Co. LTD., Nb 0.01wt%, 10 x 10 x 0.5 t mm, polished on one side, (100)) was purchased and used without any pretreatment. The surface was cleansed in acetone, followed by ethanol and distilled water. The contact layer was deposited on unpolished side of the crystal. The electrodes prepared this way will hereafter be referred to as STO:Nb(SC)/M where M represents the type of metal used as a contact layer.

4.3. Results and Discussion

4.3.1. Characterization of $SrTiO_3$ Electrodes Prepared by Particle Transfer Method

The structure of $SrTiO_3$ photoelectrode prepared by PT method was observed with SEM. Figure 4-2 shows SEM images of a photoelectrode prepared from Al-STO(flux) particles with Ta contact layer. Top-view SEM images of the photoelectrode is shown in Figure 4-2(a). The electrode was similar in structure to a $LaTiO_2N$ electrode prepared via the PT method that we reported previously.[9] The SEM images show that the surface of the electrode was densely covered with Al-STO(flux) particles, albeit with a few voids,

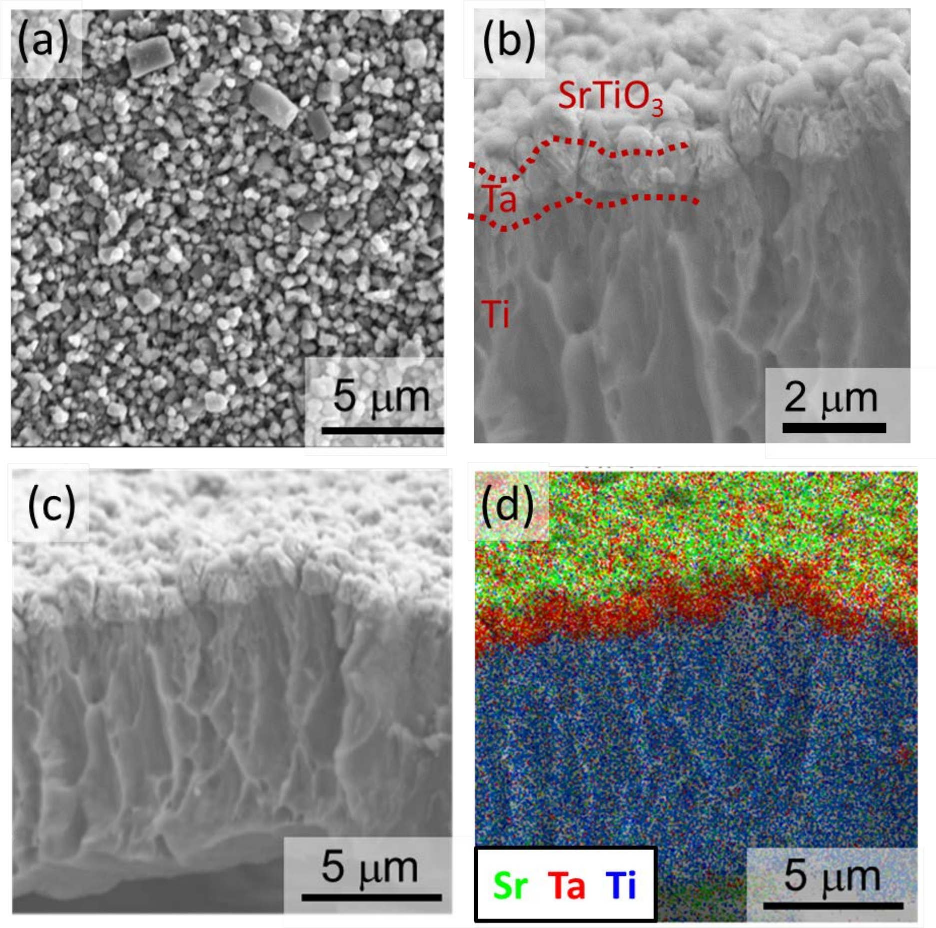

Figure 4-2. SEM images of Al-STO(flux)/Ta. (a) Top down view, (b, c) cross section, and (d) EDS mapping of the cross section.

as shown in Figure 4-3. The cross-sectional SEM images shown in Figures 4-2(b,c) and the simultaneously measured EDS map shown in Figure 4-2(d) reveal that the Al-STO(flux) particles were firmly anchored by the contact layer with quite a few excess particles on the electrode surface, and that the Ta contact layer was distributed between the Al-STO(flux) particles and the Ti conductor layer. Excess particles on the electrode can absorb light and decrease the number of useful photons for PEC reactions. Based on the SEM results, it is reasonable to conclude that the $SrTiO_3$ electrodes prepared using PT method have structural features suitable for applications to PEC water splitting.

Structural feature of photoelectrodes fabricated from STO(wako), Al-STO(ssr), and STO(flux) under the same condition as the case of were also characterized by using SEM as presented in Figure 4-4. The surface of the electrodes prepared from STO(wako) was covered by few micron sized aggregates and sub-micron sized particles with indeterminate form. The electrodes prepared from Al-STO(ssr) has similar structural features with STO(wako)/Ti as shown in Figure 4-4(b). The primary particles of Al-STO(ssr) were a few hundred nanometers in size and they were agglomerated into secondary particles. The size distribution of the STO(flux) particles is roughly 0.2-2 μm which is much broader compared to other samples examined in this study. The piles of smaller particles of about a few hundred nanometers were easily observed around few micron meter sized particles as shown in Figure 4-4(c). The particles of Al-STO(flux) were separated from each other due to the flux treatment, and the size distribution was narrower which was roughly 0.2-1 μm. A few exceptionally large particles of about 2 μm was seldom observe, while piling up of the smaller particles was not observed unlike the electrodes prepared from STO(flux).

4.3.2. Photoelectrochemcical Properties of $SrTiO_3$ Electrodes

In the electrode preparation by PT method, the choice of the contact layer material is essential to obtain photoelectrode with large photocurrent because of the significant influence of schottky barrier formation. *I-E* curves of Al-STO(flux)/M photoanodes prepared with contact layer metals of Ta, Ti, Au, or Ni, were shown in Figure 4-5. The photoanode fabricated with Ta contact layer, Al-STO(flux)/Ta, exhibited the largest photocurrent at whole applied potential. To declare the reason of different from *I-E* curves Al-STO(flux)/M photoelectrodes, metal-semiconductor contact are discussed based on the difference of work functions. The work functions of the metals used for the contact layer are listed in Table 4-1. For Al-STO(flux)/Ta and Al-STO(flux)/Ti, high current densities of 6.7 and 5.0 mA cm^{-2} at 1.23 V_{RHE} were observed, while Al-STO(flux)/Ni and Al-STO(flux)/Au exhibited clearly lower current densities of 2.1 mA cm^{-2} and 1.4 mA cm^{-2} at the same potential. These results can be well explained by the difference in the

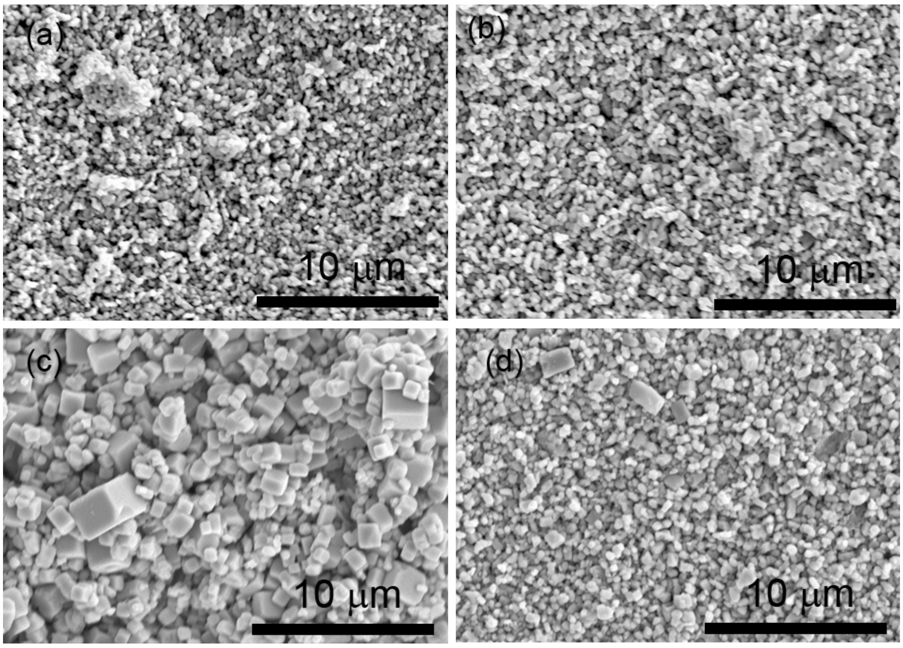

Figure 4-4. Top-view SEM images of (a) STO(wako)/Ti, (b) Al-STO/Ti, (c) STO(flux)/Ti, and (c) Al-STO(flux)/Ti electrodes.

band diagram at the metal-semiconductor contact due to the difference in work functions of the metals [14] as illustrated in Figure 4-5.

The work function of $SrTiO_3$ is reported to be about 4.2 eV [15], and its bandgap is reported to be about 3.2 eV [16]. When it forms a junction with a metal such as Au and Ni, which have significantly larger work functions than that of $SrTiO_3$, an obvious Schottky barrier should be formed at the metal-semiconductor interface. This Schottky barrier exhibits rectification behavior, which prevents electron transfer from the $SrTiO_3$ to the metal. In contrast, the difference between the work functions of Ta and Ti and that of $SrTiO_3$ is negligible. Therefore, the Schottky barrier formed at the interfaces is negligible and an ohmic-like contact that provides efficient electron transfer from $SrTiO_3$.

Table 1. Work function of metals examined as contact layer [14].

Metal	Work function / eV
Ta	4.25
Ti	4.33
Mo	4.60
Au	5.10
Ni	5.15

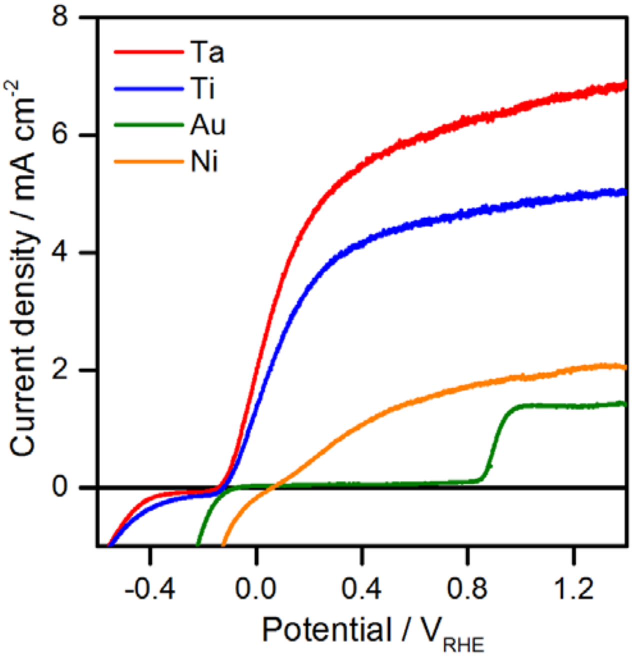

Figure 4-5. *I*-*E* curves for Al-STO(flux)/M with different metals as contact layer. 0.1 M Na_2SO_4 aqueous solution + NaOH (pH = 13) and 300 W Xe lamp equipped with cold mirror (λ >300 nm) were used as an electrolyte and light source.

Next, the effect of the contact layer material on the PEC properties was examined for electrodes produced from a single crystalline wafer of Nb-doped $SrTiO_3$. *I*-*E* curves measured for STO:Nb(SC)/M are shown in Figure 4-5. Although the onset potential was independent of the contact layer material, STO:Nb(SC)/Ta exhibited the highest photocurrent. Based on the *I*-*E* curves for the electrodes prepared from both particles and single crystalline wafers, it can be concluded that Ta produces the best electrical contact for $SrTiO_3$ electrodes owing to its small work function

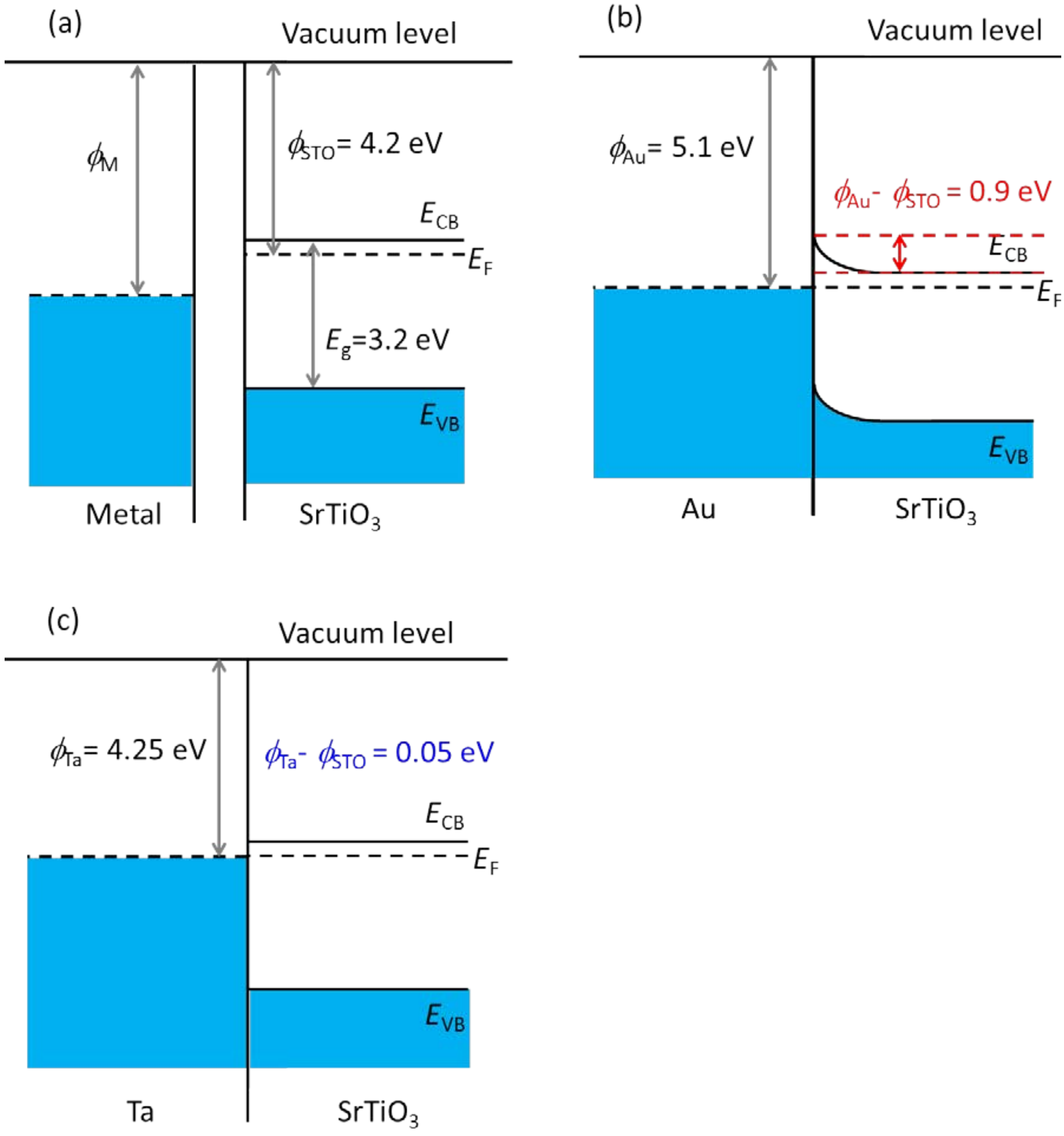

Figure 4-6. Schematic illustration of contact between semiconductor $SrTiO_3$ and metal contact layer (a) Before contact, (b) after contact with Au, and (c) after contact with Mo.

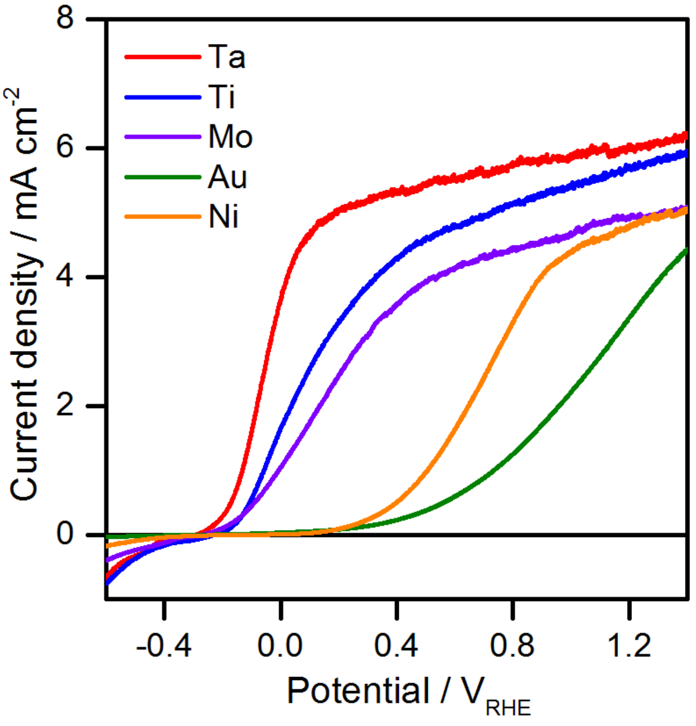

Figure 4-7. *I*-*E* curves for STO:Nb(SC)/M with different metals as contact layer. 0.1 M Na_2SO_4 aqueous solution + NaOH (pH = 13) and 300 W Xe lamp equipped with cold mirror (λ >300 nm) were used as an electrolyte and light source.

The PEC properties of electrodes prepared from different types of $SrTiO_3$ particles were investigated. *I*-*E* curves for the photoanodes prepared from STO(wako), Al-STO(ssr), STO(flux), and Al-STO(flux) are shown in Figure 4-8. The photoanodes prepared from STO(wako) showed poor reproducibility likely due to the fact that many agglomerated which are a few micrometer in size exists. It should be noted that the existence of particles with too large size results in formation of pinholes to the contact and conductor layers indicating contamination of the electrode surface by erupted adhesives through the pinholes. However, the chosen electrode showed quite high photocurrent of 7.6 mA cm^{-1} at 1.23 V$_{RHE}$. The structure of the electrodes prepared from Al-STO(ssr) powder was not much different from that of the electrodes prepared from STO(wako) as shown in Figure 4-4 and the chosen electrode showed 7.2 mA cm^{-1}, which was comparable to the highest current density observed for STO(wako). The primary particles of Al-STO(ssr) were a few hundred nanometers in size and they were agglomerated into secondary particles. The electrode prepared from STO(flux) powder showed the lowest current density of 3 mA cm^{-1} at 1.23 V_{RHE} among the examined samples. The electrodes prepared from Al-STO(flux) powder showed photocurrent of 7.6 mA cm^{-1} at 1.23 V_{RHE} which is one of the highest values along with STO(wako). Furthermore, reproducibility of Al-STO(flux) based electrode was outstanding because of relatively small size distribution of the particles.

As discussed above, the photocurrent for Al-STO based phtooanode was not saturated in the potential range studied, likely due to the series resistance caused by its high resistivity. STO(wako) showed the highest photocurrent among the samples investigated, while pristine STO showed the lowest photocatalytic activity for overall water splitting as discussed in Chapter 2. The difference between the PEC properties and the photocatalytic properties is likely due to the different mechanisms through which water splitting takes place on these electrodes. In the case of PEC water splitting, photo-excited carriers in the photocatalytic material are macroscopically separated by the band bending produced at the solid-liquid interfaces. In contrast, in the case of photocatalysis, all of the reactions take place directly on the photocatalytic particles. Thus, photocatalysis can be more sensitive to the surface conditions and does not always require electrical conductivity and band bending. The difference in charge separation is one of the possible reasons why a preferred synthesis method exists. It can be concluded that the unacceptably high Al-STO resistivity is a reflection of its high crystallinity based on its surface and bulk properties, and that the high crystallinity led to the higher photocatalytic activity.

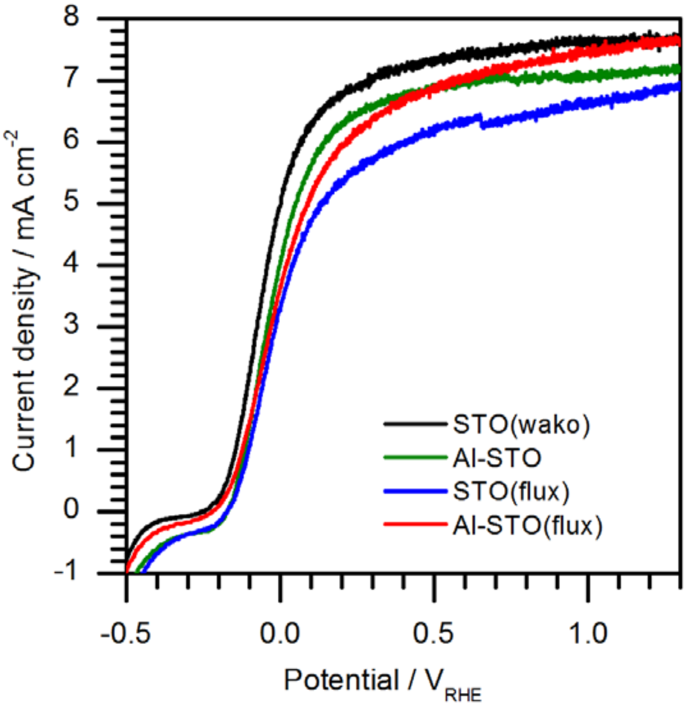

Figure 4-8. *I-E* curves for STO(wako)/Ti, Al-STO(ssr)/Ti, STO(flux)/Ti and Al-STO(flux)/Ti. 0.1 M Na_2SO_4 aqueous solution + NaOH (pH = 13) and 300 W Xe lamp equipped with cold mirror (λ >300 nm) were used as an electrolyte and light source.

4.3.3. Comparison between Electrodes Prepared from Particulate and Single Crystalline $SrTiO_3$

Figure 4-9 shows a comparison of the *I-E* curves and incident photon-to-current efficiency (IPCE) spectra measured for Al-STO/Ta(PT) and STO:Nb/Ta(SC). The onset potential for STO:Nb/Ta(SC) was about 0.1 V more negative than that for Al-STO/Ta(PT), while the photocurrent for Al-STO/Ta(PT) was even higher than that for STO:Nb/Ta(SC) at > 0 V_{RHE}. I believe that this is the first demonstration of electrodes prepared from semiconducting particles showing comparable performance to those prepared from the corresponding single-crystal material.

Some possible reasons for the higher photocurrent for Al-STO/Ta(PT) than for STO:Nb/Ta(SC) may be the following: The carrier concentration for Al-STO could have been lower than that for the conductive 0.01 wt.% Nb-doped STO. In the case of photoelectrodes prepared from sub-micron sized photocatalytic particles, carriers do not need to travel a long distance, and a material with a relatively high electrical resistivity can be used. It should be noted that higher resistivity can lead to a thicker depletion layer, which enhances the charge separation, and to an increase of the series resistance causing an IR drop in the electrode. Additionally, the smaller size of photocatalytic materials allows the depletion layer to occupy a larger fraction of photocatalytic particles in volume. Enhanced light absorption through the rough surface combined with reflections by the underlying metal layers is yet another possibility.

The IPCE spectra of Al-STO/Ta(PT) and STO:Nb/Ta(SC) under an applied potential of 1.23 V_{RHE} are shown in Figure 4-10. The relatively high IPCE of 18% exhibited by STO:Nb/Ta(SC) is consistent with the previously reported values of 15.67% on a 0.07 mol% Nb-doped single-crystal wafer of $SrTiO_3$ at 1.5 V vs. SCE [17] and of 25% at 290 nm on a thin-film Nb-doped $SrTiO_3$ photoanode [18]. Al-STO/Ta(PT) exhibited higher IPCEs than those of STO(SC) at all wavelengths studied, and the maximum value was 69% at 320 nm. These results show that photoanodes prepared from photocatalytic particles via the PT method are capable of comparable performance to those prepared from the single-crystal form of the same material. Moreover, such electrodes can exhibit a high IPCE due to their advantageous structural properties for light absorption and utilization of photo-excited carriers.

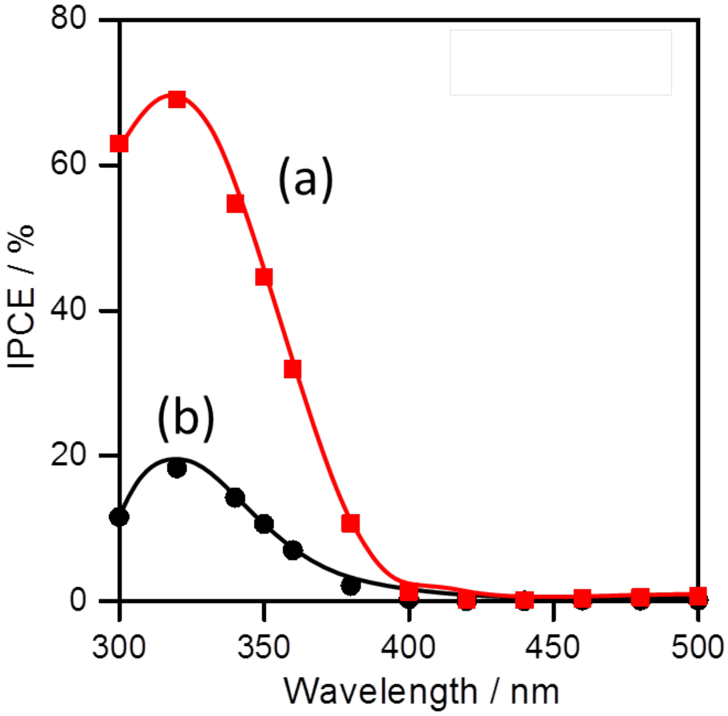

Figure 4-10. IPCE of (a) STO(PT)/Ta and (b) STO:Nb(SC)/Ta (left), with the light intensity (right). Measurement conditions: 3-electrode system with Ag/AgCl reference and Pt counter; Reaction solution, 0.1 M Na_2SO_4 aqueous solution + NaOH (pH = 13); Light source, 300 W Xe lamp (λ >200 nm).

4.4. Conclusions

A $SrTiO_3$ electrode with an extremely high IPCE was prepared from STO particles by the PT method. The photoanodes had desirable structural properties such as strong anchoring of the faceted and micron-sized $SrTiO_3$ particles onto the underlying metal layers. The resulting electrode structure exhibits efficient light absorption, smooth electron transfer from the particles to the back electrode, and enhanced charge separation. A systematic study of the contact layer material used for $SrTiO_3$ photoanodes prepared from both particles and single-crystal wafers revealed that Ta is the best material for forming ohmic contact, and the results are consistent with a general discussion on metal-semiconductor contacts based on the work function. The Al-STO/Ta(PT) photoanode exhibited a high IPCE of 69% at $V_{RHE} = 1.23$ V, which is higher than that for STO:Nb/Ta(SC) (18%). In fact, this IPCE is the highest among photoanodes prepared from similar materials. These results suggest that once photocatalytic materials with sufficient crystallinity and sensitivity to sunlight are developed, efficient solar hydrogen production from water using simple and scalable particle-based systems will become possible. Finally, the photocatalytic activity for overall water splitting of $SrTiO_3$ particles varied depending on the synthesis method used to produce the particles. These differences are likely due to the different mechanisms by which water splitting takes place on the electrode. I believe that although the crystallinity of Al-STO is sufficiently high, its resistivity is too large for application to photoanodes.

References

[1] N. S. Lewis, "Toward cost-effective solar energy use," *Science*, vol. 315, no. 5813, pp. 798–801, 2007.

[2] M. G. Walter, E. L. Warren, J. R. McKone, S. W. Boettcher, Q. Mi, E. A. Santori, and N. S. Lewis, "Solar water splitting cells," *Chemical Reviews*, vol. 110, no. 11, pp. 6446–6473, 2010.

[3] Z. Li, W. Luo, M. Zhang, J. Feng, and Z. Zou, "Photoelectrochemical cells for solar hydrogen production: current state of promising photoelectrodes, methods to improve their properties, and outlook," *Energy & Environmental Science*, vol. 6, no. 2, pp. 347–370, 2013.

[4] S.-Q. Fan, C.-J. Li, G.-J. Yang, L.-Z. Zhang, J.-C. Gao, and Y.-X. Xi, "Fabrication of nano-TiO_2 coating for dye-sensitized solar cell by vacuum cold spraying at room temperature," *Journal of Thermal Spray Technology*, vol. 16, no. 5-6, pp. 893–897, 2007.

[5] M. Yang, L. Li, S. Zhang, G. Li, and H. Zhao, "Preparation, characterisation and sensing application of inkjet–printed nanostructured TiO_2 photoanode," *Sensors and Actuators B: Chemical*, vol. 147, no. 2, pp. 622–628, 2010.

[6] S. Ito, S. Yoshida, and T. Watanabe, “Fabrication and characterization of meso-macroporous anatase TiO_2 films.” *Bulletin of the Chemical Society of Japan*, vol. 73, no. 8, pp. 1933– 1938, 2000.

[7] R. Abe, M. Higashi, and K. Domen, “Facile fabrication of an efficient oxynitride TaON photoanode for overall water splitting into H_2 and O_2 under visible light irradiation,” *Journal of the American Chemical Society*, vol. 132, no. 34, pp. 11 828–11 829, 2010.

[8] M. Higashi, K. Domen, and R. Abe, “Fabrication of efficient TaON and Ta_3N_5 photoanodes for water splitting under visible light irradiation,” *Energy & Environmental Science*, vol. 4, no. 10, pp. 4138–4147, 2011.

[9] T. Minegishi, N. Nishimura, J. Kubota, and K. Domen, “Photoelectrochemical properties of $LaTiO_2N$ electrodes prepared by particle transfer for sunlight-driven water splitting,” *Chemical Science*, vol. 4, no. 3, pp. 1120–1124, 2013.

[10] K. Ueda, T. Minegishi, J. Clune, M. Nakabayashi, T. Hisatomi, H. Nishiyama, M. Katayama, N. Shibata, J. Kubota, T. Yamada, and K. Domen, “Photoelectrochemical oxidation of water using $BaTaO_2N$ photoanodes prepared by particle transfer method,” *Journal of the American Chemical Society*, vol. 137, no. 6, pp. 2227–2230, 2015.

[11] J. Seo, T. Takata, M. Nakabayashi, T. Hisatomi, N. Shibata, T. Minegishi, and K. Domen, “Mg–Zr cosubstituted Ta_3N_5 photoanode for lower-onset-potential solar-driven photoelectrochemical water splitting,” *Journal of the American Chemical Society*, vol. 137, no. 40, pp. 12 780–12 783, 2015.

[12] H. Kumagai, T. Minegishi, Y. Moriya, J. Kubota, and K. Domen, “Photoelectrochemical hydrogen evolution from water using copper gallium selenide electrodes prepared by a particle transfer method,” *The Journal of Physical Chemistry C*, vol. 118, no. 30, pp. 16 386–16 392, 2014.

[13] J. Liu, T. Hisatomi, G. Ma, A. Iwanaga, T. Minegishi, Y. Moriya, M. Katayama, J. Kubota, and K. Domen, “Improving the photoelectrochemical activity of $La_5Ti_2CuS_5O_7$ for hydrogen evolution by particle transfer and doping,” *Energy Environ. Sci.*, vol. 7, no. 7, pp. 2239–2242, 2014.

[14] H. B. Michaelson, “The work function of the elements and its periodicity,” *Journal of Applied Physics*, vol. 48, no. 11, pp. 4729–4733, 1977.

[15] Y.-W. Chung and W. B. Weissbard, “Surface spectroscopy studies of the $SrTiO_3$(100) surface and the platinum- $SrTiO_3$(100) interface,” *Physical Review B*, vol. 20, no. 8, p. 3456, 1979.

[16] K. Van Benthem, C. Elsässer, and R. French, “Bulk electronic structure of $SrTiO_3$: Experiment and theory,” *Journal of Applied Physics*, vol. 90, no. 12, pp. 6156–6164, 2001.

[17] Y. Jiang, Y. Jinhua, and Z. Zhigang, “Enhanced photoelectrolysis of water with photoanode Nb : $SrTiO_3$,” *Applied Physics Letters*, vol. 85, no. 4, pp. 689–691, 2004.

[18] A. N. Pinheiro, E. G. Firmiano, A. C. Rabelo, C. J. Dalmaschio, and E. R. Leite, “Revisiting $SrTiO_3$ as a photoanode for water splitting: development of thin films with enhanced charge separation under standard solar irradiation,” *RSC Advances*, vol. 4, no. 4, pp. 2029–2036, 2014.

Chapter 5: Summary and Outlooks

5.1. Conclusions in this Study

In this work, photocatalytic and photoelectrochemical overall water splitting on particulate $SrTiO_3$ was investigated. Effects of cation doping and flux treatments on photocatalytic overall water splitting of particulate $SrTiO_3$ were discussed. To understand the reason of different photocatalytic activities of the modified $SrTiO_3$ particles, carrier dynamics of photo-excited carriers in the photocatalysts were studied by using the time-resolved absorption spectroscopy. Photoelectrochemical properties of these particles were examined using photoelectrodes fabricated by particle transfer method.

In chapter 1, properties and history of $SrTiO_3$ as a photocatalyst, the principles of photocatalytic and photoelectrochemical reactions, and experimental techniques such as measurement of photocatalytic activity and characterization of photoelectrochemical properties are explained in detail. Problems of $SrTiO_3$ which has absorption edge of over 300 nm as a photocatalyst for overall water splitting are pointed out based on the properties of the material, and the purpose of my study was declared.

In chapter 2, enhancement of overall water splitting activity on $SrTiO_3$ under UV light by doping with cations having different valences and by flux treatments are discussed. The $SrTiO_3$ particles synthesized by using $SrCl_2$ as a flux showed an apparent quantum efficiency (AQE) of 30% at 360 nm which is, so far the highest value in the photocatalytic overall water splitting reaction at the wavelength of over 300 nm. The composition analysis revealed that unexpected Al doping to the $SrTiO_3$ particles occurred during the flux treatment in an alumina crucible. The comparison of ionic radius of cations clarified that Al^{3+} can replace Ti^{4+}, and the doping can suppress the formation of Ti^{3+} which has been considered as one of the recombination sites in $SrTiO_3$. I concluded that the Al doping to the $SrTiO_3$ particles is the essential for the high photocatalytic activity. Al doped $SrTiO_3$ particles synthesized without the use of flux resulted in only the quarter rate of hydrogen and oxygen evolution compared to the case of with the use of flux. The experimental results show that both Al doping and the use of flux are indispensable to obtain the high photocatalytic activity in overall water splitting. Effects of the flux treatment on the structural properties of $SrTiO_3$ are also discussed in detail in this chapter.

In chapter 3, carrier dynamics in modified $SrTiO_3$ particles investigated by time-resolved absorption spectroscopy, and the reason of the enhanced photocatalytic activity by Al doping and the flux treatment are discussed. The optical absorptions found at NIR-Vis. region were assigned through the variation of the light absorption by existence of the hole or electron scavengers. Consequently, there was a clear relationship between the life time of the electron bound at shallowly trap levels and photocatalytic activity in overall water splitting. I concluded that the life time of the absorption by the electron bound at shallowly trap levels is clearly enhanced by the flux treatment, and the enhancement of the life time is essential for the higher photocatalytic activity.

In chapter 4, a $SrTiO_3$ electrode with a high IPCE was prepared from $SrTiO_3$ particles by the particle transfer method. The photoanodes had desirable structural properties such as strong anchoring of the faceted and micron-sized $SrTiO_3$ particles onto the underlying metal layers. The resulting structure of the prepared electrodes exhibited efficient light absorption, smooth electron transfer from the particles to the back electrode, and enhanced charge separation. A systematic study of the contact layer material used for $SrTiO_3$ photoanodes prepared from both particles and single-crystal wafers revealed that Ta is the best material for forming ohmic contact, and the results are consistent with a general discussion on metal-semiconductor contacts based on the work function. The photoanode prepared by particle transfer method from Al doped $SrTiO_3$ particles prepared by using flux exhibited a high IPCE of 69% at 1.23 V_{RHE}, which is higher than that for the photoanode fabricated from the single crystal of Nb doped $SrTiO_3$, 18%. In fact, this IPCE is the highest among photoanodes prepared from similar materials. These results suggest that once photocatalytic materials with sufficient crystallinity and sensitivity to sunlight are developed, efficient solar hydrogen production from water using simple and scalable particle-based systems will become possible. Finally, the photocatalytic activity for overall water splitting of $SrTiO_3$ particles varied depending on the synthesis method used to produce the particles. These differences are likely due to the different mechanisms by which water splitting takes place on the electrode. I believe that although the crystallinity of Al doped $SrTiO_3$ prepared by using flux is sufficiently high, its resistivity is too large for application to photoanodes.

5.2. Future Outlook

The AQE of photocatalytic overall water splitting was improved to 30% at 360 nm using Al doped $SrTiO_3$. This drastic improvement in the AQE in the near UV region is achieved by doping assisted by facile flux treatments. This points to various important and useful aspects in the development of photocatalytic water splitting. Firstly, similar concepts may be readily applicable to non-oxide photocatalytic materials such as (oxy)nitrides and (oxy)sulfides that operate under visible light to produce higher AQE at longer wavelengths, because doping has been an essential method to upgrade the properties of semiconducting materials. Secondly, the behavior of photo-excited carriers during the water splitting reaction can be discussed more clearly because the influence of recombination is less significant compared to earlier works. Knowledge based on the behavior of photoexcited carriers surely promotes the development of more active photocatalysts. Thirdly, photocatalysts that are highly active in the overall water splitting may be used to design efficient, scalable, and safe reactors for photocatalytic water splitting. Unlike photoelectrochemical and electrochemical systems, photocatalytic systems evolve hydrogen and oxygen in proximity. Therefore, it is necessary to utilize actual photocatalysts to study the behavior of gaseous mixture of hydrogen and oxygen in a reactor. Al doped $SrTiO_3$ studied in my work may serve as a model photocatalyst for such purposes. Finally, this work points to the importance of controlling impurities in photocatalysts because a very small amount of impurities can affect the photocatalytic activity drastically, where their effect can be either positive or negative.

The $SrTiO_3$ electrode fabricated by particle transfer method from flux treated and Al doped $SrTiO_3$ particles and Ta as contact layer showed comparable performance with $SrTiO_3$ photoelectrode fabricated from single crystalline wafer of Nb doped $SrTiO_3$. The $SrTiO_3$ electrode fabricated by particle transfer method showed relatively high IPCE of 69%, reflecting the possibility of particle based photoelectrochemical cells efficient for sunlight driven water splitting. However, preparation of high quality photocatalytic particles with absorption edge long enough to absorb visible light is still a challenge.

Through this study, I showed possibility of sunlight driven water splitting by photocatalysis and photoelecrochemistry. Further development of photocatalytic materials which could utilize visible light, of modification of the photocatalytic particles, and of cocatalysts to decrease overpotentials of water splitting reactions will allow us to obtain hydrogen from water under sunlight with practical efficiency.

Appendix A. Standard Solar Spectrum

The utilization of solar energy is widely studied in various research fields. The solar radiation at the Earth's surface widely changes upon the location, the season of the year, the time of day, and the atmosphere. Therefore, it is necessary to decide standard solar spectrum to compare the experimental results which used the solar irradiation. The standard solar spectra were determined by several research groups including the American Society for Testing and Materials. The standard was sophisticated over the year and the current Standard Reference Spectra are the standard direct normal spectral irradiation with air mass 1.5, and the standard global total spectral irradiation on the 37° sun facing tilted surface with air mass 1.5. These two spectra are abbreviated as AM1.5 and AM1.5G, and are presented in Figure A-1. The data of these spectra are in open access in the National Renewable Energy Laboratory website (http://rredc.nrel.gov/solar/spectra/am1.5/).

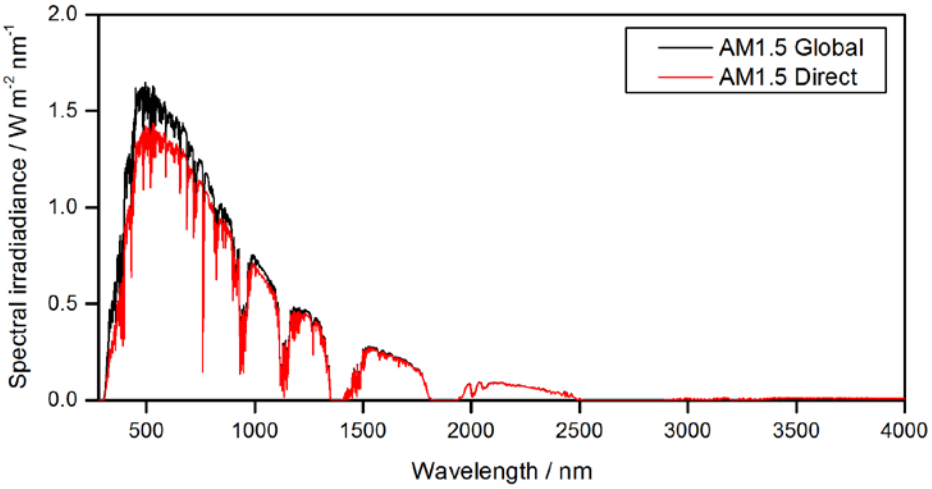

Figure A-1. The two different standard solar spectra

Appendix B. Examination of the Heterogeneous Nucleation on Crucible Surface during the Flux Treatment

In chapter 2, I applied Wanklyn's theory that for the crystal growth in flux, nucleation mainly occurs on the crucible surface. To examine this theory flux treatment on $SrTiO_3$ was performed using crucibles with different sizes as in figure B-1. The Type A crucible is the same size with the alumina crucibles used in chapter 2, and the Type B crucible is much bigger than the Type A crucible. 1.8348 g of $SrTiO_3$ and 15.8523 g of $SrCl_2$ were thoroughly mixed and put into each type of crucibles. Since the same amount of the mixture was put into crucibles with different sizes, it is expected that the area of crucible that is in direct contact with the mixture is much larger when the Type B crucible was used. The area of the crucible surface that is in direct contact with the mixture divided by the volume of the mixture was roughly estimated, and it was about 2 cm^{-1} and 15 cm^{-1} for the Type A and the Type B crucible, respectively. If the heterogeneous nucleation on the crucible surface is the dominant nucleation process, number of nucleation sites should be much larger for the Type B crucible compared to the Type A crucible. This means that the number crystals obtained when the Type B crucible was used should be much larger than the number of crystals obtained when the Type A crucible was used. Since I used the same amount of mixture, it is expected that the size of crystals obtained in the Type B crucible should be much smaller than the size of crystals obtained in the Type A crucible. Figure B-2 shows the SEM images of the $SrTiO_3$ particles obtained by using each crucible. It is quite clear that the average size of the $SrTiO_3$ particles obtained in the Type A crucible is much bigger than the average size of the $SrTiO_3$ particles obtained in the Type B crucible. The surface area of the samples obtained in the Type A crucible and the Type B crucible were 0.9 m^2 g^{-1} and 2.8 m^2 g^{-1}, respectively. The difference in the surface area well agreed the difference on the particle size. As it was expected, smaller particles were obtained when bigger crucible was used. This result strongly supports that during the $SrCl_2$ flux treatment of $SrTiO_3$, nucleation is mainly occur on the surface of crucible.

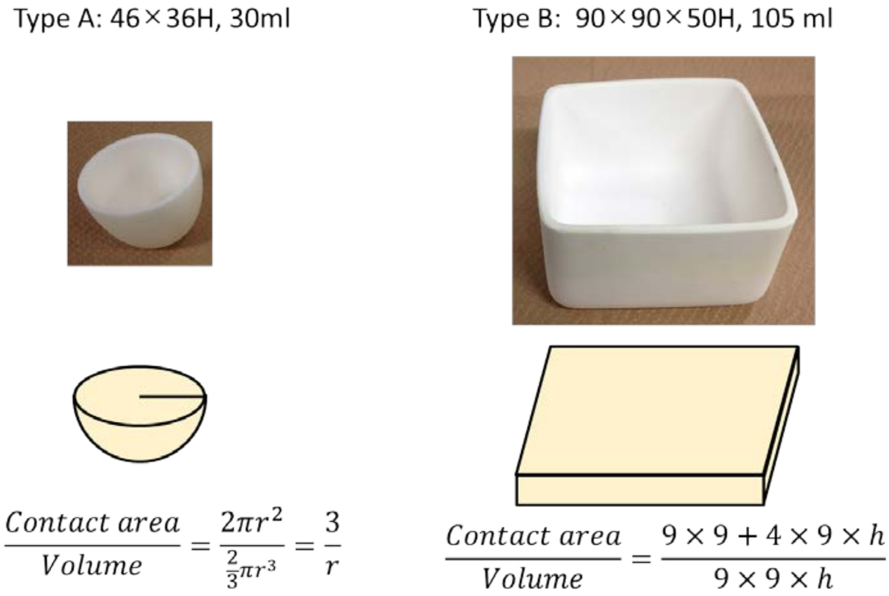

Figure B-1. The Type A crucible and the Type B crucible used for the flux treatment.

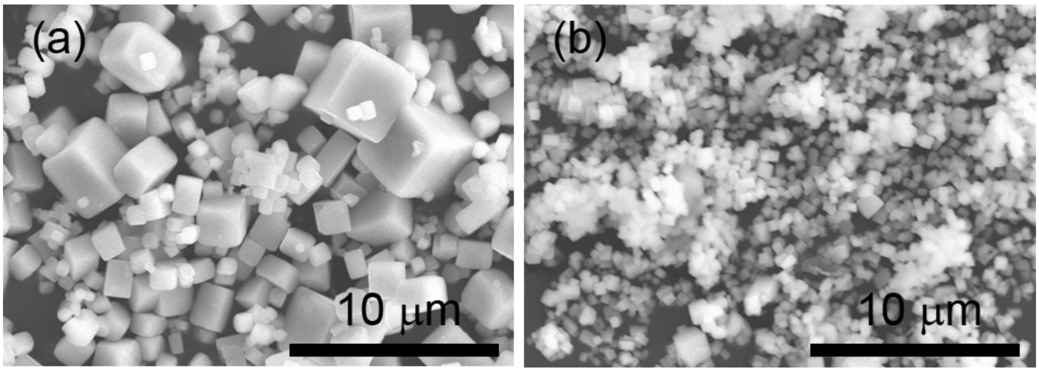

Figure B-2. The SEM images of flux treated $SrTiO_3$ (a) in Type A crucible and (b) in the Type B crucible.

List of Publication

1. **Yeilin Ham**, Takashi Hisatomi, Yosuke Goto, Yosuke Moriya, Yoshihisa Sakata, Akira Yamakata, Jun Kubota, Kazunari Domen, “Flux-Mediated Doping of $SrTiO_3$ Photocatalysts for Efficient Overall Water Splitting”, *Journal of Materials Chemistry A*, accepted.
2. Yoshihisa Sakata, Yoshiko Miyoshi, Tatsuya Maeda, Kohki Ishikiriyama, Yuki Yamazaki, Hayao Imamura, **Yeilin Ham**, Takashi Hisatomi, Jun Kubota, Akira Yamakata, Kazunari Domen, “Photocatalytic Property of Metal ion Added $SrTiO_3$ to the Overall H_2O Splitting”, *Applied Catalysis: A General*, accepted.
3. Akira Yamakata, **Yeilin Ham**, Masayuki Kawaguchi, Takashi Hisatomi, Jun Kubota, Yoshihisa Sakata, Kazunari Domen, “Morphology-Sensitive Trapping States of Photogenerated Charge Carriers on $SrTiO_3$ Particles Studied by Time-Resolved Visible to Mid-IR Absorption Spectroscopy: The Effects of Molten Salt Flux Treatments”, *Journal of Photochemistry and Photobiology A: Chemistry*, in press.
4. **Yeilin Ham**, Minegishi Tsutomu, Takashi Hisatomi, Kazunari Domen, “$SrTiO_3$ Photoanode Prepared by Particle Transfer Method for Oxygen Evolution from Water with High Quantum Efficiencies”, *Chemical Communications*, submitted.
5. **Yeilin Ham**, Kazuhiko Maeda, Dongkyu Cha, Kazuhiro Takanabe, Kazunari Domen, “Synthesis and Photocatalytic Activity of Poly(triazine imide)”, *Chemistry – an Asian Journal*, 8 (1), 2013, 218-224.
6. Jang Mee Lee, Jayavant L. Gunjakar, **Yeilin Ham**, In Young Kim, Kazunari Domen, Seong-Ju Hwang, “A Linker-Mediated Self-Assembly Method to Couple Isocharged Nanostructures: Layered Double Hydroxide─CdS Nanohybrids with High Activity for Visible-Light-Induced H_2 Generation”, *Chemistry − a European Journal*, 20 (51), 2014, 17004-17010.

Acknowledgments

I want to express my deep gratitude to Professor Kazunari Domen. I do not think there is a way that I could pay back what you have given me. You gave me another change, and I hope you do not regret that decision. Your attitude toward the research and toward colleagues was what I most wanted to learn from you. It was my blessing that I could come to your laboratory.

Professors I met in Domen laboratory were all really brilliant people. I discussion with Professor Jun Kubota, Professor Kazuhiko Maeda, Professor Kazuhiro Takanabe, Professor Tsutomu Minegishi and Professor Masao Katayama were very kind and their ideas were always helpful for my research.

Also, I am obliged to Dr. Takashi Hisatomi, Dr. Yosuke Moriya, Professor Yoshihisa Sakata and Professor Akira Yamakata. This thesis was never finished with the help from them.

Ms. Tomita and Ms. Minegishi were the most nicest, kind people, and time to time small talk with them was a few happy entertainment I had in our lab.

Also, I need to thank Professor Takayuki Komatsu. I always tough of him as my father, and I hope to do so as long as he allow me to do so.

My family is probably why I am working at all. I am very blessed to have my family Woonchul Ham, Inja Kim and Hyeilin Ham. Hyeilin’s advice to me for writing doctoral thesis was what I rely on the most.

I was also supported by my dearest friend Bosul Jeon, and my kind Doctor Takei.

Thomas Kuhn’s book let me understand a lot about this field more than anyone else. While doing these experiments I always struggled with the lack of theorems and even hypothesis or premises. This book let me understand that situation. Now I understand that the field of photocatalytic water splitting is only on the stage of normal science and the lack of theorem is a natural state of the normal science. This realization let me work harder so that I could contribute for this field to move forward to be a new paradigm.

I own thanks to Rainer Maria Rilke, Arthur Schopenhauer, Herman Hesse, Patrick Suskind and many other great teachers who taught me how to live, and gave me the strength to finish this thesis. The fact that people like them existed, people who care about human being exists itself was a great relief for me.

Last but not least, I want to express my gracefulness to hyde. The truth is, so long as I can breathe or my eyes can see, every work I do should be dedicated to him.